Generation and characterisation of quantum entanglement using SPDC photons

A THESIS

submitted for the Award of Ph.D. degree of

MOHANLAL SUKHADIA UNIVERSITY

in the

Faculty of Science

by

Jabir M.V

Under the Supervision of

Goutam K Samanta

Associate Professor
Atomic, Molecular, and Optical Physics Division
Physical Research Laboratory
Ahmedabad, India.

DEPARTMENT OF PHYSICS

MOHANLAL SUKHADIA UNIVERSITY

UDAIPUR

Year of submission: 2018

To

My family,

Their love, enduring compassion and support deserve eternal gratitude.

DECLARATION

I, **Mr. Jabir M.V***, S/o Mr. Hamza M.P, resident of PRL hostel, Thaltej, Ahmedabad, 380009, hereby declare that the research work incorporated in the present thesis entitled,* **"Generation and characterisation of quantum entanglement using SPDC photons"** *is my own work and is original. This work (in part or in full) has not been submitted to any University for the award of a Degree or a Diploma. I have properly acknowledged the material collected from secondary sources wherever required. I solely own the responsibility for the originality of the entire content.*

Date:

(Jabir M.V)

CERTIFICATE

I feel great pleasure in certifying that the thesis entitled, **"Generation and characterisation of quantum entanglement using SPDC photons"** embodies a record of the results of investigations carried out by Mr. Jabir M.V under my guidance. He has completed the following requirements as per Ph.D regulations of the University.

(a) Course work as per the University rules.

(b) Residential requirements of the University.

(c) Regularly submitted six monthly progress reports.

(d) Presented his work in the departmental committee.

(e) Published a minimum of one research paper in a referred research journal.

I am satisfied with the analysis, interpretation of results and conclusions drawn. I recommend the submission of the thesis.

Date:

Goutam K Samanta
(Thesis Supervisor)
Associate Professor, AMOPH,
Physical Research Laboratory,
Ahmedabad - 380 009

Countersigned by

Head of the Department

Abstract

In this work we investigate the generation and characterization of quantum entanglement in two photon state (bi-photon mode). We explore the scope of developing sources entangled in different degrees-of-freedom (DoFs) based on a second order non-linear optical process known as spontaneous parametric down conversion (SPDC). Polarization and orbital angular momentum (OAM) DoF are the two important bases for the entangled states. The entangled state based on polarization DoF is not only extensively used to understand the fundamental properties of entanglement but it also used in various application like quantum teleportation, quantum cryptography etc. Unfortunately, the existing sources of polarization entanglement suffer from the common draw back in terms of number of entangled photons generated through SPDC process. However any practical applications of the entangled source including ground to satellite quantum communication demand entangled photons with high brightness. We develop a compact, simple and robust polarized entangled photon source with high brightness at room temperature. Using periodically-poled potassium titanyl phosphate crystal, we produce non-collinear, type-0, phase-matched, degenerate photons at 810 nm with high spectral brightness. So far, this is the highest number of degenerate photons generated using a continuous-wave laser pumped bulk crystal and detected using multimode fiber. We have studied the dependence of pump focusing on the brightness of the generated photons collected using both multimode, and single mode

fibers. Combining the crystal in a novel system architecture comprised of Sagnac interferometer and polarizing optical elements, the source produces polarization entangled photon states with high fidelity.

The entangled photons generated in SPDC with Gaussian pump is well understood, however, there few reports to understand the effect of structured pump beam on entanglement properties of the down converted photons. To understand the complete effect of structured beam on entanglement properties, one need to study the modificaiton of wave-vectors while pumping with structured beam. Therefore, with the help of a new class of beam called perfect vortex, we investigate the effect of OAM and the spatial profile on angular spectrum of SPDC photons. The “perfect” vortex is a new class of optical vortex beam having ring radius independent of its topological charge (order). One of the simplest techniques to generate such beams is the Fourier transformation of the Bessel-Gauss beam. We demonstrate a novel experimental scheme to generate perfect vortex of any ring radius using a convex lens and an axicon. Using such vortex we have studied non-collinear interaction of photons having OAM in SPDC process and observed that the angular spectrum of the SPDC photons are independent of OAM of the pump photons, rather depends on spatial profile of the pump beam. With the understanding of the OAM effect on down converted photons, we pumped non-linear dual-crystal with vortex beam to study the effect of spatial profile on polarization entanglement. We have verified that the pump spatial profile is transferred to the bi-photon spatial profile in SPDC process with out effecting the polarization entanglement bi-photon modes.

In addition to the entanglement in polarization DoF, we have investigated the entanglement between different DoF known as hybrid entanglement. Till now hybrid entangled photons are generated by applying post-selection method in the SPDC photons. Since the SPDC process is feeble and produces low number of entangled photons, further selection to these photons reduces over all count of the photons. To overcome such problem, we have demonstrated a novel experimental scheme to generate hybrid entangled photons with help of classical non-separable pump beam. Using Sagnac interferometer we have generated non-seperable beam and verified the inseparability of OAM and polarization DoF with projection measurement. By pumping contiguous non-linear crystal with non-separable beam, we have generated two photon (bi-photon) hybrid entangled state. With help of coincidence measurement, spatial profile of the heralded signal photons can be revived by conditioning the idler photon into Gaussian mode. Polarization projection in idler reveals the phase profile or OAM content of the heralded signal photons. To verify the entanglement between OAM and polarization DoF in bi-photons modes, we measure the entanglement witness operator and showed it exceeds the classical bound.

Entanglement in OAM degree of freedom can give higher dimensional entanglement, thus useful in improving information capacity of the photons as well as increases the security and robustness from eavesdropping. Since the higher dimensional entangled state give more advantageous over two dimensional state in secure communication, we explore the dimensionality of OAM entangled state with help of asymmetric vortex beam. We controll the bi-photon orbital angular momentum (OAM) eigen modes in the spontaneous parametric down conversion process by adjusting the asymmetry of the pump vortex beam. Adjusting the optic axis of the spiral phase plate (SPP) of phase winding corresponding to OAM mode, l, with respect to the beam propagation axis, we have transformed a Gaussian beam into an asymmetric vortex beam with OAM modes, l, l-1, l-2 $\ldots$0 with different weightages. By pumping the nonlinear crystal with such asymmetric vortices and controlling their asymmetry we have tailored the spiral spectrum of the bi-photon OAM eigen modes. Calculating the Schmidt number of the bi-photons shows the increase in the spiral bandwidth of the OAM eigen modes and hence the dimensionality of the system.

LIST OF PUBLICATIONS

Journal publications

Publications included in the thesis

1. *Controlling the biphoton orbital angular momentum eigenmodes using asymmetric pump vortex beam*
   M. V. Jabir, Ali Anwar, and G.K. Samanta,
   arXiv,1803.04635 (2018).

2. *Robust, high brightness, degenerate entangled photon source at room temperature*,
   M.V. Jabir, and G.K. Samanta,
   Scientific Reports 7, 12613 (2017).

3. *Direct transfer of classical non-separable states into hybrid entangled two photon states,*
   M. V. Jabir, N. Apurv Chaitanya, Manoj Mathew, and G.K. Samanta,
   Scientific Reports 7, 7331 (2017).

4. *Control of spatial distribution of entangled photons by the spatial structure of classical pump beam,*
   M.V. Jabir, and G.K. Samanta,
   Frontiers in Optics, JTh2A. 18, Optical Society of America (2016).

5. *Generation of "perfect" vortex of variable size and its effect in angular spectrum of the down-converted photons*,
   M.V. Jabir, N. Apurv Chaitanya, A. Aadhi, and G.K. Samanta,
   Scientific Reports 6, 21877 (2016).

Publications not included in the thesis

1. *Hollow Gaussian beam generation through nonlinear interaction of photons with orbital-angular-momentum,*
   Apurv Chaitanya N., **M.V. Jabir**, J. Banerji, and G.K. Samanta,
   Scientific Reports 6, 32464 (2016).

2. *Efficient nonlinear generation of high power, higher order, ultrafast "perfect" vortices in green,*
   Apurv Chaitanya N., **M.V. Jabir**, and G.K. Samanta,
   Optics Letters 41, 1348 (2016).

3. *Airy beam optical parametric oscillator,*
   A. Aadhi, Apurv Chaitanya N., **M.V. Jabir**, Pravin Vaity, R. P. Singh, and G.K. Samanta,
   Scientific Reports 6, 25245 (2016).

4. *Frequency-Doubling of Femtosecond Pulses in "Thick" Nonlinear Crystals With Different Temporal and Spatial Walk-Off Parameters*,
   Apurv Chaitanya N., A Aadhi, S Chaitanya Kumar, **M.V. Jabir**, G.K. Samanta, and M Ebrahim-Zadeh,
   IEEE Photonics Journal 8,1 (2016).

5. *High-power, high-repetition-rate, Yb-fiber laser based femtosecond ultraviolet source at 355 nm*,

Apurv Chaitanya N., A. Aadhi, **M.V. Jabir**, and G.K. Samanta,
Optics Letters 40, 4269 (2015).

6. *Frequency-doubling characteristics of high-power, ultrafast vortex beams*,
   Apurv Chaitanya N., A. Aadhi, **M.V. Jabir**, and G.K. Samanta,
   Optics Letters 40, 2614 (2015).

7. *All-periodically poled, high-power, continuous-wave, single-frequency tunable UV source*,
   A. Aadhi, Apurv Chaitanya N., **M.V. Jabir**, R. P. Singh, and G.K. Samanta,
   Optics Letters 40, 33 (2015).

Selected Conference papers:

1. *Generation of hybrid entangled two photon state using classical non-separable state of the pump beam*,
   M.V. Jabir, Apurv Chaitanya N., and G.K. Samanta,
   Frontiers in Optic, JW4A.29, Optical Society of America (2017).

2. *Robust, bright entangled photon source based on type-0, non-collinear phase-matching in periodically poled crystal*,
   M.V. Jabir, and G.K. Samanta,
   Frontiers in Optic, JW4A.30, Optical Society of America (2017).

3. *Control of spatial distribution of entangled photons by the spatial structure of classical pump beam,*
   M.V. Jabir, and G.K. Samanta,
   Frontiers in Optics, JTh2A. 18, Optical Society of America (2016).

4. *Generation of hybrid entangled two photon state by transferring classical non-separable sate,*

   M.V. Jabir, Apurv Chaitanya N., A Aadhi, and G.K. Samanta,

   International Conference on Fibre Optics and Photonics, Tu3C. 3, Optical Society of America (2016).

5. *Continuous- wave, high Power, single-frequency, tunable ultraviolet source based on all periodically poled crystals,*

   M.V. Jabir, Apurv Chaitanya N., M. Mathew, and G.K. Samanta,

   International Conference on Fiber Optics and Photonics, M3A.4, Optical Society of America (2014).

6. *Nonlinear Generation of High Power and Higher order Hollow Gaussian Beam,*

   Apurv Chaitanya N., **M.V. Jabir**, J Banerji, and G.K. Samanta,

   Frontiers in Optics, FTh5B. 5, Optical Society of America (2016).

7. *Airy beam optical parametric oscillator,*

   A. Aadhi, Pravin Vaity, Apurv Chaitanya N., **M.V. Jabir**, R. P. Singh, and G.K. Samanta,

   CLEO: QELS Fundamental Science, JTh5A-6, Optical Society of America (2015).

8. *Single-frequency continuous-wave tunable ultraviolet sources based on BIBO and PPKTP crystals and their comparative studies,*

   A. Aadhi, Apurv Chaitanya N., **M.V. Jabir**, R. P. Singh, and G.K. Samanta,

   International Conference on Optics and Photonics, Proc. SPIE-9654 (2015).

9. *All Periodically-poled Crystals Based Source of tunable, Continuous-wave, Single-frequency, Ultraviolet Radiation*

   A. Aadhi, Pravin Vaity, Apurv Chaitanya N., **M.V. Jabir**, R. P. Singh, and G.K.

Samanta,

CLEO: QELS Fundamental Science, JTh5A-26, Optical Society of America (2015).

10. *Optimization of frequency-doubling of high power, high repetition rate, femtosecond fiber laser in thick nonlinear crystal,*

    Apurv Chaitanya N., A. Aadhi, **M.V. Jabir**, Vinayak Kumar, R. P. Singh, and G.K. Samanta,

    International Conference on Fibre Optics and Photonics, M4A-28, Optical Society of America (2014).

Contents

List of Tables

List of Figures

Chapter 1

Introduction

Ever since the inception of quantum mechanics, variety of criticism has been aroused against the probabilistic nature of quantum theory. In 1935, Einstein, Podolsky and Rosen raised an important criticism against the quantum mechanics in the paper titled "Can quantum-mechanical description of physical reality be considered complete?" [1]. They proposed an imaginary experiment in which measurements of one subsystem revealed information about another subsystem without measuring the second one directly. With the idea of non-causal behavior of such system, they claimed that the possibility of such an experiment contradicted a basic dogma of standard quantum theory. Later such radical behavior of the system named as Quantum entanglement by Erwin Schrodinger. Since then, entanglement between two quantum systems is of great interest in basic physics to test the fundamental tenet of the quantum mechanics. Along with the advancement of quantum mechanics, there have been claim that the quantum mechanics is incomplete without introducing the hidden variables. In 1964, J. S. Bell [2] formulated an inequality based on locality and realism which would be violated by entangled states. Bells theorem disagreed with the idea of hidden variables and established the fact that the quantum mechanics is complete. Since then Bells inequality become popular qualitative test for verifying the entanglement of any correlated systems. Last few decades entangled system drawn a great attention as it highly useful in quantum information and quantum communication. Therefore, development of entangled system is very important for practical implementation of quantum protocols. Significant attempts have been done to develop entangled source. Among the different entangled system based on atoms, bosons and etc, photon based entangled system attained great popularity among scientist due to fact that the photons can be easily used for communication purpose. While different techniques are demonstrated to generate entangled photon pair such as quantum dots, Hong-Ou-Mandel effect etc, majority of entangled photons are generated through spontaneous parametric down conversion process (SPDC).

SPDC is a second order nonlinear optical process, where a high energy photon splits into two low daughter photons owing to the energy conservation. Since these daughter photons are generated simultaneously they maintain a correlation among themselves in different degrees-of-freedom (DoFs) including polarization, orbital angular momentum, time, path etc. This correlation leads to the entanglement of photon pair in those DoF. Among the different DoFs, entangled photon states based on polarization DoF is not only extensively used to understand the fundamental properties of entanglement but it also used for the various applications like quantum teleportation, quantum cryptography, quantum free space communication etc. Unfortunately, the SPDC based entangled photon sources suffer from common draw back of low number of photons due to the low non-linear parametric gain. However, any practical application of the entangled source including ground to satellite quantum communication demands entangled photons with high brightness. Efforts have been made to improve the brightness of the entangled photon sources by exploring different nonlinear crystals in bulk and wave-guide structures. In addition to that, different phase-matching techniques including type-II, type-I and type-0 have been implemented in different experimental schemes. Crystal length and non-linearity are two important parameters which greatly influence the overall gain of the SPDC process for a given pump intensity. With the manipulation of these two parameters the brightness of the entangled photon sources have been significantly improved over the years. However, the brightness obtained through the use of long periodically poled crystals engineered for high effective nonlinearity do not exploit the maximum gain of the non-linear crystal in type-I and type-II birefringent phase matching conditions. Therefore, to access the highest effective non-linearity of the periodically poled crystal, type-0 quasi-phase-matching (QPM) is the proper choice to obtain the maximum gain. Therefore, using Gaussian pump beam in type-0 phase matched periodically poled crystal, we have developed high brightness entangled source and studied its characteristic properties.

Since the polarization entanglement are limited to two dimensional basis (($|H\rangle$, $|V\rangle$), ($|R\rangle$, $|L\rangle$), and($|D\rangle$, $|A\rangle$)), where $|H\rangle$, $|V\rangle$, $|R\rangle$, $|L\rangle$, $|D\rangle$, and $|A\rangle$ are horizontal, vertical, right circular, left circular, diagonal, and anti-diagonal polarization respectively, one can not depend on polarization DoF to develop higher dimensional entangled state. As the higher dimensional entangled state provides higher information capacity and robustness against eavesdropping, development of such state are essential for secure communication. Fortunately, orbital angular momentum (OAM) is one of the important DoF which provides higher dimensional entanglement. Therefore, development of higher dimensional entangled state via SPDC process necessitate the investigation of OAM DoF of bi-photon modes. Typically, the studies on OAM DoF are done through the manipulation of SPDC photons using mode converters, such as, spatial light modulator (SLM) and q-plate, in complicated experimental schemes. However, the phase modulators reduces the overall number of photons and thus limiting the use of OAM DoF for practical applications requiring entangled state with high brightness. Most of the OAM based entangled systems are developed with Gaussian pump beam. In contrast to that, couple of studies have shown that the bi-photon mode generated through SPDC process will have the same transverse spatial profile as well the phase profile of the pump beam. Therefore, instead of using Gaussian beam, one can alternatively manipulate the bi-photon modes using structured (phase modulated) pump beam without compromising the photon number generated in the SPDC process. Moreover, manipulation of the laser pump beams reduce alignment difficulty arises from the low number of photon generated in SPDC process. To study how the spatial and phase profile of the pump beam effects on the SPDC photons, one need to understand the angular spectrum (transverse wave vector) of the individual SPDC photons. Angular spectrum not only indicate the presence of any asymmetry in spatial structure of the bi-photon mode, but it also dictates the quality of spatial entanglement in the bi-photon modes. Therefore, we have thoroughly investigated the effect angular spectrum using phase modulated structured beam.

One of the important entangled states based on OAM DoF is the hybrid entangled states, in which the OAM and polarization DoFs are entangled with each other. Hybrid entangled state allow the generation of qubit-qudit entangled states, macroscopic entanglement with very high quanta of OAM and improvement in angular resolution in remote sensing in quantum communication. Therefore, it is imperative to design an efficient technique to generate such states. With the clear understanding of the effect of structured beam on angular spectrum, we have carried out the study of bi-photon mode as it is more detrimental while developing any OAM based entangled source. We have studied the spatial profile of the bi-photon modes entangled in polarization DoF while pumping with of vortex beam (OAM beam) and verified that pump profile can be transferred to the bi-photon modes. Even after the spatial modulation of the bi-photon modes, the entanglement in polarization DoF is not significantly effected. Therefore such studies show the scope of modulating the bi-photon modes without effecting the other DoF. Owing to such result, we have designed a technique to generate hybrid entangled state directly from the non-separable beam, in which the OAM and polarization are inseparable. We have pumped the non-linear crystal with non-separable state and generated two photon (bi-photon) hybrid entangled state. Such study has opened up the possibility of transferring any pump state into bi-photon modes through SPDC process.

In principle, the dimension of the OAM based entangled state has no upper limit, which means the bi-photon generated in SPDC process has the potential to carry large amount of

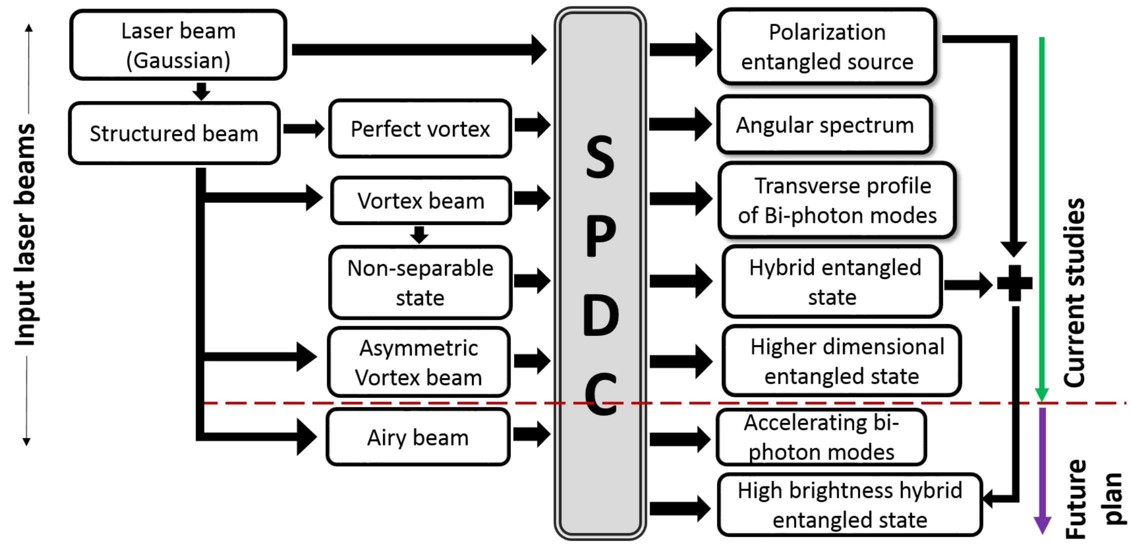

Figure 1.0.1: Pictorial representation of development of entangled system during thesis work.

information. The dimensionality of the system is characterized by the number of OAM bi-photon eigen modes generated in the process. Significant studies have been done to increase the number of OAM bi-photon modes, thus to increase the dimensionality of the entangled state. Till date, the increase of the dimensionality have been achieved by the manipulation of the Gaussian pump beam waist and the crystal length. However, the generated bi-photon modes in such techniques are restricted to a single subspace in the Hilbert space spanned by the pump OAM order $l_p = 0$. In order to access the more subspace, therefore more eigen modes, one can manipulate the OAM mode of the pump beam. Tailoring the pump beam in such a way that it contains multiple OAM modes, can create multiple subspace in bi-photon OAM Hilbert space. Recent studies have shown that asymmetric vortex beam can give superposition of different OAM modes in a single beam. Using such asymmetric pump vortex beam, we have studied the OAM bi-photon modes and observed the increase in the number of subspace and hence number of bi-photon OAM eigen modes.

The thesis has been divided into 8 chapters. The schematic representation of the thesis shown in Fig. 1.0.1. The motivation of the thesis is to develop and study photon source entangled in different degrees-of-freedom. Theoretical understanding, simulation, and data manipulation are important part of this thesis along with experimental investigation.

Chapter 1 gives the introduction and objective of the thesis work. We have revisited the basic idea of quantum entanglement and its basic properties in chapter 2, . In later sections of the chapter 2, from the abstract idea of entanglement, we have discussed the manifestation of entanglement in different degrees-of-freedom in bi-photon modes generated through SPDC process. Subsequently, the scope of manipulation of bi-photon modes with structured beam also briefed. In chapter 3, we have demonstrated the high brightness entangled source based on type-0 phase matching in periodically poled crystal with Gaussian beam. As the degenerate spectrum has the maximum gain over non-degenerate spectrum in SPDC process, we employ degenerate non-collinear geometry to separate the signal and idler since both are in same polarization state. Using such scheme we will be presenting the spatial, spectral and entanglement characteristics in this chapter. To understand the effect of spatial and phase profile of the pump beam in SPDC process, we have demonstrated a new class of beam called "perfect" vortex beam in chapter 4. With help of such beam we have studied the angular spectrum of the SPDC photons. We have experimentally showed that the angular spectrum of the down converted photons is dictated by the spatial profile of the pump but not it's OAM. Investigation of vortex beam on polarization entangled bi-photon modes are included in chapter 5. We have showed that the bi-photon mode will have the same spatial profile as the pump beam while the polarization entanglement is unaffected. Further, in chapter 6, with help of classical non-separable state, where OAM and polarization degree of freedom are inseparable the beam, we have demonstrated the generation of hybrid entangled bi-photon state in SPDC process. With the measurement of witness parameter, we have verified that the generated state is entangled. In chapter 7, we have addressed the limitation of the Gaussian pump beam and subsequently we have showed that with help of asymmetric vortex beam, carrying superposition of multiple OAM, the more subspace in OAM Hilbert space can be accessed. We have verified the OAM content in pump as well as we have measured the OAM bi-photon modes generated in the SPDC process. Finally, we have concluded thesis work along with future outlook in chapter 8.

Chapter 2

Basics of quantum entanglement

In this chapter, with brief introduction to quantum entanglement we discuss different kind of entanglement and its properties. Later sections carry discussion about the source of entangled photons known as spontaneous parametric down conversion (SPDC) process. With the discussion of different parameters, phase-matching and pump transverse profile, which dictates the SPDC process, we give a brief introduction to different structured beam. Theoretical understanding, simulation, and data manipulation are very important part of this thesis along with experimental investigation.

2.1 Quantum entanglement

The name entanglement was introduced by Erwin Schrodinger to describe the peculiar connection between quantum systems following the argument by Einstein, Podolsky and Rosen [1] to question the completeness of quantum theory. Since then, entanglement between two quantum systems is of great interest in basic physics as well as in applications. The entangled systems have interesting properties such as non-locality and contextuality which make them a great resource for various quantum protocols. By definition, a combined system is said to be entangled when the total state cannot be expressed as a product of states corresponding to the individual sub systems such as,

$$\Psi \neq \Psi_1 \otimes \Psi_2,$$

where $\Psi_1$and Ψ_2 represent the wave functions of two different subsystem.

2.1.1 Polarization entanglement

Photon posses different degrees-of-freedom (DoFs) and the polarization is one of that. Polarization DoF is one of the best example for qubit system and it can be written in terms of horizontal ($|H\rangle$) and vertical ($|V\rangle$) polarization or right circular ($|R\rangle$) and left circular ($|L\rangle$) polarization or diagonal ($|D\rangle$) and anti-diagonal ($|A\rangle$) polarization. Simple qubit system can be written as,

$$\Psi = \frac{1}{\sqrt{2}}\left(|H\rangle + |V\rangle\right) = \frac{1}{\sqrt{2}}\left(|R\rangle + |L\rangle\right) = \frac{1}{\sqrt{2}}\left(|A\rangle + |D\rangle\right).$$

Corresponding polarized entangled state formed from such qubits are,

$$\Psi_{1\pm} = \frac{1}{\sqrt{2}}\left(|HH\rangle \pm |VV\rangle\right) = \frac{1}{\sqrt{2}}\left(|RR\rangle \pm |LL\rangle\right) = \frac{1}{\sqrt{2}}\left(|AA\rangle \pm |DD\rangle\right). \tag{2.1.1}$$

$$\Psi_{2\pm} = \frac{1}{\sqrt{2}}\left(|HV\rangle \pm |VH\rangle\right) = \frac{1}{\sqrt{2}}\left(|RL\rangle \pm |LR\rangle\right) = \frac{1}{\sqrt{2}}\left(|AD\rangle \pm |DA\rangle\right). \tag{2.1.2}$$

The four entangled state Ψ_{1+}, Ψ_{1-},Ψ_{2+}, and Ψ_{2-} are known as maximally entangled Bells states. All the Bells state violate CHSH Bell inequality [3], and the value of Bells parameter, S$\geq$ 2 with maximum value of 2.828. It is to be mentioned that for all separable state the Bells parameter S has value <2 with maximum of 2.

2.1.2 Orbital angular momentum (OAM) entanglement

Similar to the polarization, orbital angular momentum (OAM) is another important DoF which is widely used in quantum optics. Unlike polarization, having two dimension, the OAM DoF commonly represents with the integer value l, known as qudit, which forms infinite basis in Hilbert space. Therfore, the value of l can be varied from $-\infty$ to ∞, and it can give infinite dimensional entangled system. A qudit system can be written as,

$$\Psi = \sum_{l=-\infty}^{\infty} C_l \, |l\rangle \, .$$

Where, l is the topological charge and C_l is the eigen value corresponding to the state $|l\rangle$. The higher dimensional entangled state arise from such qudit can be written as [4],

$$\Psi_{entangled} = \sum_{l=-\infty}^{\infty} C_l \, |l, -l\rangle \, .$$

Where, C_l is the eigenvalue corresponding to the state $|l, -l\rangle$, with normalization condition $\sum_{l=-\infty}^{\infty} |C_l|^2$=1. The upper bound violation of CHSH bell inequality for 3 dimensional state is reported as, S=2.873 [5], which is higher than two dimensional entangled state (S=2.828) such as polarization entangled state.

2.1.3 Hyper entanglement

As we discussed in previous subsection, polarization and orbital angular momentum are independent DoFs, however, one can get both OAM entanglement and polarization entanglement in same two photon state. This kind of entanglement is known as hyper entanglement [6]. Such state can be written as ,

$$\Psi = \frac{1}{\sqrt{2}} (|HH\rangle \pm |VV\rangle) \otimes \frac{1}{\sqrt{2}} (|l, -l\rangle \pm |-l, l\rangle) \, .$$

It is to be noted that there is no entanglement between polarization and OAM. These states are highly useful in dense coding [7, 8], remote state preparation [9], and quantum correction [10].

2.1.4 Hybrid entanglement

In hybrid entanglement system, two different DoFs are entangled each other. In case of photon most common bases for such entangled state are OAM and polarization. The Hilbert space spanned by OAM and polarization bases are non-separable in such system, and are quite often used to study the quantum properties like non-local steering and complimentary [11, 12]. The wave function of biphoton system who's OAM and polarization DoF are entangled can be written as,

$$\Psi = \frac{1}{\sqrt{2}} \left(|H, l\rangle \pm |V, -l\rangle \right).$$

Where, OAM degree of freedom of one photon is entangled with polarization degree of freedom of another photon.

2.2 Spontaneous parametric down conversion

Almost all quantum information/entanglement experiments were first demonstrated with photons. One of the popular source of entangled photons is spontaneous parametric down conversion process (SPDC) [13, 14]. SPDC is a second order nonlinear optical process, where a high energy photon splits into two low energy daughter photons owing to the energy conservation. SPDC is said to be parametric process because there is no energy exchange take place between the medium and the interacting photons. Since these daughter photons are generated simultaneously they maintain a correlation among themselves in different DoFs including polarization, orbital angular momentum, time, path etc. This correlation leads to the entanglement of photon pair in those DoFs. The photon incident on the crystal very often referred as pump and the while the out going pair photon historically known as 'idler' and 'signal'. The wave function of the bi-photon generated through SPDC process can be written as [15],

$$|\Psi\rangle = \int\int \Phi(q_{1,}q_2)\widehat{a}^{\dagger}(q_1)\widehat{a}^{\dagger}(q_2)dq_1dq_2\,|0\rangle\,, \tag{2.2.1}$$

where $\widehat{a}^{\dagger}(q_1)$ and $\widehat{a}^{\dagger}(q_2)$ are the creation operator of a plane wave with transverse momentum q_1 and q_2 respectively. As q_1 and q_2 are transverse momentum of idler and signal photon, $\Phi(q_{1,}q_2)$ is the bi-photon amplitude or known as mode function. The complete form of bi-photon amplitude is

$$\Phi(q_{1,}q_2) = Sinc(\frac{1}{2}\triangle k_z L)A(q_p). \tag{2.2.2}$$

Where, $A(q_p)$ is transverse momentum of the pump beam ($q_p = q_1 + q_2$, is transverse momentum vector). $Sinc(\frac{1}{2}\triangle k_z L)$ is phase-matching function dictated by the crystal parameters and pump wave-vector. It is evident that to obtain the maximum bi-photon amplitude, the argument of *Sinc* function has to be zero. As L, non-linear crystal length, is always finite, maximum down conversion (maximum mode function) can be attained only if wave-vector mismatch,$\triangle k_z = 0$. Apparently, tuning $\triangle k_z$ to be zero is know as phase-matching condition. Along with that, spatial distribution of the bi-photon decided by the pump spatial profile as cleat from the second term, $A(q_p)$. These are the two important parameters, which decides the efficiency and properties of bi-photon modes.

2.2.1 Phase-matching

SPDC process happens accordance with energy and momentum conservation laws. The two conservation law, is defined as the sum of the wave-vector and energy, of the idler and signal, is equal to the wave-vector and energy of the pump photon, jointly known as phase-matching condition and it can be written as,

$$\overrightarrow{k_s} + \overrightarrow{k_i} = \overrightarrow{k_p} \tag{2.2.3}$$

$$\omega_s + \omega_i = \omega_p. \tag{2.2.4}$$

$\overrightarrow{k_s}, \overrightarrow{k_i}$, and $\overrightarrow{k_p}$ are the wave-vector of signal, idler and pump, respectively. Whereas ω_s, ω_i, and ω_p are the frequency of signal, idler and pump, respectively. As we discussed in the above section, the $\triangle k_z(= k_s + k_i - k_p)$, is the wave-vector mismatch between pump, idler and signal. The name phase-matching originated form the idea that, as $\triangle k_z = 0$, the proper phase relation between the pump, idler, and signal can be achieved through out the crystal. There are different technique to achieve phase-matching, and the most common techniques are birefringent phase-matching and quasi-phase matching. Birefringent phase-matching technique is achieved by exploiting the birefringent properties of nonlinear crystals, where the different plane of polarization experience different refractive index while propagating through crystal. Therefore, choosing proper polarization direction for the interacting photons, idler, signal and pump, one can achieve phase-matching. The polarization direction in the plane along the optic axis is known as extra-ordinary ray (e) and polarization orthogonal to the optic axis known as ordinary ray (o).

Birefringent phase-matching

Based on input and output polarization direction, birefringent phase-matching has classified in to type-I and type-II.

Type-I phase-matching: Where the polarization of input pump is orthogonal to the polarization of signal and idler . Which can be symbolically written as,

$$e_p \rightarrow o_s + o_i$$

and

$$o_p \rightarrow e_s + e_i$$

, where indices p, s, and i represent the polarization of pump, signal and idler. Figure 2.2.1 shows the pictorial representation of two different geometrical configuration in phase matching. In collinear configuration, generated down converted photons travel along with pump propagation axis, however, in non-collinear configuration the generated down converted photons travel with an angle, θ, with respect to the pump propagation axis. The second row of Fig. 2.2.1 shows cross sectional image of the collinear and non-collinear taken using CCD. As the collinear configuration gives intensity profile similar to the Gaussian intensity distribution, non-collinear configuration gives the ring shaped intensity distribution due to the fact that probability to the generate bi-photon in any azimuthal direction is equal. Therefore the any diametrical opposite points are highly correlated.

Type-II phase-matching: If idler/signal is orthogonal to the signal/idler of the SPDC photons, then it is called type-II phase-matching, and can be symbolically written as,

$$e_p \rightarrow e_1 + o_2$$

,where, indices p, s, and i represent the polarization of pump, signal, and idler. In type-II, the intensity profile in collinear configuration is same as in Fig. 2.2.1, however, in non-collinear configuration one can observe two rings corresponding to two different polarization as it shown in Fig. 2.2.2. Since the photons present in intersection point, marked with red circle, are indistinguishable in polarization basis, one can write this two point as superposition of two polarization bi-photon state. Such state can not be written as individual sub state of the each photon. Therefore this state is entangled in polarization basis.

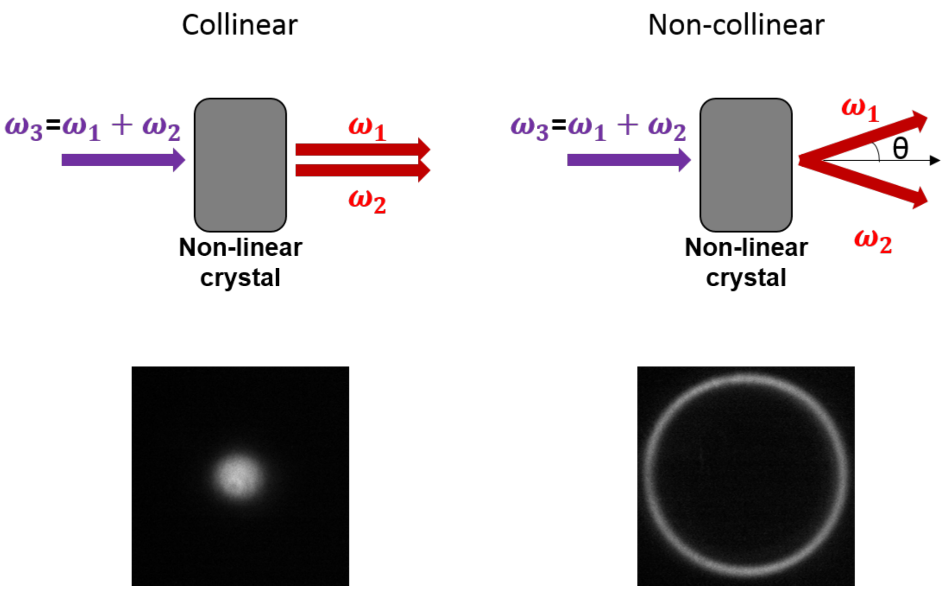

Figure 2.2.1: First row shows the pictorial representation of collinear and non-collinear phase-matching and the second row shows the intensity profile of the down converted photons generated in the respective configuration.

Quasi phase-matching

Quasi-phase matching in which, a crystal with spatially modulated nonlinear properties is used. In which, over some propagation distance crystal allow conversion of the pump frequency to signal and idler frequencies even though all the frequencies involved are not phase locked with each other. Conversion happens as long as phase between pump and signal/idler is less than 180 degrees and beyond it, the interaction would take place with the opposite direction of conversion. Therefore, to keep again conversion of the pump to signal and idler, crystal axis are flipped periodically.

Type-0: Unlike in birefringent phase matching condition, it is not necessary to have different polarization states in quasi phase-matching condition, in fact, it is most common to have equal polarization states, know as type-0 ($e_p \rightarrow e_s + e_i$) phase matching. Nevertheless, type-II can also be achieved in some crystals [16].

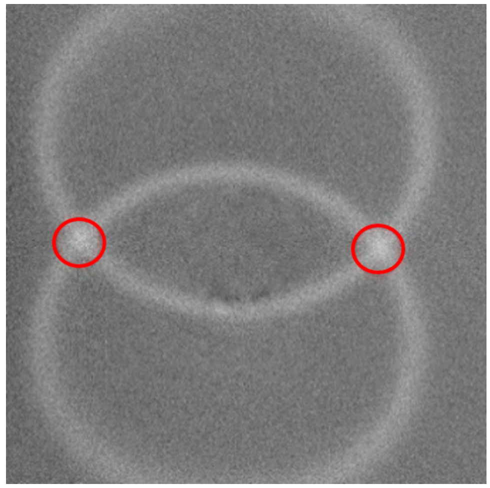

Figure 2.2.2: Intensity profile of the down converted photons generated under non-collinear type-II phase-matching condition.

2.3 Pump amplitude

As we discussed in section 1.2, the mode function or the bi-photon amplitude is dictated by the pump transverse amplitude, and it plays crucial role while developing any entangled system. It has been experimentally shown that the different pump profile can be transferred to the bi-photon amplitude [17, 12]. Therefore, it is essential to understand the different structured beam profile and its properties.

2.3.1 Gaussian beam

Gaussian beams, having the maximum intensity at the center and decreases exponentially away from the center, can be mathematically expressed in terms of a Gaussian function (Fig. 2.3.1 (a)). The intensity distribution of such beams can be described in terms of rectangular symmetric Hermite-Gaussian modes, and it can be written as [18]

$$\begin{aligned} G(x,y,z) &= \left(\tfrac{2}{\pi}\right)^{1/2}(1/w)\exp\left[-ik\left(x^2+y^2\right)/2R\right] \\ &\quad\times\exp\left[-\left(x^2+y^2\right)/w^2\right]\exp\left[-i\psi\right] \end{aligned}$$

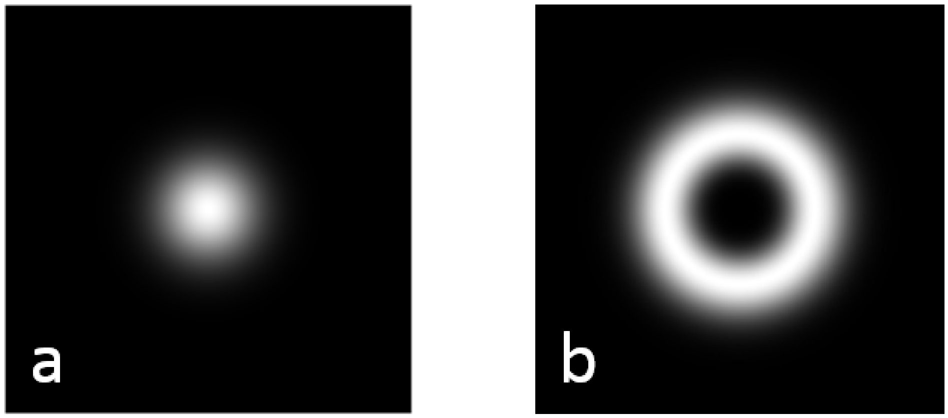

Figure 2.3.1: Intensity profile of (a) Gaussian beam and (b) Vortex beam.

This is the fundamental transverse mode which most of the lasers produce due to its high gain inside laser cavity.

2.3.2 Vortex beam

Optical vortex beams are having helical wave front with doughnut structure. Due to azimuthal varying phase distribution, the beam posses phase singularity at the center of the beam. The doughnut shaped intensity profile has zero intensity at the singular point given in Fig. 2.3.1 (b). Optical vortex beams carry orbital angular momentum (OAM) of $l\hbar$ per photon and characterized by topological charge (order), or winding number, l [19]. Due to doughnut spatial structure and OAM, the optical vortices find variety of scientific, industrial, and medical applications [20, 4]. Vortex beams are a special case of the Laguerre-Gaussian (LG) mode. The mathematical formula of Laguerre-Gaussian modes can be represented as

$$\begin{aligned} u_{lp}^{LG}(r,\phi,z) \quad = \quad & \left(\tfrac{2}{\pi l! p!}\right)^{1/2}(1/w)\exp\left[-ik\left(r^2\right)/2R\right] \\ & \times\exp\left[-\left(r^2\right)/w^2\right]\exp\left[-i\left(l+p+1\right)\psi\right] \\ & \times\exp\left[-il\phi\right](-1)^{min(l,p)}L_{min(l,p)}^{l-p}\left(2r^2/w^2\right)^{min(l,p)} \end{aligned}$$

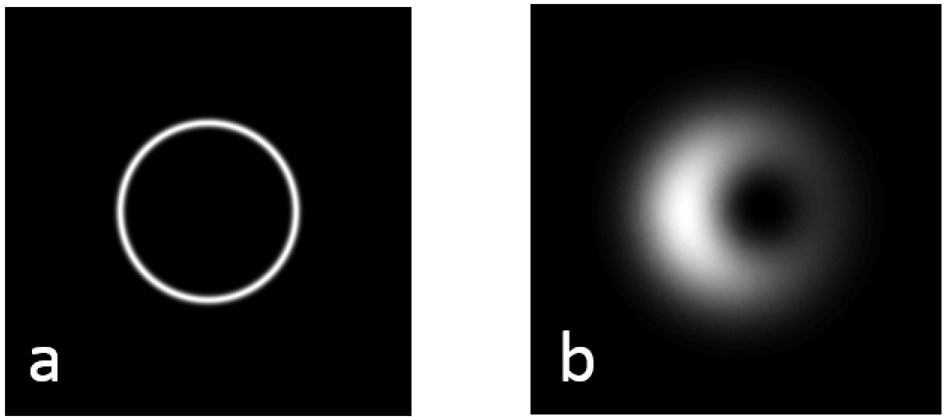

Figure 2.3.2: Intensity profile of (a) perfect vortex beam and (b) Asymmetric vortex beam.

here $L_p^l(x)$ is a generalized Laguerre polynomial with radial index p and azimuthal index l. The OAM arises due to the fact that the beam posses azimuthal component of the pointing vector which can be attributed to the the helical wave front of such beams. Since the argument of the LG function is depend on the azimuthal index, the size of the vortex beam vary with order l. These beams can be generated using spiral phase plates (SPPs) [21], q-plate [22] and spiral phase mirrors (SPMs) [23]. They can also be generated through spatial light modulators (SLMs) using holographic technique [24].

2.3.3 Perfect vortex beam

Recent developments in the field of structured beams provided a new class of optical vortex beam known as "perfect" vortex [25], in which size/area of the vortices are independent of its azimuthal index, l. Fig. 2.3.2 (a) shows the typical intensity profile of the perfect vortex beam, unlike the doughnut shaped intensity profile of vortices, perfect vortex beam have a ring shaped intesity profile. As the size and order are independent each other in perfect vortices, it is possible use such beam to study the individual contribution of phase profile (OAM) and spatial profile (size) in nonlinear interaction like second harmonic and down conversion processes.

Fourier transformation of the Bessel-Gauss (BG) beam of different orders is used to generate "perfect" vortices [25]. The complete form of complex field amplitude of the experimentally realizable "perfect" vortex of order l can be represented as [25]

$$\tilde{u}_n\left(\tilde{r},\tilde{\phi}\right) = i^{n-1}\frac{w_g}{w_0}\exp\left(-\frac{\left(\tilde{r}-\rho_r\right)^2}{w_0^2}\right)\exp\left(il\tilde{\phi}\right).$$

Where, w_g is the beam waist radius of the Gaussian beam confining the BG beam, $2w_o$ ($w_o = 2f/kw_g$, the Gaussian beam waist at the focus) is the annular width of the perfect vortex of ring radius governed by the relation, ρ_r is the radius of the ring, and l is the azimuthal index of the input BG beam.

2.3.4 Asymmetric vortex beam

Asymmetric optical vortex beam is a special class of vortex beam having asymmetric azimuthal intensity distribution with respect to the beam center. Near to the center of the beam, beam experiences symmetric phase variation with respect to the spatial modulators, however, away from the center in radial direction, beam experiences the unequal phase variation across the beam. Therefore, the total azimuthal index, l, become fractional and the index vary along with asymmetry of the beam. Such fractional order beam can be written in terms of different integer order vortex beam with different weightage. Asymmetric vortex beams are experimentally generated and observed that the beams carry broad OAM modal distribution [26]. The intensity distribution of the typical fractional asymmetric vortex beam is shown in Fig. 2.3.2 (b). The electric field equation for such beams can be written as [27],

$$u_l(r,\phi,z) = w^{-l}[q(z)]^{-(l+1)}[r\exp(i\phi) - q(z)x_0]^l \\ \times\exp\left[-\frac{r^2}{w^2(z)} + \frac{ikr^2}{2R(z)}\right].$$

where, w_g is the beam waist radius of the Gaussian beam confining the vortex beam, x_0 is the the distance between the center of the beam and optical axis of the phase modulators, and l is the azimuthal index.

Chapter 3

High brightness polarized entangled source

This chapter constitutes the following journal publication:

1. *Robust, high brightness, degenerate entangled photon source at room temperature*, **M.V. Jabir,** and G.K. Samanta, *Scientific Reports* 7, 12613 (2017)

3.1 Introduction

Entangled photon sources, a basic ingredient for many quantum optical experiments, are of paramount importance not only for the fundamental research [28] but also for a variety of applications in real world quantum communications [29] and quantum computing [30]. However, the realization of next generation envisaged projects towards the implementation of world-wide quantum network through ground-to-satellite and/or inter-satellite links [31, 32] require development of compact and robust entangled photon sources with high brightness, and entanglement purity. Over decades, a variety of schemes have been proposed and implemented [33, 34] for entangled photons, however, the polarization entangled photon sources realized through the spontaneous parametric down-conversion (SPDC) in second order, (χ^2), bulk nonlinear crystals remain the most appropriate choice.

Since, the parametric gain of SPDC process is low, efforts have been made to improve the brightness of the entangled photon sources by exploring different nonlinear crystals in bulk [35, 36] and waveguide [37] structures, different phase-matching geometries including type-II [38, 39, 40, 41, 42, 37], type-I [38] and type-0 [42, 43, 44], and different experimental schemes. Given that the length and nonlinearity are two important crystal parameters greatly influencing the overall gain of the SPDC process for a given pump laser intensity, the brightness of the entangled photon sources have been significantly improved over the years through the use of long periodically poled crystals engineered for high effective nonlinearity. As such, use of type-0, quasi-phase-matching (QPM) in periodically poled potassium titanyl phosphate (PPKTP) crystal in crossed-crystal geometry has produced collinear, non-degenerate paired photons at a spectral brightness as high as 0.278 MHz/mW/nm [44]. On the other hand, PPKTP crystals in type-II phase-matching have been extensively used in Sagnac-loop to produce narrow band entangled photons [45, 46] without exploiting the full advantage of high nonlinear co-efficient of the QPM crystals. Therefore, despite the generation of broadband entangled photons, the type-0 phase-matching is more favored over other phase-matching geometries to produce bright entangled photons. While one can expect further enhancement in the paired photons rate by operating the source at degeneracy, however, the separation and detection of individual photons of the collinear, co-polarized paired photons at degenerate wavelength is significantly difficult proposition. Attempt has been made to overcome such problem with the use of non-collinear, type-0, third order QPM in periodically poled lithium tantalate (PPSLT) crystal [47], however, the use of third order QPM resulted in moderately low rate of paired photons (98.5 kHz/mW). On the other hand, the requirement of active temperature control for non-critical phase-matching in periodically poled crystals increases the overall complexity of the sources. The success of future quantum communication experiments, in addition to other obstacles, demands engineering of high brightness entangled photon sources with minimal system complexities. In this chapter, we demonstrate a high brightness entangled photon source producing non-collinear, degenerate photons at 810 nm with spectral brightness as high as $\sim 0.41 \pm 0.02$ MHz/mW/nm. Based on a single, 30 mm long PPKTP crystal configured in a polarization Sagnac interferometer [48, 49, 50, 51, 52], the source produces entangled photon states violating the Bell's inequality by nearly 32 standard deviations and a Bell state fidelity of 0.975. The Table 3.1 represents the performance of our source as compared to some of the recent bright entangled photon sources based on PPKTP crystals.

Reports	Phase-matching	Detected spectral brightness (MHz/mW/nm)	Collection efficiency (%)	Fidelity (%)
Ref.[42]	Type-0	$0.22\ ^{(a)(b)}$	$31^{(c)}$	99.1
Ref.[43]	Type-0	$0.38\ ^{(a)(d)}$	-	99.3
Ref.[44]	Type-0	$0.298\ ^{(a)(e)}$	$18^{(f)}$	98.3
Ref.[40]	Type-II	$0.002^{(c)(g)}$	$6.6^{(c)}$	98
Ref.[50]	Type-II	$0.005^{(a)(b)}$	$16^{(c)}$	98.1
Our study	Type-0	$0.41^{(g)}$	$18.5^{(c)}/20^{(f)}$	97.5

Table 3.1: Comparison of the performance parameters of the SPDC sources based on PPKTP crystals. $^{(a)}$Nondegenerate photons, $^{(b)}$Sagnac interferometer, $^{(c)}$single mode fiber, $^{(d)}$double-pass, $^{(e)}$two crystals,$^{(f)}$multimode fiber, $^{(g)}$single-pass degenerate photons.

3.2 Experimental methods

The schematic of the experimental set up is shown in Fig. 3.2.1. A continuous-wave, single-frequency (linewidth $\leq$12 MHz) UV laser providing 100 mW of output power at 405 nm is used as a pump laser. A 30 mm long, 2×1 mm^2 in aperture, single grating, PPKTP (Raicol, Israel) crystal of period, $\Lambda = 3.425\ \mu$ m, is used for type-0 ($e \rightarrow e + e$)

phase-matched down conversion of pump beam at 405 nm. A convex lens of focal length, $f_1 = 300$ mm, is used to focus the pump beam at the center of the crystal. To generate entangled photons, we have devised a novel experimental scheme based on polarization Sagnac interferometer consisting of a dual wavelength polarizing beam splitter cube (D-PBS), a dual wavelength half-wave plate (D-$\lambda/2$) plate, and two high reflecting ($R > 99$ %) mirrors, M, at both 405 nm and 810 nm. The working principle of the scheme can be understood as follows. The $\lambda/2$ plate at 405 nm placed before the D-PBS controls the polarization of the pump beam in such a way that the reflection (vertical polarization, V) and transmission (horizontal polarization, H) ports of the D-PBS have equal laser powers. The V polarized pump photons travelling in clock-wise (CW) direction in the Sagnac interferometer, generate V polarized SPDC photons at 810 nm owing to type-0, non-collinear phase-matching in PPKTP crystal. The D-$\lambda/2$ plate transforms the polarization of both pump and the SPDC photons from H to V and vice versa. Therefore, the V polarized SPDC photons propagating in CW direction of the Sagnac interferometer transformed into H polarized photons and pass through the D-PBS. At the same time, the H polarized pump photons travelling in the counter clockwise direction (CCW) in the Sagnac interferometer transformed into V polarization after passing through the D-$\lambda/2$ plate and generate V polarized non-collinear SPDC photons in the same PPKTP crystal. The D-PBS combines the SPDC photons generated in both CW and CCW directions of Sagnac interferometer. Since both the CW and CCW pump beams follow the same path in opposite directions, and the PPKTP crystal is placed at a position symmetric to the D-PBS, the present experimental scheme is robust against any optical path changes to produce SPDC photons in orthogonal polarizations with ultra-stable phase. Using high reflecting mirrors, M, and two interference filters (IF) of different transmission bandwidths (2 nm and 10 nm) centered at 810 nm, the SPDC photons are collected and subsequently detected with the help of single photon counting module, SPCM (AQRH-14-FC, Excelitas). The analyzer, comprises a PBS and a $\lambda/2$ plate, is used to study the polarization entanglement of the generated photons. The lens pair, f_2 and f_3, images the crystal plane to the fiber tip used for photon collection. For all the measurements presented throughout the manuscript we have used a coincidence window of 8.1 ns.

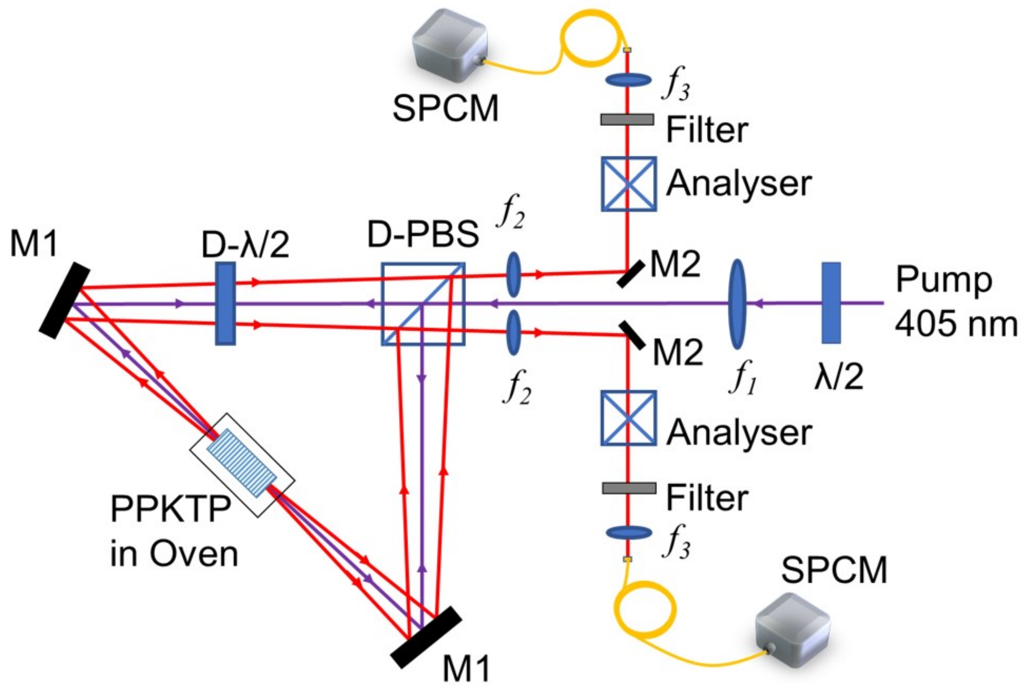

Figure 3.2.1: Schematic of the experimental setup. $\lambda/2$, half-wave plate at 405 nm; D-PBS, D- $\lambda/2$, polarizing beam splitter cube and half-wave plate at dual wavelengths, at 405 nm and 810 nm; M1-2, mirrors;f_{1-3}, lenses; PPKTP, nonlinear crystal in a temperature oven; Analyzer, polarization analyzer comprises a PBS and a $\lambda/2$ plate; IF, interference filter; SPCM, single photon counting module.

3.3 Results and discussion

3.3.1 Spatial and spectral characteristics of the SPDC source

To verify the generation of degenerate SPDC photons in non-collinear, type-0 phase matching, we pumped the crystal at an input power of 40 mW. Using a CCD camera (SP620U, Spiricon) along with an interference filter of spectral width $\sim$10 nm centered at 810 nm, we have recorded the angular spectrum or transverse momentum distribution of the SPDC photons in the Fourier plane using a convex lens of focal length, $f = 50$ mm in $f - f$ optical system configuration [53]. Since each pixel represents a particular transverse momentum of the SPDC photons, using the recorded spatial distribution of the SPDC photons we calculated the emission angle (half cone angle) of the photons at different crystal temperature with the results shown in Fig.3.3.1. As evident from Fig.3.3.1, the emission angle of the SPDC photons decreases from 2.15° to 0° with the increase of crystal temperature from 22°C to 35.5°C, clearly verifying the transition of the phase-matching of the SPDC photons from non-collinear to collinear geometry. While decrease in crystal temperature below 22°C results in further increase in the non-collinear phase-matching angle of the degenerate SPDC photons, the increase of crystal temperature beyond 35°C produces non-degenerate SPDC photons in collinear phase-matching geometry. A linear fit (not shown in the Fig.3.3.1) to the experiment data for the crystal temperature variation across 22°C to 29°C reveals that the emission angle (half cone angle) of the SPDC photons changes by 0.037°C for a change of 1°C in the crystal temperature. Such a small variation in the emission angle with the crystal temperature indicates the possibility of generation of entangled photons at room temperature without using any active temperature control, commonly required for non-critical phase-matching [54]. Using the Sellmeier equations [55] of PPKTP crystals and the equations for non-collinear phase-matching we theoretically calculated (solid line) the emission angle of the SPDC photons in good agreement with the experimental data (dots). The non-collinear generation and variation of the SPDC ring diameter with crystal temperature is also evident from the CCD images of the intensity distribution of the SPDC photons as shown by the inset of Fig.3.3.1. In contrary to the electron multiplying CCD (EMCCD) commonly used to record SPDC rings, here, the use of CCD camera signifies the generation of high number of SPDC paired photons in our experiment.

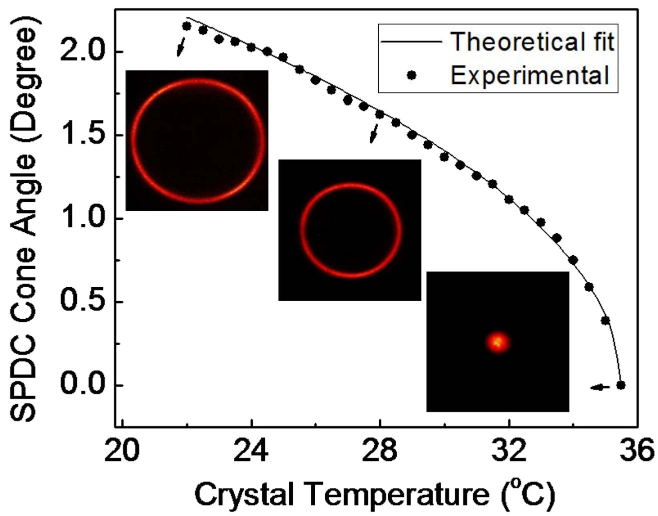

Figure 3.3.1: Variation of emission half-cone angle of the SPDC photons measured in free space with crystal temperature. Solid line corresponds to the theoretical fit to the experimental data. (Inset) CCD images of the SPDC ring at three crystal temperatures, 22°C, 28°C and 35°C

We have also studied the spectral distribution of the SPDC source at both non-collinear and collinear phase-matching geometries. Pumping the crystal with an input power of 40 mW and removing the interference filter we have measured the spectrum of the SPDC photons using a spectrometer (HR 4000, Ocean Optics) at different temperatures of the crystal. The results are shown in Fig.3.3.2(a). As evident from Fig.3.3.2(a), for the crystal temperature between 29°C to 35°C results in non-collinear, degenerate SPDC photons at 810 nm, however, further increase in the crystal temperature up to 65°C produces collinear, non-degenerate SPDC photons with wavelength tunability over $810-743$ nm in the signal wavelength (open circles) and $810-891$ nm in the idler (solid circle). The solid line is the tuning curve predicted from the Sellmeier equations of PPKTP crystal [55], confirming a reasonable agreement between the experimental data and theoretical calculations. Figure 3.3.2 (b) shows the measured spectra of the collinear SPDC paired photons at crystal temperature of 35°, 40°, 45°, 50°, 55°, and 60°C. It is evident from Fig.3.3.2(b) that the source produces degenerate SPDC photons at a spectral width (full width at half maximum, FWHM) of ∼31 nm centered at 810 nm, with a signature of high parametric gain of the PPKTP crystal. We also observed similar spectrum at crystal temperature below 35°C. However, the spectral width of the signal and idler photons decrease with the increase of crystal temperature away from degeneracy. From the normalized intensity of the SPDC photons, it is also evident that the development of SPDC source with high brightness requires operation of the periodically poled crystal based sources in degenerate, non-collinear, type-0 phase matching geometry.

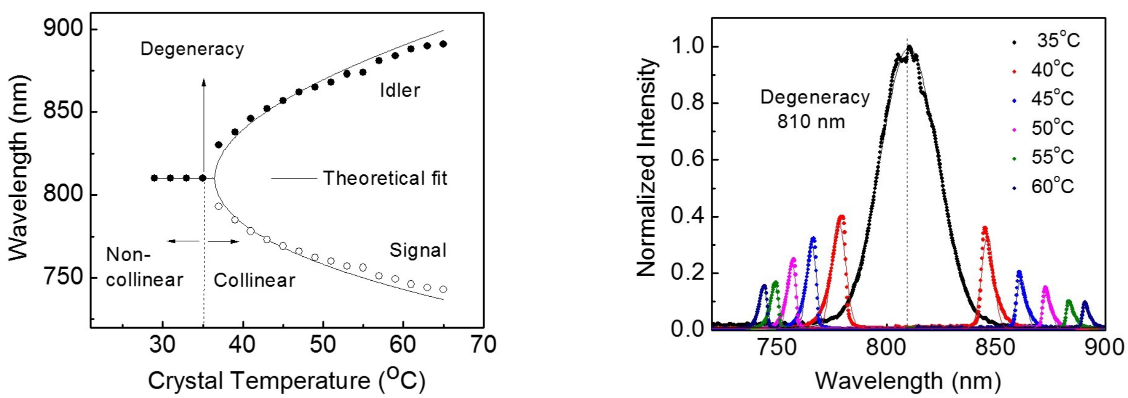

(a) (b)

Figure 3.3.2: (a)Wavelength tuning of the SPDC photons as a function of crystal temperature. (b) Emission spectra of the SPDC photons recorded at different crystal temperatures.

3.3.2 Detection and characterization of the SPDC photons using both multimode and single mode fibers

After successful generation of degenerate, non-collinear SPDC photons using type-0 phase-matched PPKTP crystal, we characterized the source in terms of spectral brightness and efficiency. In order to collect photons from two diametrically opposite points of the SPDC ring we have used the imaging systems consist of two convex lenses of focal lengths $f1$

and $f2$, in $2f1-2f2$ configuration to image the crystal plane to the tip of the fiber connected to SPCM. For comparison, we have used both multimode(MMF) and single mode fibers(SMF) separately to measure the spectral brightness of the photons collected from two diametrically opposite points of the SPDC ring filtered with the interference filter(IF) of bandwidth $\sim$2 nm at different pump beam focusing and pump power. The results are shown in Fig.3.3.3. As evident from Fig.3.3.3(a), for a constant pump beam power of 0.25 mW and crystal temperature of 29°C the spectral brightness of the paired photons, collected using multimode fiber and the imaging system having lenses of focal lengths, $f_1 = 50$ mm and $f_2 = 5$ mm, vary from $1.98 \pm 0.02 \times 10^5$ Hz/mW/nm to $2.73 \pm 0.02 \times 10^5$ Hz/mW/nm with the pump beam waist radius varying from 4 μ m to 139.5 μ m clearly showing a maximum spectral brightness of $4.19 \pm 0.03 \times 10^5$ Hz/mW/nm at optimum pump beam waist radius of 59 μ m. We have also measured the dependence of the spectral brightness with the pump power at two different crystal temperatures, 22°C and 29°C. The results are shown in Fig.3.3.3(b). As expected, the spectral brightness increases linear to the pump power (see Fig.3.3.3(b)), at a slope of, $N_c = 3.13 \pm 0.01 \times 10^5$ Hz/mW/nm, and $N_c = 3.92 \pm 0.01 \times 10^5$ Hz/mW/nm at crystal temperature 22°C (open circle) and 29°C (closed circle) respectively. Using the photon numbers, $N_1 \sim N_2$ recorded from two diametrically opposite points on the SPDC ring and their spectral brightness, N_c in the equation, $N_{Pair}=N_1 \times N_2/N_c$ [47], we can estimate the spectral brightness to be as high as $\sim 8.05 \pm 0.03$ MHz/mW/nm and $\sim 10.16 \pm 0.02$ MHz/mW/nm at 22° C and 29° C respectively. Such a high number of non-collinear degenerate paired photons as compared to previous reports, can be attributed to high parametric gain resulting from the use of long crystal length and first order grating period of the PPKTP crystal. To the best of our knowledge, this is so far, the highest detected non-collinear, degenerate paired photons from a bulk crystal based SPDC source.

Given that the parametric gain is almost constant near the degeneracy and the SPDC is a very feeble nonlinear process, one can, in principle, expect the number of detected paired photons to be constant with crystal temperature. However, as evident from Fig.3.3.3(b),

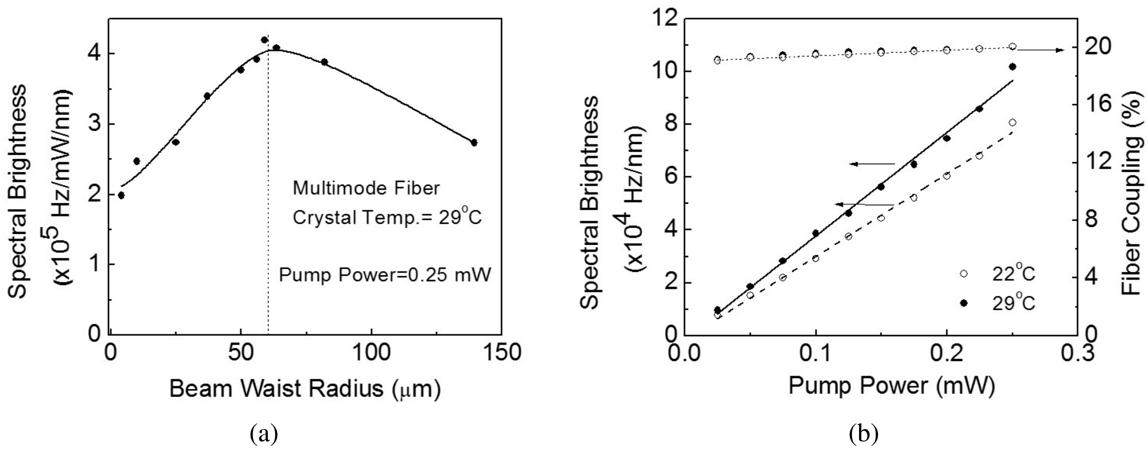

Figure 3.3.3: (a) Dependence of spectral brightness of the paired photons on the pump beam waist at crystal temperature of 29° C, and (b) the variation of spectral brightness and fiber coupling efficiency on the pump power at crystal temperature 22° C (open circles) and 29° C (solid circles) for photon collection using multimode fiber.

we observed a change in spectral brightness with crystal temperature. Such effect can be understood as follows. Given that the number of SPDC photons is constant at constant pump power, and distributed over the annular area of the SPDC ring, the linear decrease in the radius of the SPDC ring with the increase in crystal temperature from 22° C to 29° C results in a quadratic increase in the number density (number of photons per unit area per sec). Therefore, spectral brightness measured using the fixed aperture size of the detection system show the change with the crystal temperature. Here, we can conclude that for high brightness SPDC source one need to adjust the crystal parameters to access the optimum size of the SPDC ring. One can in principle, adjust the grating period of the PPKTP crystal to access such high brightness of the SPDC source at any favorable crystal temperature. The coupling efficiency calculated using the equation, $\xi = {}^{Nc}/\sqrt{(N1 \times N2)}$, for different pump powers, as shown in Fig.3.3.3(b), remains almost constant in the range of 19% to 20% at both crystal temperatures. Using the same experimental condition, we have verified the room temperature operation of the source by measuring the coincidence and singles counts without using temperature oven. At the lab temperature of 23°C, we observed the spectral brightness of the source to vary with a standard deviation as low as ∼1.6% over two hours.

Further, we characterized the SPDC source using single mode fibers. Pumping the crystal at a constant power of 0.25 mW and temperature ∼29° C we measured the photon spectral brightness collected using the single mode fiber and the imaging systems comprise lenses of $f_1 = 100$ mm and $f_2 = 2$ mm for different pump beam waist radius. As evident from Fig.3.3.4(a), the spectral brightness varies from $0.164 \pm 0.004 \times 10^4$ Hz/mW/nm to $0.336 \pm 0.006 \times 10^4$ Hz/mW/nm with the pump beam waist radius varying from 4 μm to 139.5 μm clearly showing a maximum spectral brightness of $2.50 \pm 0.02 \times 10^4$ Hz/mW/nm at optimum pump beam waist radius of 41 μm. Keeping the pump beam waist radius at optimum value of 41 μm, we have measured the variation of spectral brightness with the pump power. As evident from Fig.3.3.4(b), the number of paired photons (spectral brightness) increases linear to the pump power at a slope of $N_c = 2.43 \pm 0.01 \times 10^4$ Hz/mW/nm resulting maximum paired photons of $6.18 \pm 0.01 \times 10^3$ Hz/nm at a pump power of 0.25 mW. The corresponding maximum number of paired photons produced in the SPDC process can be calculated to be $N_{Pair} = 0.74 \pm 0.01$ MHz/mW/nm. The coupling efficiency is almost constant at∼18.45% for all the pump powers.

3.3.3 Entanglement properties of the source

With the successful generation of paired photons with high brightness, we study the source for the generation of polarized entangled photons. Since in type-0 phase-matching geometry, the generated paired photons have the same state of polarization as that of the pump photons, we placed the PPKTP crystal along with a D-$\lambda/2$ plate inside the polarization Sagnac interferometer and pumped in both CW and CCW directions with same state of polarization (see Fig. 3.2.1), vertical ($|V\rangle$). The non-collinear SPDC photons generated in both the directions are superposed using the PBS after changing the polarization state of the photons generated in one of the directions by the D-$\lambda/2$. To verify the non-collinear

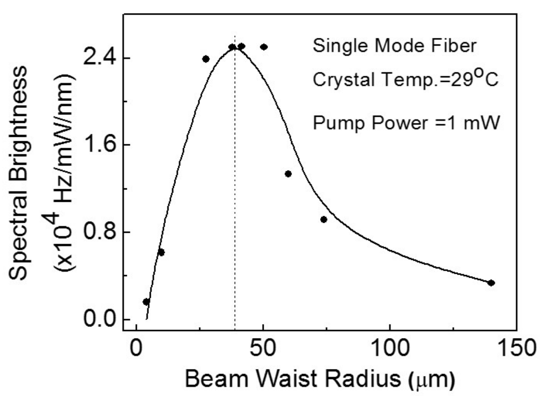

(a)

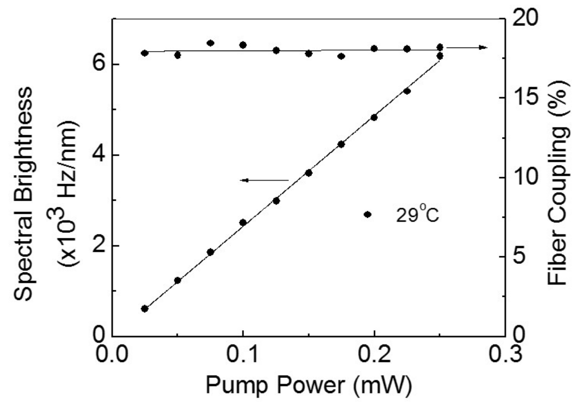

(b)

Figure 3.3.4: (a) Dependence of spectral brightness of the paired photons on the pump beam waist, and (b) the variation of spectral brightness and fiber coupling efficiency with the pump power at crystal temperature of 29° C for photon collection using singlemode fiber. Lines are guide to the eye.

generation of SPDC photons for both pump directions, and their superposition as required for entanglement, we have recorded the intensity distribution of the SPDC photons using an EMCCD (ANDOR, DU-897U-CS0-BVAntiF) at pump power of 5 mW. The results are shown in Fig. 3.3.5. Adjusting the polarization state, horizontal $|H\rangle$, and or vertical $|V\rangle$, of the pump beam to the PBS, we pumped the PPKTP crystal in CCW and or CW directions, respectively. Figure 3.3.5(a) and 3.3.5(b) show the spatial distribution of the SPDC photon with polarization states, $|HH\rangle$ and$|VV\rangle$ generated in CW and CCW, respectively. It is evident that the PPKTP crystal in the current experimental architecture produces indistinguishable SPDC rings of orthogonal polarization states, $|HH\rangle$ and$|VV\rangle$, which is further confirmed from the Fig. 3.3.5(c) and Fig. 3.3.5(d) representing the images of the SPDC rings under misalignment and perfect alignment of the source, respectively. Under perfect alignment, the twin photon states can expected to be, $\psi = 1/\sqrt{2}(|HH\rangle + |VV\rangle)$. However, one need quantum state tomography study to ascertain the actual twin photon state.

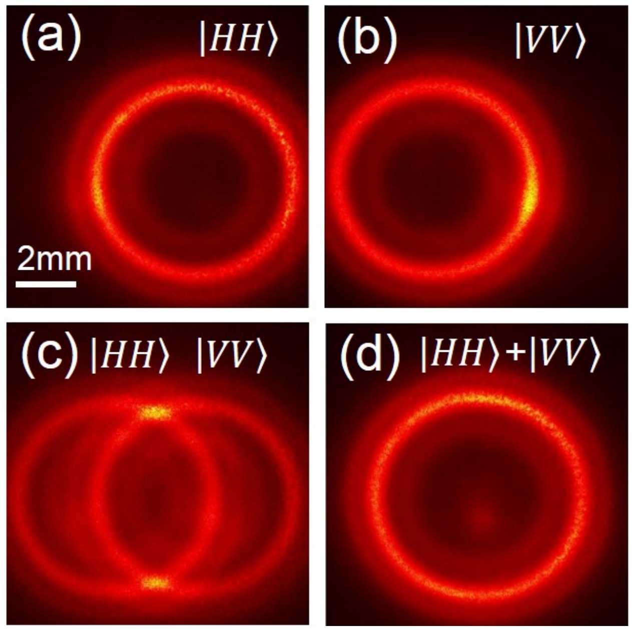

Figure 3.3.5: Images of the paired photons of polarization state, (a) $|HH\rangle$, (b) $|VV\rangle$, (c) both $|HH\rangle$ and $|VV\rangle$ with misalignment, and (d) perfectly overlapped states, $|HH\rangle$ and $|VV\rangle$. The black circles represent the diametrically opposite regions on the SPDC ring used for entanglement studies. The pump power used for this measurement is 5 mW.

For quantitative analysis of the polarized entanglement of the source, we pumped the crystal with a total power of $\sim$1 mW at crystal temperature $\sim$29° C and aligned the system to maintain perfect overlapping of the SPDC rings. Using standard coincidence measurement technique we recorded the two-photon interference in terms of photon coincidence between the twin photons distributed in two diametrically opposite points of the SPDC ring under two non-orthogonal projection bases, H/V (horizontal/vertical) and D/A (diagonal/anti-diagonal). The photon detection system comprised with two lenses of focal length, $f_1 = 150$ mm and $f_2 = 5$ mm in $2f_1 - 2f_2$ configuration, an interference filter of bandwidth $\sim$2 nm, polarization analyser, multimode fiber, and SPCM. The results are shown in Fig. 3.3.6. As evident from Fig. 3.3.6, we observed a typical quantum interference of the polarized entangled photons for H/V(solid cicles) and D/A(open circles) projections for the crystal temperature 29° C. The solid lines are best fit to the experimental data. The number of detected entangled paired photons has a maximum value of 0.32 ± 0.02 MHz/mW/nm, close to the detected paired photons ($N_c = 3.92 \pm 0.01x105$ Hz/mW/nm) presented in Fig. 3.3.3. Such small difference can be attributed to the use of longer focal length, $f_1 = 150$ mm, of the detection system to avoid mechanical constraint in the experimental setup. The interference fringe visibility in H and D projections are estimated to be 98.2±0.3% and 72.8±0.4% respectively. The measured fringe visibility under both bases are higher than 71%, sufficient to violate Bell's inequality. Using the coincidence rates, we measured the Bell's parameter to be S= 2.19±0.03, violating the Bell's inequality by more than 6 standard deviations, a clear indication of polarization entanglement of the generated two-photon states. The lower values of fringe visibility in diagonal projection can be attributed to the relative phase among the higher order spatial modes in the SPDC process collected by the multimode fiber, which can be improved through proper phase compensation schemes [56].

Similarly, we have studied the polarization entanglement using single mode fiber with the results shown in Fig 3.3.7. As evident from Fig. 3.3.7, the number of detected entangled paired photons has a maximum value of 1.88×10^4 Hz/mW/nm at 0.5 mW of pump power. However, the interference fringe visibility in H (solid circles) and D (open circles) projections are measured to be $97.4 \pm 0.2\%$ and $96.9 \pm 0.3\%$. Using the coincidence counts we have calculated Bell's parameter to be S= 2.63 ± 0.02 clearly violating the Bell's inequality by nearly 32 standard deviations. Such study clearly shows the generation of high quality entangled photons with high brightness even in the absence of any phase compensation schemes commonly used for SPDC based entangled photon sources. The table 3.2 summaries various experimental results of the SPDC source.

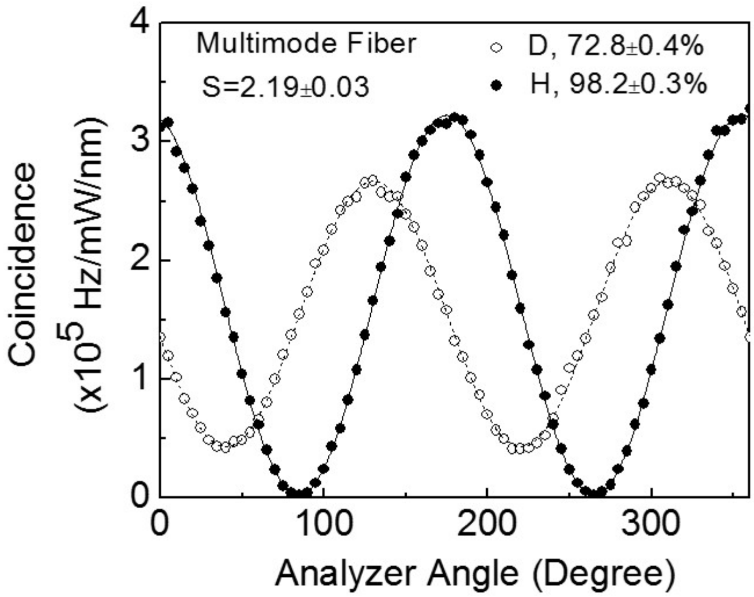

Figure 3.3.6: Quantum interference of the entangled photons at horizontal, H (solid circles) and diagonal, D (open circles) projection bases for crystal temperature 29° C collected using multimode fiber

We have also studied the effect of pump power on the entanglement quality of the paired photons by measuring the visibility of quantum interference fringes at different pump powers with the results shown in Fig. 3.3.8. Like previous report[39], here, we have also observed that the fringe visibility in both H and D projections decrease with the pump power resulting a fringe visibility of 70.8% and 68.9% in H and D projections respectively, below the fringe visibility limit of 71% for entanglement,even for the pump power as low as 5 mW. Such degradation in the entanglement quality with the increase of pump power can be attributed to the multi-pair generation due to high gain in the PPKTP crystal. To verify the robustness of our entangled photon source, we have measured the fluctuation in the spectral brightness at H-H projection collected using single mode fiber. Keeping the pump power constant at 0.5 mW, we have recorded the coincidence of the paired photons with an

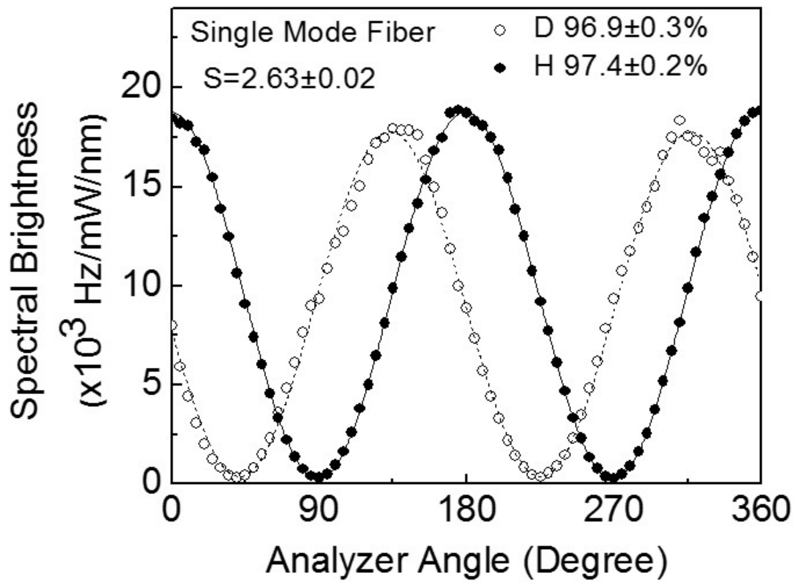

Figure 3.3.7: Quantum interference of the entangled photons at horizontal, H (solid circles) and diagonal, D (open circles) projection bases for crystal temperature 29° C collected using single mode fiber

exposure of one second over 3600 seconds with the results shown in Fig. 3.3.8(a). As evident from Fig. 3.3.8(a), the spectral brightness of the SPDC source fluctuate at a standard deviation of 0.065 ± 10^4 Hz/nm over the average spectral brightness of 1.97×10^4 Hz/nm for 0.5 mW, corresponding to an estimated passive fluctuation as low as $\sim$3%. Similarly, in D-A projection we measured the fluctuation in spectral brightness at a standard deviation of 0.074×10^4 Hz/nm with an estimated passive fluctuation of $\sim$4.7%, slightly higher than that of H-H projection. Such instability of the SPDC source can further be improved with proper isolation of the source from the temperature fluctuation and air turbulence of the laboratory environment. To find the degree of entanglement of the photon states for the SPDC source we have constructed the density matrix of the state using linear tomographic technique [57]. The inset of Fig. 3.3.8(b) shows the graphical representation of the absolute values of the density matrix of the generated states. From the analysis, we determine

Collection Fiber	Detected spectral brightness (MHz/mW/nm)	Estimated spectral brightness (MHz/mW/nm)	Coupling efficiency (%)	Visibility (%) H/D bases	Fidelity (%)
Single mode	0.024	0.74	18.5	97.4±0.2/ 96.9±0.3	97.5
Multimode	0.41	10.16	20	98.2±0.3/ 72.8±0.4	

Table 3.2: Performance parameters of the SPDC source measured using both single mode and multimode fibers at the crystal temperature of 29° C.

the state to be, $\psi = 1/\sqrt{2}(|HH\rangle - |VV\rangle)$ with state fidelity of 0.975. Since the relative phase between the CW and CCW beams of the Sagnac interferometer is determined by the position of the crystal [52], we can transform the output state, $\psi = 1/\sqrt{2}(|HH\rangle - |VV\rangle)$ into $\psi = 1/\sqrt{2}(|HH\rangle + |VV\rangle)$ and vice versa by simply adjusting the crystal position with respect to the PBS in our experimental setup.

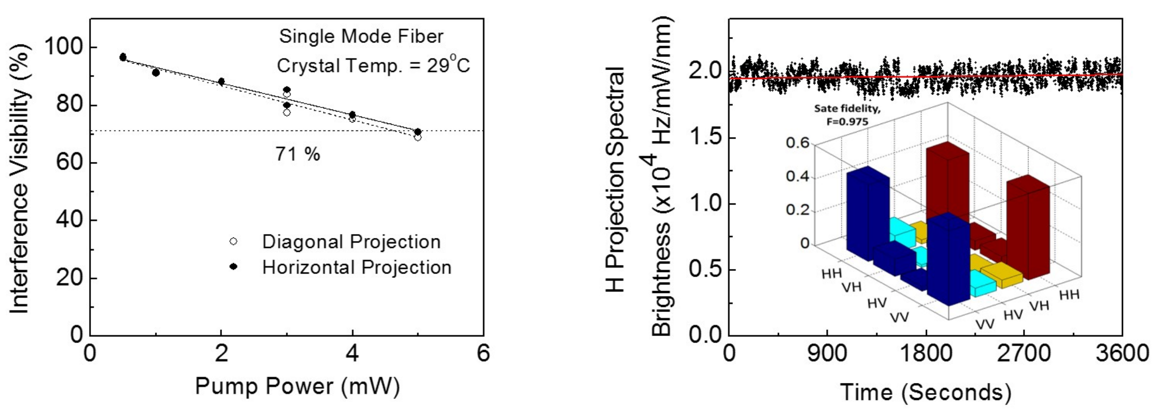

(a) (b)

Figure 3.3.8: (a) Dependence of spectral brightness of the paired photons on the pump beam waist, and (b) the variation of spectral brightness and fiber coupling efficiency with the pump power at crystal temperature of 29°C and the inset shows graphical representation of the absolute values of the density matrix of the polarization entangled photon states. Lines are guide to the eye.

3.4 Conclusion

In conclusion, we have demonstrated a simple, compact and robust source of entangled photons at high brightness. Based on non-collinear, degenerate, type-0 phase-matching of a single PPKTP crystal at room temperature in a Sagnac interferometer, the source produces a detected paired photons rate of 0.41±0.02 MHz/mW/nm. To the best of our knowledge, this is the highest number of degenerate paired photons detected with the help of multi-mode fiber from a bulk crystal pumped with a continuous-wave laser. The polarization correlation study and quantum tomography measurement using single mode fibers reveals that the source produces entangled photon states violating the Bell's inequality by nearly 36 standard deviations and a Bell state fidelity of 0.975. Such high brightness entangled photon source in compact and rugged architecture is ideal for the many present and future experiments in the field of quantum optics especially in quantum communications.

Chapter 4

Effect of pump profile on angular spectrum of SPDC photons

This chapter constitutes the following journal publications:

1. *Generation of "perfect" vortex of variable size and its effect in angular spectrum of the down-converted photons*,
   M.V. Jabir, Apurv Chaitanya N., A. Aadhi, and G. K. Samanta,
   Scientific Reports 6, 21877 (2016)

4.1 Introduction

Spontaneous parametric down-conversion (SPDC) [13, 14], one of the most important nonlinear processes, is of paramount interest especially in the field of quantum optics [58] for its intrinsic capability in generating entangled photon pairs. In this process, a photon (pump) of higher energy while interacting with second order nonlinear crystals splits into a pair of low energy photons (signal-idler) subject to energy conservation and phase matching. Depending upon the phase matching conditions inside the nonlinear crystals, the down converted photons are known to be emitted in variety of spatial distributions. For example, pump beam of Gaussian mode under type-I (where the signal and idler have same polarization but orthogonal to the pump polarization), non-collinear phase-matching produces down converted photons in an annular ring, with photon of each pair at diametrically opposite points. As such, these photon pairs are entangled in the spatial degrees of freedom [59] and other degrees of freedom including orbital angular momentum (OAM) [4]. The angular spectrum and hence the entanglement properties of these paired photons are highly influenced by different crystal parameters including birefringence and length, and the spatial structure of the pump beam [60]. Therefore, it is imperative to study the angular spectrum of the SPDC photons for different crystal parameters and pump beams of different spatial structures and OAM.

Optical vortices having phase singularities (phase dislocations) in the wavefront, carries vanishing intensity at the singular point. Due to the screw-like (helical) phase structure around the point of singularity, such beams carries OAM. The characteristic phase distribution of optical vortices is represented as $\exp(il\theta)$, where θ is the azimuthal angle. The integer l is called the topological charge or the order of the vortex. It has been observed [17] that the OAM of the classical beam can be transferred to the heralded single photon generated through SPDC process. Therefore, it is important to study the spatial distribution of the SPDC photons while pumped with different order optical vortices. Recently, there have been report [61] that unlike Gaussian beam, the vortex pump beams produce SPDC photons in asymmetric annular rings and the asymmetry increases with the order of the vortex. As the divergence [24] and the radius of the vortex beam increases with its order [62], it is difficult to ascertain the contribution of the spatial distribution of the vortex beam and it's OAM in the asymmetry of SPDC ring separately.

Recent development in the field of structured beams have resulted in a special class of optical vortices, known as perfect vortices [25], where the radius of the vortex ring is independent of its order. The experimentally realizable annular field profile of the perfect vortex with topological charge l at a fixed propagation distance may be written as [63]

$$E(\rho,\theta) \equiv exp\left(\frac{-(\rho-\rho_r)^2}{(\Delta\rho)^2}\right)exp(il\theta) \tag{4.1.1}$$

where, (ρ,θ) are polar coordinates, ρ_r and $\Delta\rho$ are the radius and annular width of the perfect vortex. Among different techniques [63, 64, 65], Fourier transformation of the Bessel-Gauss (BG) beam of different orders [65] is the simplest technique to generate perfect vortices. The axicon, an optical element with a conical surface, converts Laguerre-Gaussian (LG) beams into BG beams [66, 67]. The order of the BG is the same as that of the input LG beams. The Gaussian (zero order LG beam) input beam results in 0th order BG beam. Fourier transformation of such BG beams using a lens of focal length, f, results perfect vortex at the back focal plane with field amplitude distribution given as [64]

$$E(\rho,\theta) = i^{(l-1)}\frac{w_g}{w_o}exp(il\theta)exp\left(\frac{-(\rho^2+\rho_r^2)}{(w_o^2)}\right)I_l\left(\frac{(2\rho_r\rho)}{(w_o^2)}\right) \tag{4.1.2}$$

where, w_g is the beam waist radius of the Gaussian beam confining the BG beam, I_l is the lth order modified Bessel function of first kind, and $2w_o$ ($w_o = 2f/kw_g$, the Gaussian beam waist at the focus) is the annular width of the perfect vortex of ring radius governed by the relation,

$$\rho_r = f sin((n-1)\alpha) \tag{4.1.3}$$

where, n and α are the refractive index and base angle of the axicon respectively. As evident from Eqn. (3.1.3), for given axicon parameters, the radius of the perfect vortex is constant for a lens and linearly varying with the focal length of the Fourier transforming lens.

However, for all practical purposes [63, 68], one need to vary the radius of the vortex ring, which requires either a number of Fourier transforming lenses of different focal lengths and or imaging systems of different demagnification factors. As such, both of these options can provide variation (only discrete values) in the vortex ring radius, definitely, at the cost of increased experimental complexity. Here we present a novel technique to generate perfect vortices with continuously varying annular ring radius. As a proof of principle, we have generated perfect vortices of topological charge as high as l=6 with annular ring radius continuously varying from 0.3-1.18 mm. This novel experimental scheme can potentially be used as a quick and simple technique to measure the apex angle of an axicon. Pumping a nonlinear crystal using such vortices of different ring radius we have studied the angular spectrum of the down converted photons and experimentally observed that the angular spectrum of the down converted photons is dictated by the spatial profile of the pump but not it's OAM. However, the asymmetry in the angular spectrum which is detrimental to the entanglement quality of the SPDC source [69], depends on the size of the input beam. Using the variable size perfect vortex we have experimentally found for given a nonlinear crystal (birefringence parameter and length) the input beam radius generating the symmetric angular spectrum of the down converted photons.

4.2 Theory

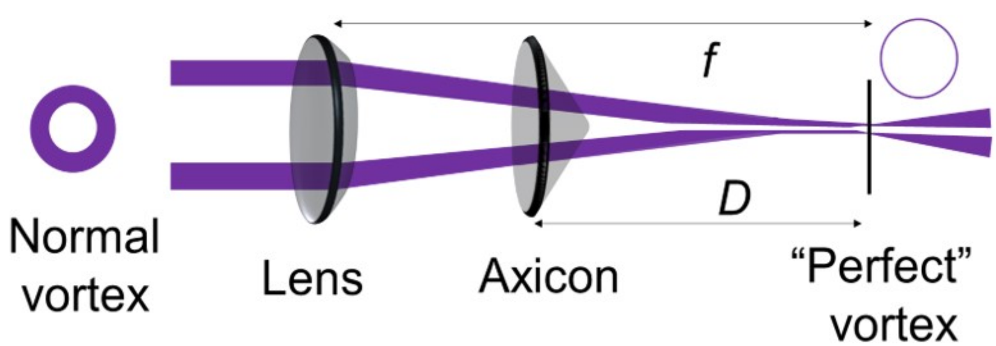

Figure 4.2.1: Pictorial representation of the generation of variable size perfect vortex by using lens-axicon combination.

According to the Fourier transformation theory [70], any object can be Fourier transformed by placing the object behind the lens at any arbitrary distance D from the focal plane. The basic principle of the technique is pictorially represented in Fig. 4.2.1, where the object (axicon) placed at a distance $(f-D)$ behind the lens of focal length, f, is Fourier transformed into perfect vortex at the back focal plane for input vortex beams. The amplitude distribution of the perfect vortex at the back focal plane is given by

$$E(\rho,\theta) = i^{(l-1)} exp\left(\frac{ik\rho^2 f^2}{2D^3}\right)\frac{w_g}{w_D} exp(il\theta) \times$$
$$exp\left(-\frac{[\rho f/D]^2+\rho_r^2}{w_D^2}\right) I_l\left(\frac{2\rho_r[\rho f/D]}{w_D^2}\right) \tag{4.2.1}$$

In the current system configuration, the width of the perfect vortex is $2w_D$=1.65 x $2w_o$ [65]. For large value of ρ_r, the modified Bessel function, I_l can be approximated to [64]

$$I_l\left(\frac{2\rho_r[\rho f/D]}{w_D^2}\right) \sim exp\left(\frac{2\rho_r[\rho f/D]}{w_D^2}\right) \tag{4.2.2}$$

Therefore, Eqn. (3.2.1) can be reduced to

$$E(\rho,\theta) = i^{(l-1)} exp\left(\frac{ik\rho^2 f^2}{2D^3}\right)\frac{w_g}{w_D} exp\left(\frac{-[\rho f/D-\rho_r]^2}{w_D^2}\right) exp(il\theta) \tag{4.2.3}$$

The Eqn. (3.2.3) has similar functional form as Eqn. (3.1.1) with additional quadratic phase factor and a scale factor. As we are dealing with the intensity of the perfect vortex beam at focal plane, the quadratic phase does not make any difference in our current study. The perfect vortex ring is formed at, $\rho = \rho_r D/f$ with a modified ring radius,

$$\rho_r = Dsin((n-1)\alpha) \tag{4.2.4}$$

As evident from Eqn. (3.2.4), the radius of the perfect vortex can be varied simply by moving the axicon away from the back focal plane of the lens. For ring radius ρ_r to be zero the axicon required to be placed at the focal plane of the lens which is impractical for many applications. On the other hand, for $D \rightarrow 0$, the Fourier transform relation breaks down. Therefore, the value of D can be varied practically within the range of $0 < D < f$.

4.3 Experimental methods

The schematic of the experimental setup is shown in Fig. 4.3.1. A pump diode UV laser (Toptica- TopMode 405) of 100 mW at 405nm with spectral width ~12 MHz is used as the pump laser. The power to the nonlinear crystal is controlled by using a combination of half-wave plate (λ/2) and polarising beam splitter (PBS1) cube. Two spiral phase plates, SPP1 and SPP2 are used to convert Gaussian beam into optical vortices (LG beams) of order, l=1 and l=2, respectively, at conversion efficiency >95%. Due to limited availability of SPPs producing vortices of order l >2, we have used a vortex-doubler setup [71] comprised of a polarizing beam splitter cube (PBS 2), quarter-wave plate ($\lambda/4$), and dielectric coated mirror, M1, with high reflectivity at 405nm. The working principle of the vortex doubler can be understood as follows. The Gaussian beam in horizontally polarization passes through the PBS2. In forward pass through the SPP1 the Gaussian beamacquires spiral phase corresponding to vorticity of order l=+1 (say). The λ/4 plate having its axes at 45° to its polarization axis converts the polarization of the beam into left circular polarization. The mirror, M, reverses both the polarization handedness (left circular to right circular) and sign of the vorticity (l =+1 to -1) of the reflected beam.The right circularly polarized beam on return pass through the $\lambda/4$ plate gets converted into vertical polarization. To the return beam (l= -1), the direction of phase variation of the SPP1 is opposite to that of the forward pass. Therefore, the return beam acquires additional spiral phase resulting total vorticity, l= -2, twice the phase winding of the SPP placed inside. Since the return beam have vertical polarization, it gets reflected by the PBS2. Using different combinations of

SPP1 and SPP2, placed inside and outside of the vortex-doubler we have generated optical vortices of orders (topological charges) up to l=6.

An antireflection coated 1” diameter axicon made of BK-7 glass having apex angle 178° is used to convert the vortex beam of order l into BG beam of the same order. As shown in Fig. 4.2.1, the Fourier transforming lens (f=200 mm) placed before the axicon with a separation of $f-D$ (D is the distance of the axicon from Fourier plane) produces the perfect vortices at its back focal plane. To measure the change in the vortex radius we have placed the CCD camera (SP620U, Ophir) at the back focal plane of the Fourier lens and varied the position of the axicon. A 5 mm long and 4 $\times$ 5 mm aperture, BaB_2O_4 (BBO) is used as the nonlinear crystal for down conversion of the pump beam (Fig. 4.2.1 (b)). The crystal is cut at θ=29.9°, internal angle with the normal incidence, for type-I (e$\rightarrow$o+o) non-collinear phase-matching to produce degenerate signal and idler photons at 810 nm at an angle 3° with respect the pump beam. Due to the circular symmetry, the photons are generated in a cone of apex angle 6° and the photons of each pair are situated in diametrically opposite points. A second lens, f=50 mm Fourier transforms the generated SPDC ring which is recorded using electron multiplying CCD (EMCCD, Andor-iXon Ultra 897) after filtering the pump photon using an interference filter, IF of 10 nm bandwidth centred at 810 nm. The EMCCD has 512$\times$512 pixels with pixel size of 16 micron. To suppress background noise the EMCCD was operated at -80°C. We have taken images by accumulating 20 frames exposure time of 0.5 s. The λ/2 placed after the mirror M2 is to adjust the polarization of the input beam depending on the crystal orientation for perfect phase matching.

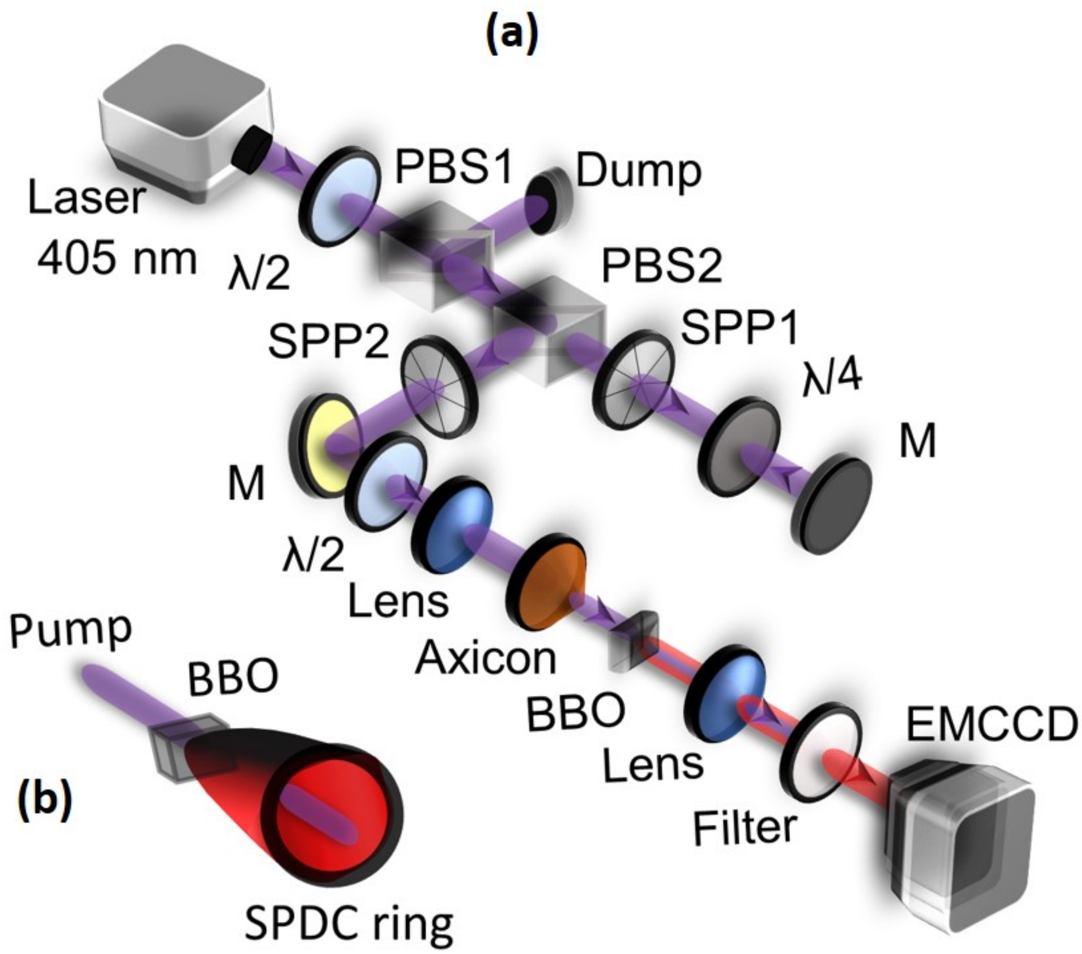

Figure 4.3.1: (a) Schematic of the experimental setup. $\lambda/2$, half wave plate; PBS1-2, polarizing beam splitter cube; SPP1-2, spiral phase plate; $\lambda/4$, quarter wave plate; M1-2, Mirrors; Axicon, to generate BG beam; BBO, nonlinear crystal for down conversion; Filter, interference filter; EMCCD, electron multiplying CCD. (b) Schematic of generation of SPDC ring.

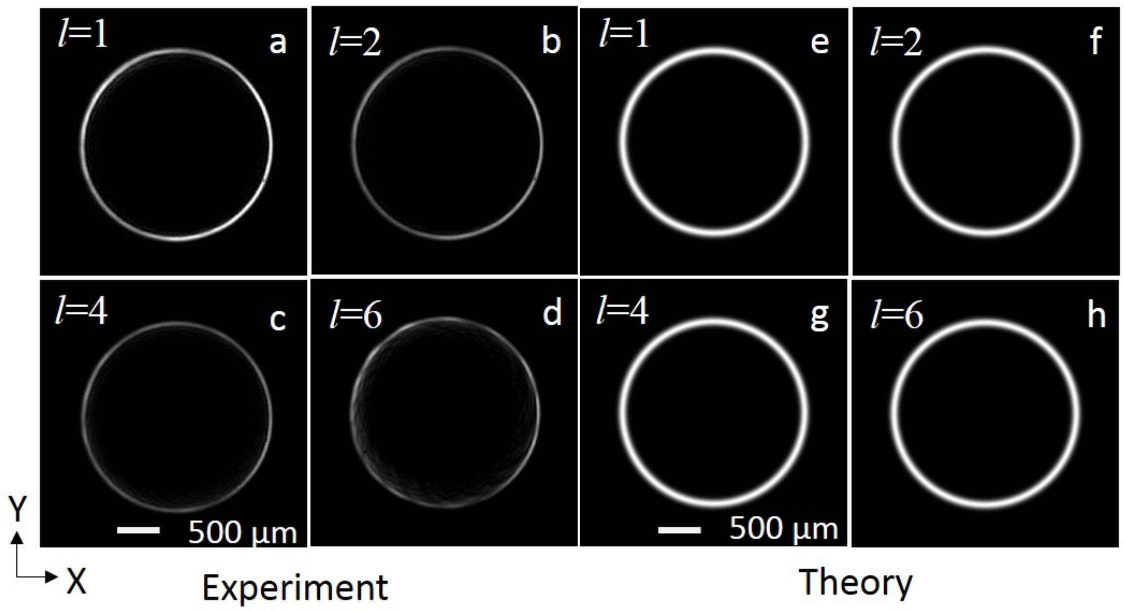

Figure 4.4.1: (a-d) Experimentally measured intensity distribution and (e-h) corresponding theoretical intensity distribution of the perfect vortex of order l=1, 2, 4 and 6.

4.4 Results and discussion

4.4.1 Generation of perfect vortex beam

To verify the generation of perfect vortex, we have recorded the intensity profile of the beam at the back focal plane of the Fourier transforming lens (f=200 mm) using a CCD camera with the results shown in Fig. 4.4.1. The axicon is placed at D=160 mm before the Fourier plane. As evident from the intensity profile of the vortex beams of topological charge l=1 , 2, 4, and 6 shown in Fig. 4.4.1 (a-d) respectively, all the beams have same annular ring radius, ρ_r=1.18 mm confirming the generation of vortices having annular ring radius independent of topological charge. Using Eqn. (3.2.3) we have simulated the perfect vortex profile, which are shown in Fig. 4.4.1 (e-h). We verified that value of ρ_r obtained form theoretical plot is closely matching with experimental value.

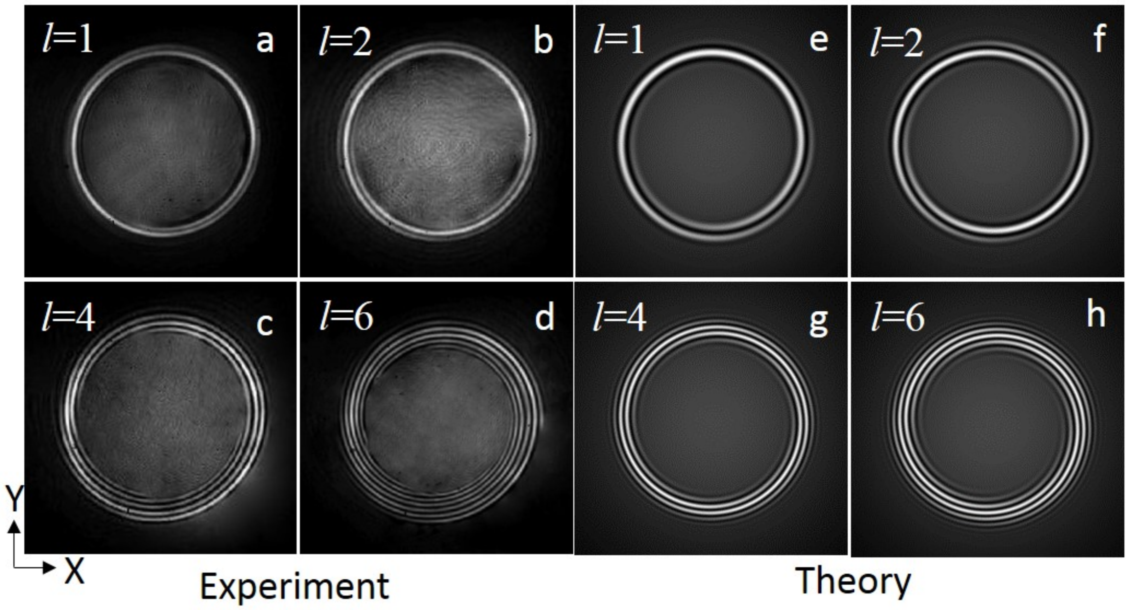

Figure 4.4.2: (a-d) Experimentally measured interference pattern and (e-h) corresponding theoretical interference pattern of the perfect vortex of order l=1, 2, 4 and 6 and Gaussian beam.

To confirm the vorticity and order of the perfect vortex, the beam is interfered with a Gaussian beam at 405 nm with interference pattern shown in Fig. 4.4.2. A close observation of the interference pattern of Fig. 4.4.2 (a-d) reveals the characteristic spiral patterns at the annular ring of the beams corresponding to vortex orders l=1, 2, 4, 6 respectively. Unlike the spiral fringe pattern as observed in the interference of normal vortex beam with Gaussian beam, the spiral fringes in Fig. 4.4.2 (a-d) is not visible at the center of the interference pattern due to the large dark core of the perfect vortices. Such observation clearly ascertains the capability of our experimental scheme in generating high-quality perfect optical vortices even at higher values of topological charges. Using Eqn. (3.2.3) along with the experimental parameters we have theoretically simulated their interference pattern with Gaussian beam with the results shown in of Fig. 4.4.2 (e-h) respectively. We can clearly see a close matching between theoretical and experimental results.

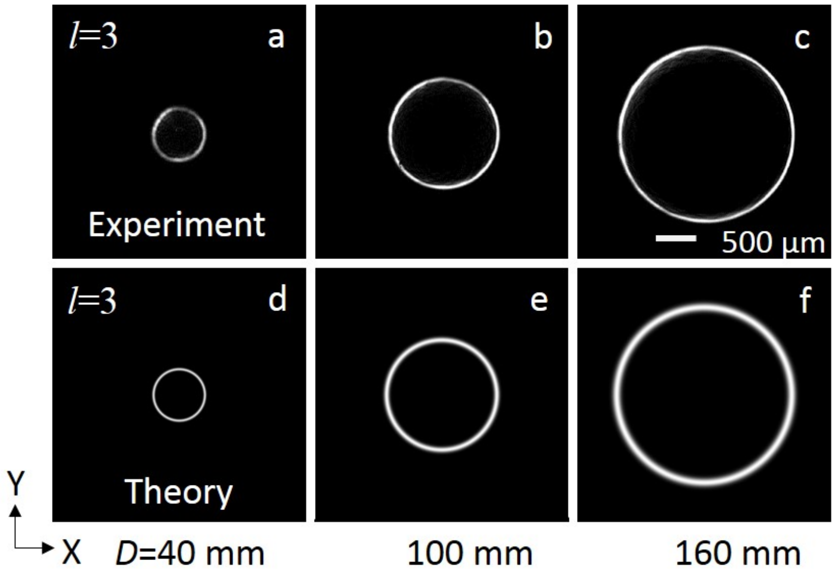

Figure 4.4.3: Experimental and theoretical images of the perfect vortex of order l=3 for different position of the axicon. First row and second row respectively represent the experimental and theoretical images of the perfect vortex for D value (a,d) 40 mm, (b,e) 100 mm, (c,f) 160 mm.

4.4.2 Variable size perfect vortex beam

With the successful generation of perfect vortices with orders as high as l=6, we experimentally confirmed the variation of perfect vortex radius on demand. As a proof of principle, we recorded the intensity pattern of the perfect vortex of topological charge l=3 at the Fourier plane for three different axicon positions, D=40, 100 and 160 mm, with the results are shown in Fig. 4.4.3. As evident from first row (a)-(c) of Fig. 4.4.3, the annular ring has radius of 0.3 mm, 0.75 mm and 1.18 mm for the D- value of 40 mm, 100 mm and 160 mm respectively. In principle the annular ring radius can further be reduced by decreasing the D-value, however, due to the mechanical constrain arising from the CCD camera structure and related optical components (attenuators) we could not record experimentally the perfect vortex of ring radius, $\rho_r < 0.3$ mm by placing the axicon with separation D <40 mm. To avoid such mechanical constrain in recording the vortex ring radius for D <40 mm, which is beyond the scope of present study, one can easily image the Fourier transforming plane to other measurement planes. On the other hand, further increase in vortex ring radius requires Fourier transforming lenses of longer focal lengths. Using Eq. (3.2.3) along with the experimental parameters, we have also theoretically calculated the intensity profile of the vortex of l=3 as shown in second row (d)-(f) of Fig. 4.4.3, in good agreement with the experimental results. However, we can observe a slight mismatch in the theoretical and experimental values of vortex ring radius which can be attributed to the inaccuracy of the apex angle used in theoretical study.

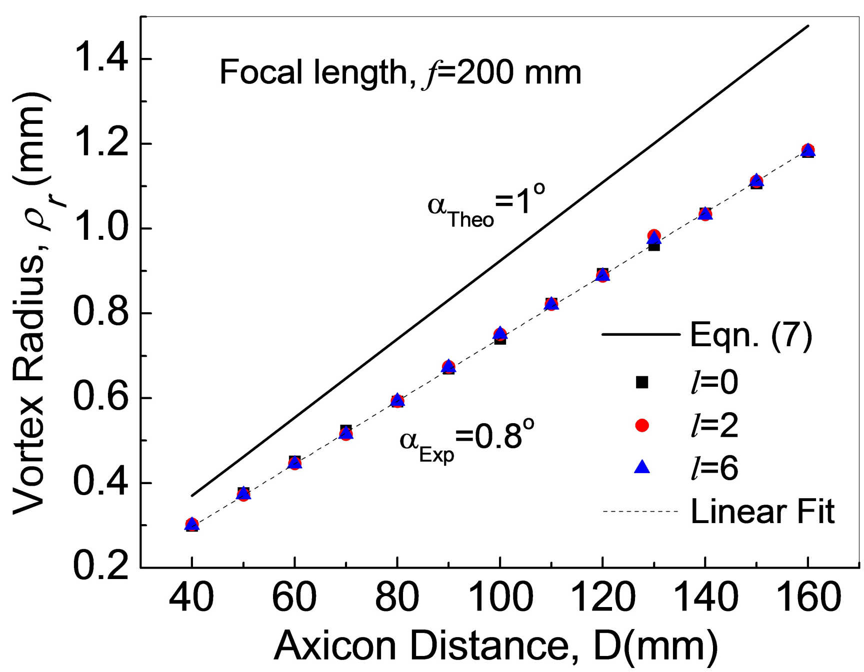

Figure 4.4.4: Variation of perfect vortex radius with distance D for vortex order 0, 2 and 6. The solid points and dotted line represent the experimental data and linear fit, respectively. Solid line represents theoretical beam radius of the perfect vortex calculated using Eq. (7) and axicon parameters.

To get more insight about the possibility of varying the ring radius of vortices of all orders, we have measured the ring radius of the vortices of three different orders l=0, 2 and

6 (l=0 is the Gaussian beam) with the results shown in Fig. 4.4.4. As evident from Fig. 4.4.4, the annular ring of the Gaussian as well the vortices of both orders have same radius for a fixed position of the axicon and increases linearly with the increase of D-value. Using Eq. (3.2.4) and axicon parameters (base angle $\alpha = 1^{\circ}$ and refractive index, n=1.5302 at 405 nm) we found a clear mismatch between theoretical (solid line) and experimental results. The theoretical and experimental variation of ring radius with axicon distance have slope of 9.23×10^{-3} and 7.33×10^{-3} respectively. From the experimentally measured slope (7.33×10^{-3}) we found the apex angle of the axicon to be 178.4° slightly higher than the value 178° presented by the manufacturer. To verify the manufacturing inaccuracy in the apex angle of the axicon, we have repeated the same experiment for three different laser wavelengths (532nm, 632 nm and 1064 nm). As expected, the annular ring radius increases with axicon position (D) away from the Fourier plane for all three wavelength at a slope of $\sim 6.83 \times 10^{-3}$, 7.05×10^{-3} and 7.05×10^{-3} for 532 nm, 632 nm and 1064 nm respectively. Using the refractive indices of the BK-7 glass we found the axicon to have apex angle of $178.4^{\circ} \pm 0.03^{\circ}$ similar to the value measured previously. Such study also proves that the present experimental scheme (Fig. 4.2.1) can be used as a quick and simple way of measuring the apex angle of an axicon. However, the measurement on the shape of the axicon tip and other axicon parameters required sophisticated equipment including optical profilometer [72]. We confirm the vorticity of the variable perfect vortex while varying the ring radius (ρ_r), the generated perfect vortex beam at different values of D=40, 100 and 160 mm are interfered with a Gaussian beam at 405 nm and the interference pattern shown in of Fig. 4.4.5 (a-c). One can clearly distigush the formation of three spiral fringe pattern corrsponding to the order l=3. The theoretically stimulated inteference pattern of the same has shown in Fig. 4.4.5 (d-f).

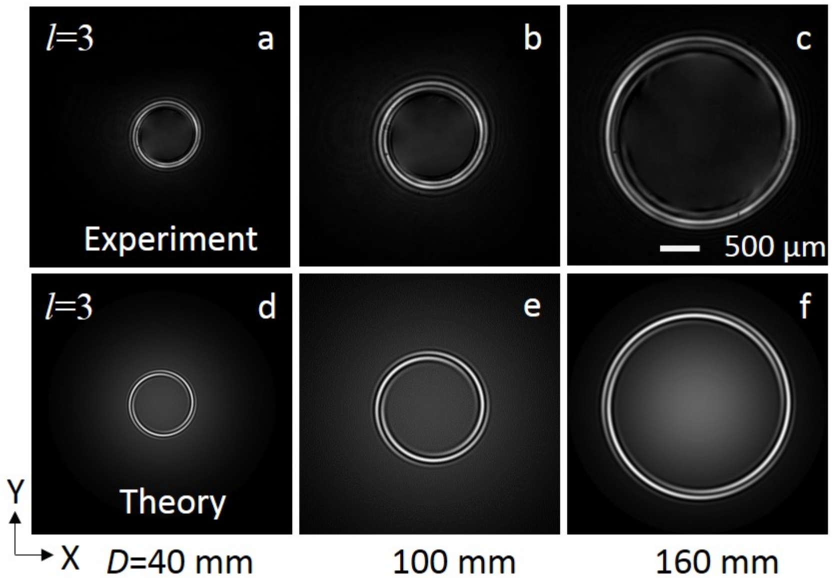

Figure 4.4.5: (a-c) Experimentally measured interference pattern and (e-f) corresponding theoretical interference pattern of the variable perfect vortex of order l=3 generated at different D=40, 100 and 160 mm with Gaussian beam.

4.4.3 Study of angular spectrum of SPDC photons using variable size perfect vortex beam

To study the contribution of OAM in the angular spectrum of the down converted photons, we pumped the nonlinear crystal (BBO) placed at the Fourier plane after the axicon using perfect vortices of different orders and ring radii. The angular spectrum or transverse momentum distribution of the down converted photons, obtained from the Fourier transformation of the generated photons using a convex lens of focal length, f=50 mm in $f-f$ optical system configuration, is recorded using EMCCD. Each pixel represents a particular transverse position r of the down converted photons, which corresponds to a transverse momentum value, K= $[\omega_{dc}/(cf)]r$, where, ω_{dc} is the frequency of the down converted photons, c is the velocity of light in free space and f is the focal length of the Fourier transforming lens. In the current study we have used topological charges, l=3 and

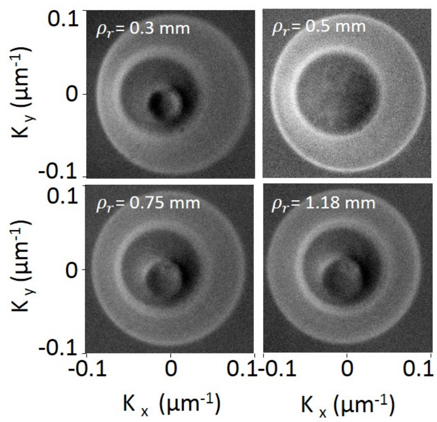

(a)

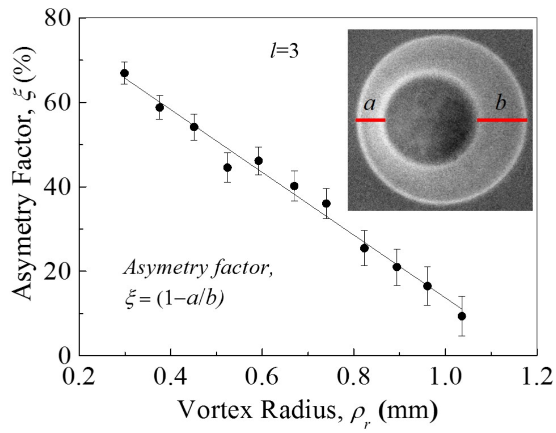

(b)

Figure 4.4.6: (a) Angular spectrum (transverse momentum) of the down converted photons recorded using EMCCD with vortex order l=3 for pump beam radius of, 0.3, 0.5, 0.75, and 1.18 mm. K_x and K_y are the transverse momentum components. (b) Dependence of asymmetry of the angular spectrum of the down converted photons on the radius of pump vortex beam. Asymmetry parameter is defined as ξ = (1-a/b), where, 'a' and 'b' are quantified as the separation between two rings on left and right side of the transverse momentum distribution of the down converted photons (inset).

varied their ring radius ρ_r for different axicon positions (D-value) and recorded the angular spectrum of the down converted photons with the results shown in Fig. 4.4.6. Fig. 4.4.6 (a) represents the angular spectrum of the down converted photons corresponding to pump radius, ρ_r= 0.3, 0.5, 0.75 and 1.18 mm for l=3. K_x and K_y are the transverse momentum components of the down converted photons. As evident from the Fig. 4.4.6 (a), for a given topological charge, l and for different annular ring radius ρ_r the down converted photons have different transverse profiles with intense inner and outer rings and intensity gradient in between. The dark spot at the centre of each transverse momentum distribution can be attributed to the back ground correction used to avoid the pump beam leaked through the interference filter. Although the increase in pump beam radius does not modify the size of the transverse momentum profile of the down converted photons, at lower pump beam size the down converted photons have asymmetric transverse momentum distribution. Such asymmetry arising from the Poynting vector walk-off in the birefringent crystals are observed for tightly focused beams of radius smaller or equivalent to the lateral displacement of the beam, $L \times tan(\rho_o)$ in the nonlinear crystal of length, L and birefringence parameter,ρ_o. For L=5 mm and ρ_o=67.44 mrad of the BBO crystal, the $L \times tan(\rho_o)$ value is calculated to be 0.34 mm. As a result we can expect asymmetric transverse distribution in down converted photons for pump beam radius, ρ_r=0.3 mm.

The asymmetry in the transverse momentum distribution of the down converted photons is detrimental for entangled photon sources [73], and for all practical purposes, one need symmetric distribution. Therefore, we have studied the asymmetry in transverse momentum distribution of the down converted photons quantitatively with the radius of the perfect vortex beam. The results are shown in Fig. 4.4.6 (b). The asymmetry factor, ξ is defined as $\xi = 1 - a/b$, where a and b representing the separation between the inner and out radii on left and right sides of the angular spectrum of the down converted photons respectively as shown in inset of the Fig. 4.4.6 (b). We have calculated the asymmetry factor, ξ, for different size of the perfect vortex of order l=3. As evident from the Fig. 4.4.6 (b), the ξ value decreases linearly with the increase of perfect vortex ring radius. Although it is expected to have symmetric angular spectrum of the down converted photons for the input vortex ring radius $\rho_r > L \times tan(\rho_o)$(>0.34 mm), we still observe a certain degree of asymmetry in angular spectrum at higher values of ρ_r. However, for ρ_r =1.18 mm ($\sim 3 \times L \times tan(\rho_o)$) we have observed symmetric (ξ <10%) angular spectrum of the down converted photons. Such study ascertain the need of proper beam diameter of the input structured beam (here, perfect vortex beam) depending upon the birefringence and length of the nonlinear crystal for entangled photon sources.

To understand how the OAM of the pump is effecting the angular spectrum of the down converted photons, we have pumped the crystal with different topological charge l= 0, 1, 3, 5 keeping the ring radius at ρ_r =1.18 mm. The results are shown in Fig. 4.4.7. As it

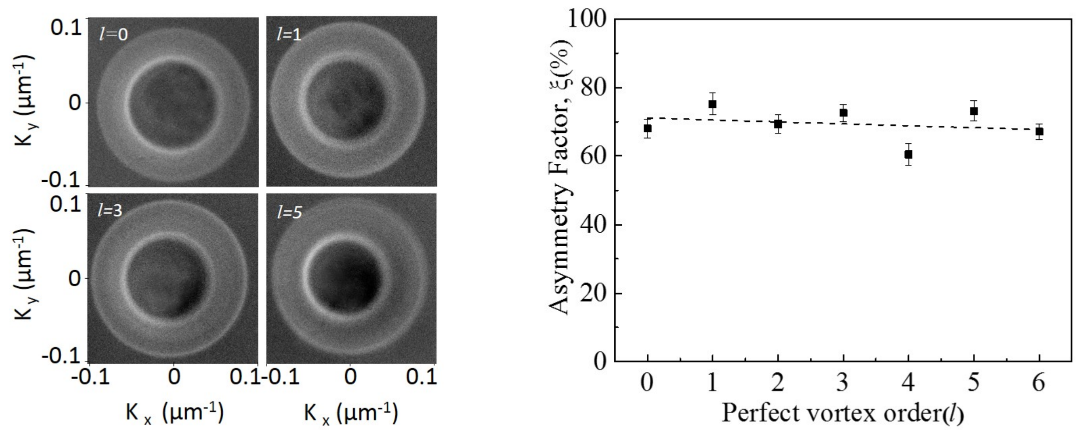

(a) (b)

Figure 4.4.7: (a) Angular spectrum (transverse momentum) of the down converted photons recorded using EMCCD with perfect vortex radius ρ_r =1.18 mm for topological charge l = 0,1,3, and 5. K_x and K_y are the transverse momentum components. (b) Dependence of asymmetry of the angular spectrum of the down converted photons on OAM of the pump vortex beam.

clear from the Fig. 4.4.7 (a) that with increase of topological charge l, asymmetry in the angular spectrum is unchanged. To understand further we have plotted asymmetry factor, ξ with different topological charge, l, which is shown in Fig. 4.4.7 (b). Starting from l=0 to 6, the asymmetric factor, ξ, falls within the linear fitting having slope $\sim$-0.5% for most of the l values. Since the value of slope is well within the error bar, one can assume there is no change in asymmetry with the increase of topological charge. Therefore, it can be concluded that the OAM of the input pump beam has no effect in the transverse distribution of the down converted photons.

4.5 Conclusion

In conclusion, we have demonstrated a novel experimental scheme to generate perfect vortex of any ring radius using a convex lens and an axicon. Using a lens of focal length

f=200mm, we have varied the radius of the vortex beam across 0.3-1.18 mm simply by adjusting the separation between the lens and axicon (D). This is also a simple scheme to measure the apex angle of an axicon with ease. Using such vortices we have studied non-collinear interaction of photons having orbital angular momentum (OAM) in spontaneous parametric down-conversion (SPDC) process and observed that the angular spectrum of the SPDC photons are independent of OAM of the pump photons rather depends on spatial profile of the pump beam. In the presence of spatial walk-off effect in nonlinear crystals, the SPDC photons have asymmetric angular spectrum with reducing asymmetry at increasing vortex radius.

Chapter 5

Controlling the spatial distribution of bi-photon mode

This chapter constitutes the following journal publication:

1. *Control of spatial distribution of entangled photons by the spatial structure of classical pump beam*
   M. V. Jabir, Apurv Chaitanya N., and G. K. Samanta,
   Frontiers in Optics 2015, OSA Technical Digest (online) (Optical Society of America, 2016), paper JTh2A.18

5.1 Introduction

Spontaneous parametric down-conversion (SPDC), one of the most important nonlinear processes, is of paramount interest especially in the field of quantum optics due to its intrinsic capability in generating entangled photon pairs. Entanglement properties of the paired photons generated through SPDC process are highly influenced by different crystal parameters including birefringence and length, and the spatial structure of the pump beam [60, 53]. Therefore, engineering the spatial structure of the pump beam to the SPDC process,one can in principle, modify the spatial distribution of heralded single photons. Recent studies have shown the transfer of pump properties such as non-diffraction [74], and doughnut intensity distribution [17] into the transverse amplitude of heralded single photon. However, to study the hybrid entanglement in OAM and polarization degree of freedom [75, 12], it is important to understand the effect of spatial structure of the pump beam on polarization entanglement property of heralded single photons. Here we report, first time to best of our knowledge, direct transfer of the spatial distribution of the classical beam to the spatial distribution of the entangled photons. Pumping the dual nonlinear crystal with optical vortex beam, we show that the entangled photons have doughnut spatial distribution similar to the pump. Therefore, one can manipulate the spatial distribution of entangled photons by simply manipulating the pump spatial structure.

5.2 Experimental methods

The schematic of the experimental setup is shown in Fig. 5.2.1. A continuous-wave, single-frequency (<12 MHz) UV laser providing 100 mW of output power at 405 nm has been used as pump laser. The laser power to the experiment is controlled using a half-wave plate ($\lambda/2$) and a polarizing beam splitter (PBS) cube. Two spiral phase plates, SPP1 and SPP2 are used to convert Gaussian beam into optical vortices of order, l=1 and l=2, respectively. Using a vortex-doubler setup comprising a PBS, quarter-wave plate ($\lambda/4$) and plane mirror, M, we have generated optical vortices of order, l=6. The $\lambda/2$ placed before the crystal controls the polarization of the pump beam to the crystal. Two cascaded 0.6 mm thick BiBO crystals in 10$\times$10 mm^2 aperture with optic axis orthogonal to each other glued together is used as SPDC crystal. The crystals are cut with, θ=151.7° (φ=90°) in optical yz-plane for perfect phase-matching of non-collinear (half-opening angle $\sim$3°) type-I (o$\rightarrow$e+e) degenerate down-conversion of 405 nm laser at normal incidence. Due to orthogonal optical axis, these two crystals produce SPDC photons in orthogonal polarization states, $|HH\rangle$ and

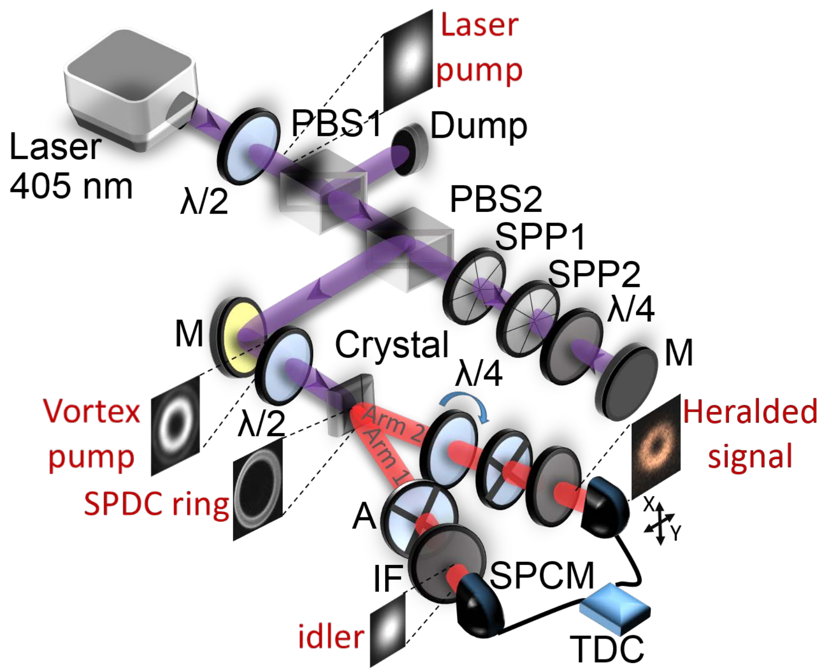

Figure 5.2.1: Schematic of the experimental setup. $\lambda/2$, half-wave plate; PBS1-2, polarizing beam splitter cube; SPP1-2, spiral phase plates; $\lambda/4$, quarter-wave plate; M1-2, Mirrors; Crystal, dual-BiBO for generation of entangled photons; IF, interference filter; SPCM, single photon counting module; TDC, time to digital converter; 2D images show the spatial profile at the respective point.

$|VV\rangle$ and the entangled photon state given as, $|\Psi\rangle = sin(\gamma)\,|HH\rangle + cos(\gamma)e^{(-i\phi)}\,|HH\rangle$. γ is angle of the $\lambda/2$ plate placed before the crystal and phase ϕ can be controlled using $\lambda/4$ plate kept in one of the arm of the down conversion photons. The polarization correlation were studied using the analyzer setup comprised with a $\lambda/2$ plate and PBS for 810 nm, single photon counting module and time to digital converter (TDC). Interference filter (IF) with transmission bandwidth of $\sim$10 nm with central wavelength at 810 nm extracts degenerate photons from broad spectrum of SPDC process. A time window of 8.1 ns was used to measure the coincidence with estimated accidental coincidence $\sim$3/sec.

5.3 Results and discussion

5.3.1 Study of polarisation entanglement with Gaussian beam

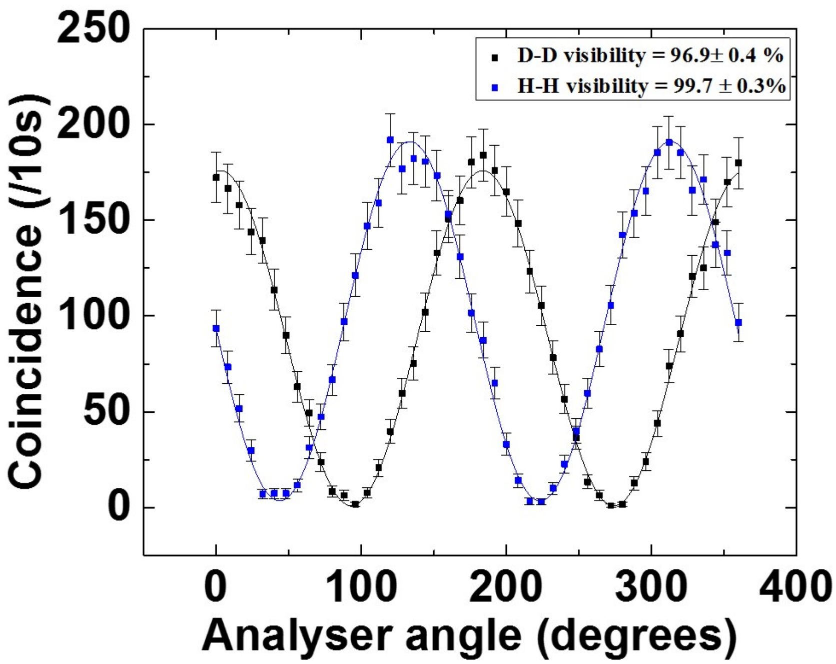

Figure 5.3.1: Variation in coincidence counts when the analyzer at the idler arm rotate while the analyzer at signal arm kept @ 45° (black dots) for D-D projection and @ 0° (blue dots) for H-H projection while pumped with Gaussian beam.

To study the photons entangled in polarization degree of freedom generated via SPDC process, we initially pump the dual-crystal with Gaussian beam. Since the cascaded dual-crystal whose optical axis are aligned in orthoganl direction, each crystal will produce bi-photon state in $|VV\rangle$ and $|HH\rangle$ respectively for a diagonaly ($|D\rangle$) polarised pump beam. As the coherence length of the pump beam is much higher than the crystal thickness the

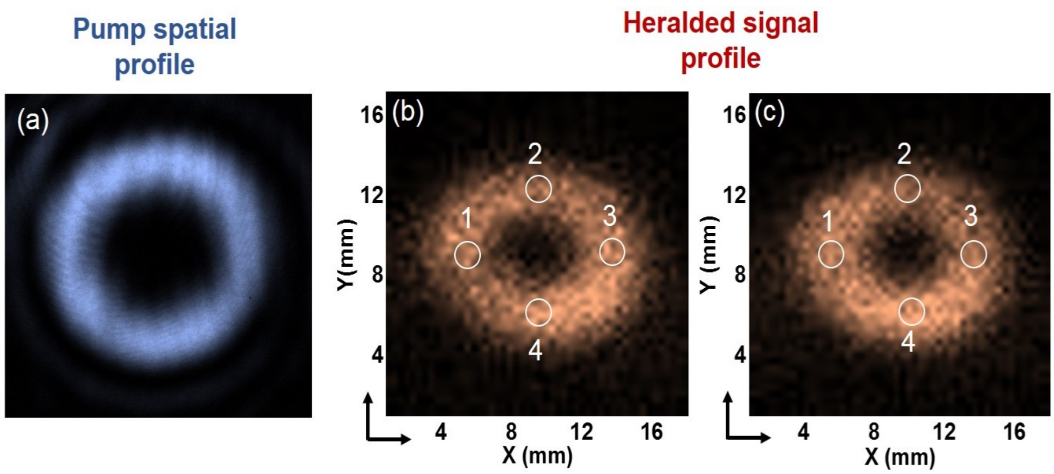

Figure 5.3.2: (a) Intensity profile of the pump vortex beam. (b) Horizontal and (c) Vertical polarized heralded signal photons generated from each crystals independently.

generated state can be written as superpostion of individaul state, $1/\sqrt{2}(|VV\rangle \pm |HH\rangle)$. Using standard polarization correlation measurement technique [76] we measured the coincidence visibility at D-D projection (black dots) and H-H projection (blue dots) shown in Fig. 5.3.1. The measured visibility at D-D and H-H projection are 96.9±0.4% and 99.7±0.3% respectively. The measured visibilities under both basis are large enough to violate Bell's inequality. Therefore, the meaured Bell's parameter to be S= 2.73±0.04 indicating the high quality polarization entanglement of the generated two-photon state.

5.3.2 Transfer of vortex spatial distribution in SPDC process

To understand the effect of spatial structure of the pump beam we have generated optical vortex beam. Due to limited availability of SPPs producing vortices of order l >2, we have used a vortex-doubler setup [71] comprised of a polarizing beam splitter cube (PBS 2), quarter-wave plate ($\lambda/4$), and dielectric coated mirror, M1, with high reflectivity at 405nm. With the help of vortex doubler we have generated optical vortices of orders (topological charges) up to l=6. The intenisty profile of the pump vortex order l=6 is shown in Fig. 5.3.2(a). The optical vortex beam resembles dougnut shape as the center of the beam has no intensity. It is clear from the previous study [17] that the intesity profile or the beam shape will be transferred to the heralded single photon genertaed in the SPDC process. To verify the successful transfer of the transverse amplitude of the pump beam through heralding in non-collinear SPDC process, where high energy photon owing to energy conservation splits into two low energy photons known as signal and idler are distributed in a ring with signal and idler photons laying in diametrically opposite points, we pumped the crystal with a vortex beam of order l=6 and measured the spatial profile of the signal (let's say) while conditioning the detection of its partner photon, idler. Using two multimode fibers, one detecting the idler photons with maximum photon counts, we have scanned the other fiber to detect corresponding signal photon at diametrically opposite point of the SPDC ring. Figure 5.3.2 (b) and (c) show the scanned profile of the heralded signal photons in $|VV\rangle$ and $|HH\rangle$ state generated from each crystal. The doughnut spatial distribution of the heralded single photons similar to the pump vortex clearly confirm the transfer of spatial profile of the classical pump beam to the single photons. The intensity asymmetry in the conditional profiles can be attributed to the birefringence of the crystals [60]. From the coordinates of the Fig. 5.3.2 (b) and (c), it is also evident that the heralded signal photons generated in individual crystals have exact spatial overlapping, indicating the possibility of resdistribution of the polarised entangled photons over the spatial coordinate.

5.3.3 Study of polarization entanglement with vortex beam

We have studied polarization entanglement across the spatial distribution of the heralded single photons. We chose four points, 1 to 4 as shown in Fig. 5.3.2(b) and (c) and measured correlation measurements and Bells' parameter to verify the entanglement. With proper adjustment of ϕ and γ, we projected the generated state into one of the Bell's states given as $|\psi\rangle = 1/\sqrt{2}(|HH\rangle + |HH\rangle)$. We measured the coincidence visibility at D-D projection (black dots) and H-H projection (blue dots) for point 1-4 with the results shown in Fig. 5.3.3 (1-4). As evident from Fig. 5.3.3, the point 1 and point 2 have visibility of 92.2±0.2%

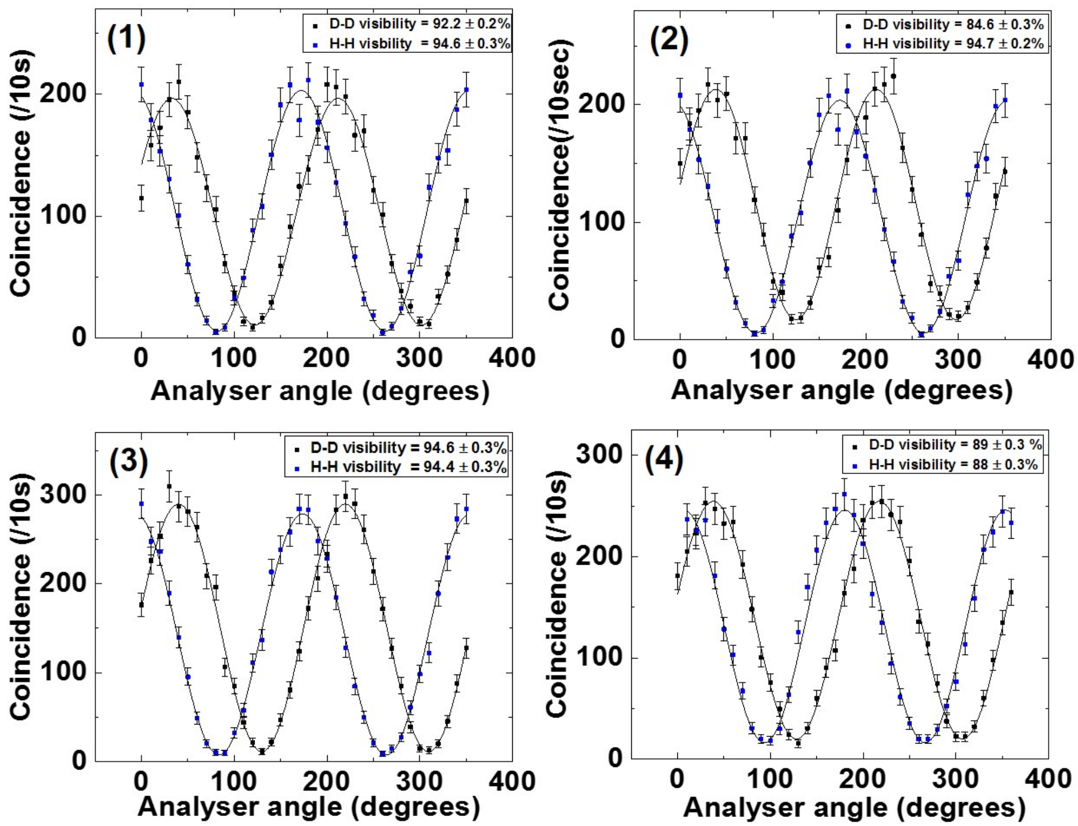

Figure 5.3.3: Variation in coincidence counts when the analyzer at the arm 2 rotate and the analyzer at arm 1 kept at 45° (black dots) for D-D projection and at 0° (blue dots) for H-H projection at point (1)-(4) while pumped with vortex beam.

(94.6±0.3%) and 84.6±0.3% (94.7±0.3%) in diagonal, D-D (horizontal,H-H) projection respectively and the point 3 and 4 have visibility of 94.6±0.3% (94.4±0.3%) and 89±0.3% (88±0.3%) in diagonal, D-D (horizontal,H-H) projection respectively. All the measured visibilities under both basis are higher than 71% [77], large enough to violate Bell's inequality. The measured Bells parameter, S~2.482±0.003 and 2.401$\pm$0.004 for point 1 and 2 respectively and 2.476±0.002 and 2.421$\pm$0.003 for point 2 and 4 respectively, much beyond its classical limit 2. Such high visibilities and Bells violation indicate the presence of high quality entanglement across the spatial extend of the heralded photons even after pumping with vortex beam. Further improvement in the degree of entanglement can be realized using proper compensation scheme [56].

5.4 Conclusion

In conclusion, we experimentally demonstrated, that the spatial profile of classical beam can be directly transferred to the polarized entangled photons. Correlation measurement and the Bells parameter indicate the presence of polarization entanglement even after pumping with the vortex beam. Therefore, one can manipulate spatial distribution of polarized entangled photons by simply manipulating the pump spatial structure. The results can pave the path to generation of hybrid entangled state with the structured pump beam.

Chapter 6

Generation of two photon hybrid entangled state

This chapter constitutes the following journal publication:

1. *Direct transfer of classical non-separable states into hybrid entangled two photon states,*
   M. V. Jabir, Apurv Chaitanya N., Manoj Mathew, G. K. Samanta,
   Scientific Reports 7, 7331 (2017)

6.1 Introduction

Entanglement, the quintessential strong non-classical correlations in joint measurement of at least two separate quantum systems, plays a critical role in many important applications in quantum information processing, including quantum communication[28], quantum computation [78], quantum cryptography [79], dense coding and teleportation [80]. Typically, in photonic quantum optics, spontaneous parametric down-conversion (SPDC) is used to produce correlated photon pairs [13, 14, 81, 82] with many accessible degree-of-freedom

(DoF) that can be exploited for the production of entanglement. With the first demonstration of entanglement with polarization DoF [83, 76], recent advancement in quantum optics have provided intrinsic entanglement (entanglement in variety of DoFs such as orbital angular momentum (OAM) air[4], energy time [35], time bin [84], and many more [85]), hyperentanglement [6] (entanglement in every DoFs) and hybrid entanglement (entanglement between different DoFs of a pair of particles). While these entangled states have various applications, the hybrid entangled states encoded with polarization and OAM, in particular, allow the generation of qubit-qudit entangled states [86] for quantum information, macroscopic entanglement with very high quanta of OAM [87], important for quantum information science, and super sensitive measurement of angular displacement in remote sensing [88].

Typically, hybrid entangled states encoded with polarization and OAM are generated through the imprinting of chosen amount of OAM to a high-fidelity polarization entangled state using mode converters, such as, spatial light modulator (SLM) [75] and q-plate [89], in complicated experimental schemes. As compared to all mode converters, the SLM have many advantages in terms of dynamic variation in OAM, accessibility to very high OAM and flexibility in imprinting two particles with an arbitrarily high difference in OAM [87]. However, the diffraction based OAM imprinting process of the SLM reduces the overall number of photons and thus limiting the use of hybrid states for practical applications requiring entangled state with high brightness. In addition to the photon losses, the alignment of SLM at significantly low number of photons generated in SPDC process is very much complicated than using the same device for the pump beam. To circumvent such problem, as such, it is imperative to device alternative techniques to produce hybrid entangled states in simple experimental scheme. Entanglement properties of the paired photons generated through SPDC process are highly influenced by different crystal parameters including birefringence and length, and the spatial structure of the pump beam [60, 53]. Recent studies have shown that the transfer of pump properties such as non-diffraction [74], intensity distribution and phase structure [17, 90] into the transverse amplitude of heralded single photons. Therefore, one can in principle manipulate the pump beam to directly generate hybrid entangled states through SPDC process.

On the other hand, light beams with non-separable states in polarization and OAM [91, 92] have attracted a great deal of interest due to its violation of Bell like inequality [93, 94]. Here we propose, for the first time to the best of our knowledge, direct transfer of non-separable laser beams into hybrid entangled two photon states in a simple experimental scheme. As a proof of principle, pumping the contiguous nonlinear crystals with classical non-separable pump beam of OAM mode l=1 and 3, and characterizing the quantum states through violation of Bell's inequalities and the measurement of entanglement witness operator ($\widehat{W}$) for twin photons, we showed that the generated two photons are entangled in both polarization and OAM. The concept is generic and can be used for hybrid entanglement with higher OAM, and photons with arbitrarily high difference in OAM through proper choice of non-separable states of the pump beam. The concern of rapidly decreasing efficiency of the down conversion process for the direct generation of entanglement of higher OAM, can be overcome by OAM independent beam size of the non-separable states using the scheme used in previous reports [53, 95].

6.2 Theory

The following conceptual theory explains the generation of two-photon hybrid entangled state through parametric down conversion process in dual-crystal scheme. Two photon state generated from spontaneous parametric down conversion can be written in the basis OAM bases as [96]

$$\Psi = \sum_{l_i=-\infty}^{\infty} C_{l_i l_s} \left| l_i, l_p - l_i \right\rangle . \qquad (6.2.1)$$

where $l_p$is the pump OAM order, l_i and l_s(l_p-$l_i = l_s$) is the OAM order of the idler and signal. C_l is the eigenvalue corresponding to the state $\left|l_i, l_p - l_i\right\rangle$, with normalization condition $\sum_{l_i=-\infty}^{\infty} |C_{l_i l_s}|^2$=1. Similarly the wave function can be written in the basis of the polarization eigenstate generated under type-1 phase matching crystal (say in crystal-1),

$$\Psi = |H_i, H_s\rangle \,. \tag{6.2.2}$$

Then the total wave function in both polarization and OAM eigenstate generated in crystal-1 will be written as,

$$\Psi_1 = \sum_{l_i=-\infty}^{\infty} C_{l_i l_s} |H_i, l_i\rangle \left|H_s, l_p - l_i\right\rangle . \tag{6.2.3}$$

The state generated from another crystal (crystal-2) whose optical axis is aligned orthogonal to the crystal-1 will be,

$$\Psi_2 = \sum_{l_i=-\infty}^{\infty} \sum_{l_s=-\infty}^{\infty} C_{l_i l_s} |V_i, l_i\rangle \left|V_s, l_p - l_i\right\rangle . \tag{6.2.4}$$

When both of the crystals are simultaneously pumped with the pump sate, $\Psi_{pump} = \frac{1}{\sqrt{2}}\left(\left|H, l_p\right\rangle + \left|V, -l_p\right\rangle\right)$, the crystal-1 will be phase matched for H-polarization carrying OAM, l_p and crystal-2 will be phase matched with V-polarization carrying OAM $-l_p$. As both the states are generated within the coherence length of the laser and with equal pump power is used for both crystal, one can write the total wave function as superposition of Ψ_1 and Ψ_2 with equal weight,

$$\Psi_{total} = \frac{1}{\sqrt{2}}\left(\sum_{l_i=-\infty}^{\infty} C_{l_i l_s} |H_i, l_i\rangle_1 \left|H_s, l_p - l_i\right\rangle_1 + \exp(i\phi) \sum_{l_i=-\infty}^{\infty} C_{l_i l_s} |V_i, l_i\rangle_2 \left|V_s, -l_p - l_i\right\rangle_2\right), \tag{6.2.5}$$

where ϕ is the phase between the two states generated from the crystal-1 and crystal-2. The subscript 1 and 2 represent the states are generated from crystal-1 and 2. Once the generated idler form both the crystals are projected in Gaussian, l_i=0, then,

$$\Psi_{total} = \frac{1}{\sqrt{2}} \left(|H_i\rangle_1 \left|H_s, l_p\right\rangle_1 + |V_i\rangle_2 \left|V_s, -l_p\right\rangle_2 \right). \quad (6.2.6)$$

Project both the signal in diagonal polarization ,$|D_s\rangle = \frac{1}{\sqrt{2}} (|H_s\rangle + |V_s\rangle)$, then

$$\Psi_{total} = \frac{1}{\sqrt{2}} \left(\left|H_i, l_p\right\rangle_1 + \left|V_i, -l_p\right\rangle_2 \right) \quad (6.2.7)$$

Therefore, the final state will be hybrid entangled bi-photon state with, $l_p = l_s$, is,

$$\Psi_{hybrid} = \frac{1}{\sqrt{2}} (|H_i, l_s\rangle_1 + |V_i, -l_s\rangle_2) \quad (6.2.8)$$

6.3 Experimental methods

The schematic of the experimental setup is shown in Fig. 6.3.1 (a). A continuous-wave, single-frequency (<12 MHz) UV laser providing 70 mW of output power at 405 nm in Gaussian spatial profile is used as a pump laser. The laser power to the experiment is controlled using a half-wave plate (λ/2) and a polarizing beam splitter (PBS1) cube. A second λ/2 plate placed after PBS1 converts the linearly polarized Gaussian beam represented by the state, $|H0\rangle$ (here, the first and second terms of the ket represent polarization and OAM of the beam respectively) in to $\Psi_{Classical_1} = \frac{1}{\sqrt{2}}(|H0\rangle + |V0\rangle)$. Here, H and V represents horizontal and vertical polarization respectively and the Gaussian beam has OAM mode of, l =0. To prepare classical non-separable states, the pump beam is passed through a polarization Sagnac interferometer comprising with PBS2, three mirrors (M) and a polarization independent spiral phase plate, SPP. The PBS2 splits the pump state, $\Psi_{Classical_1}$ in two counter propagating beams in the Sagnac interferometer with $|H0\rangle$ and $|V0\rangle$ beams

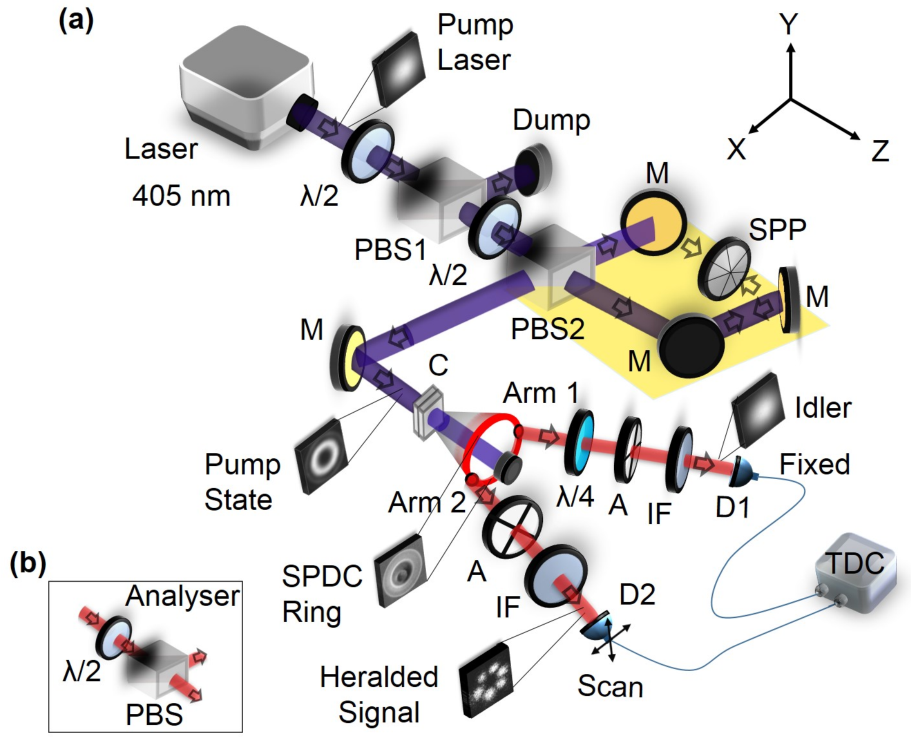

Figure 6.3.1: (a) Schematic of the experimental setup. Laser at 405 nm, continuous wave single frequency diode laser at 405 nm providing 70 mW of output power; $\lambda/2$, half-wave plate; PBS1-2, polarizing beam splitter cube; SPP, spiral phase plates; M, mirrors; schematic marked in yellow represents polarization Signac interferometer; C, dual-BIBO crystal having optic axis orthogonal to each other for the generation of entangled photons; A, analyser; $\lambda/4$, quarter wave plate; IF, interference filter; D1-2, single photon counting module (SPCM); TDC, time-to-digital converter. (b) Analyser comprises with PBS and $\lambda/2$.

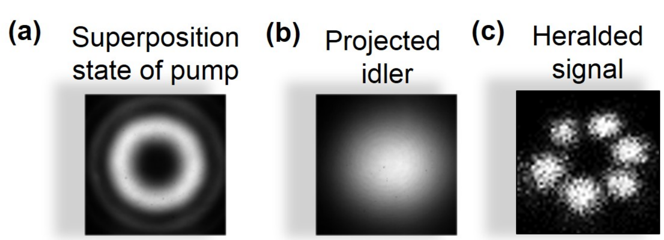

Figure 6.3.2: Spatial distribution of the non-separable states of (a) pump beam, (b) conditioned idler and (c) heralded signal photons.

propagating in counter clock-wise (CCW) and clock-wise (CW) directions respectively. After a round trip both the beams recombine in the PBS2 and produce output state same as that of the input state, $\Psi_{Classical_1}$. However, due to the presence of SPP that converts Gaussian beam (l =0) into optical vortex of OAM mode, $\pm l$, the output state of the Sagnac interferometer will be different than that of the input state. Depending on the direction of thickness variation of the SPP, if the CCW beam, $|H0\rangle$, while passing through the SPP in the Sagnac interferometer acquires spiral phase corresponding to an optical vortex of order $+l$ (say) then the CW beam, $|V0\rangle$, will acquire optical vortex of order $-l$ and vice versa. As a result, the output of the Sagnac interferometer can be represented by the classical non-separable states, $\Psi_{Classical_2} = \frac{1}{\sqrt{2}}(|Hl\rangle + e^{-i\phi}|V-l\rangle)$. The phase factor, ϕ, arises due to the asymmetric positioning of the SPP inside the Sagnac interferometer.

Two contiguous BIBO (bismuth borate) crystals each of 0.6-mm thick and 10×10 mm^2 in aperture with optic axes aligned in perpendicular planes, is used as nonlinear crystal for SPDC process. Both the crystals are cut with, $\theta = 151.7°$ ($\phi = 90°$) in optical yz-plane for perfect phase-matching of non-collinear type-I (o$\rightarrow$e+e) degenerate down converted photons at 810 nm in a cone of half-opening angle $\sim$3° for normal incidence of pump. Orthogonal positioning of the optic axes of the BIBO crystals facilitate the pump photons in both $|H\rangle$and $|V\rangle$ polarization states to produce respective non-collinear SPDC photons in concentric cones around the direction of the pump beam. For entanglement studies, we select two diametrically opposite points of the SPDC ring [red circle in Fig. 6.3.1 (a)] in the horizontal plane and named them as Arm-1 and Arm-2. In Arm-1, we conditioned one of the down-converted photons (say idler photon) using a hard aperture of diameter $\sim$460 μm and multimode fiber [17]. To herald its partner photon (here signal) we collected the photons in Arm-2 using a collimator with an opening diameter of $\sim$460 μm and a multi-mode fiber assembly placed on x-y scanning stage. The photons of each arm are analysed through coincidence count using a combination of single photon counting module (SPCM) and a time-to-digital converter (TDC). A time window of 2.5 ns was used to measure the

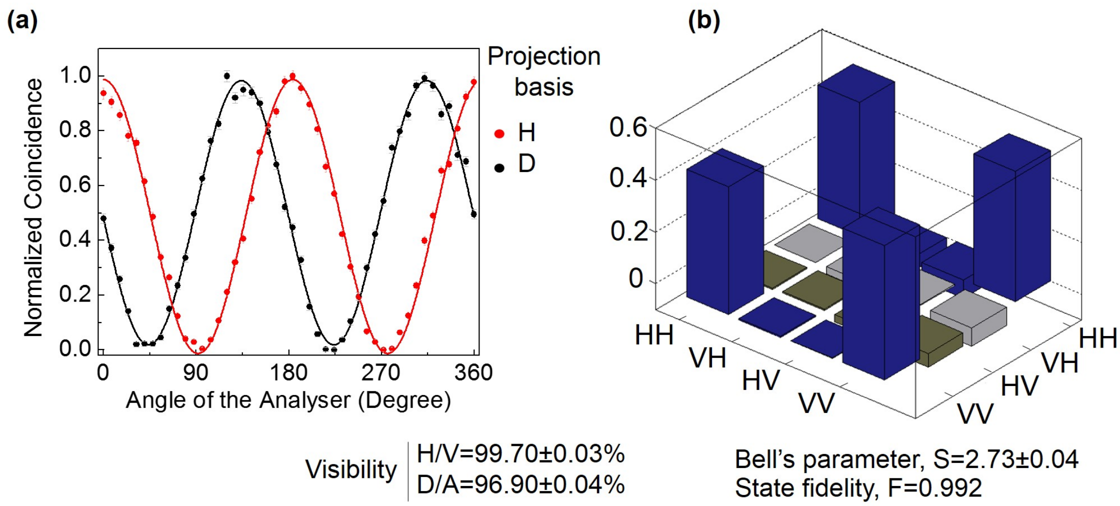

Figure 6.4.1: (a) Visibility graph for polarization entangled state at H (red dots) and D (black dots) bases. (b) Graphical representation of the density matrix obtained from linear tomographic technique for polarization entangled state.

coincidence counts. Quarter-wave plate, $\lambda/4$, and analysers, A, [comprised with a $\lambda/2$ plate and PBS as shown in Fig. 6.3.1 (b)] are used to analyse the photons in polarization basis. The interference filter (IF) with transmission bandwidth of $\sim$10 nm with central wavelength at 810 nm is used to extracts degenerate photons from broad spectrum of SPDC process. Figure 6.3.2 (a)-(c) show the spatial distribution of the non-separable states of pump beam, conditioned idler and heralded signal photons respectively.

6.4 Results and discussion

6.4.1 Generation of polarized entangled photons

In non-collinear SPDC process, where high energy photon owing to energy conservation splits into two low energy photons known as signal and idler, the generated entangled photons are distributed in a ring with signal and idler photons laying in diametrically opposite points [see Fig. 6.3.1 (a)]. To study the entanglement quality of the down converted photons in the current experimental scheme we pumped the dual-BIBO crystal with input state $\Psi_{Classical_1} = \frac{1}{\sqrt{2}}(|H0\rangle + |V0\rangle)$ in Gaussian spatial intensity distribution by removing the SPP from the Sagnac interferometer. Due to orthogonal positioning of the optic axes of the crystals, if the first crystal produces down converted photons of the pump photons of $|H\rangle$ polarization state into $|VV\rangle$ owing to type-I phase-matching, the second crystal converts pump photons of $|V\rangle$ polarization state into down converted photons in $|HH\rangle$ state and vice versa. Since the crystal thickness is small and the coherence length of the pump laser is very high (~25 m) the photons generated from the both crystals are highly indistinguishable in space and time. Therefore, one can write the output state, of the down converted photons as superposition of individual states $|HH\rangle$ and $|VV\rangle$. However, one need to determine the state and the quality of polarization entanglement in two photon states. In doing so, we used standard coincidence measurement technique and recorded the two-photon interference in terms of photon coincidence between the twin photons distributed in Arm-1 and Arm-2 under two non-orthogonal projection bases, H/V (horizontal/vertical) and D/A (diagonal/anti-diagonal) using two polarization analysers as the quantum state analyser with the results shown in Fig. 6.4.1 (a). The normalized coincidence rate measured for 10 sec show the expected sinusoidal variation with angle of the quantum state analyser with fringe visibilities 99.7±0.03% and 96.9±0.04% for H (red dots) and D (black dots) bases respectively. The measured visibilities under both basis are higher than 71% [77], large enough to violate Bell's inequality. However, using the coincidence rates we measured the Bell's parameter to be S= 2.73±0.04 indicating the polarization entanglement of the generated two-photon state. We also constructed the density matrix of the state using linear tomographic technique [57]. Figure 6.4.1 (b) shows the graphical representation of density matrix of the generated state. From this analysis, we determine the state to be $\Psi_{Classical_1} = \frac{1}{\sqrt{2}}(|HH\rangle + |VV\rangle)$ and fidelity is 0.992.

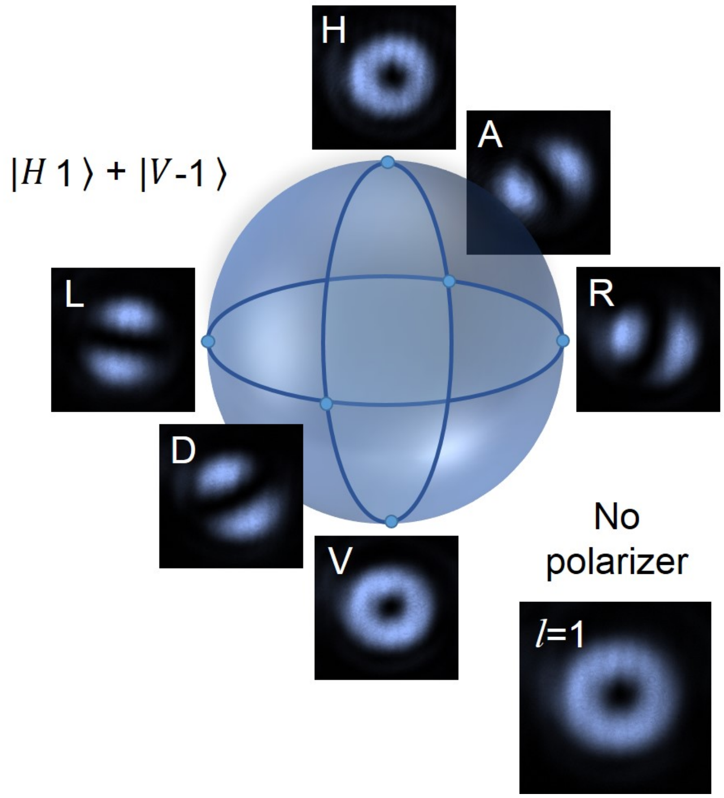

Figure 6.4.2: Intensity profiles of the non-separable states of the pump beam for two different OAM modes. Depending on the projection of the beam in different polarization states, $|H\rangle$, $|A\rangle$, $|R\rangle$, $|V\rangle$, $|D\rangle$, and $|L\rangle$ (as shown by the white letters on the images) on the Poincaré sphere, the mode pattern of the beam recorded by the CCD camera change to different points on LG-Bloch sphere for state $\frac{1}{\sqrt{2}}(|H1\rangle + e^{-i\phi}|V-1\rangle)$.

6.4.2 Preparation of classical non-seperable state

We prepared the classical pump beam in non-separable states [92] in OAM and polarization DoF by placing SPP inside the polarization Sagnac interferometer with phase variation corresponding to OAM mode of l=1, 2 and 3. The non-separable states of the pump beam incident to the nonlinear crystal can be expressed, $\Psi_{Classical_2} = \frac{1}{\sqrt{2}}(|Hl\rangle + e^{-i\phi}|V-l\rangle)$ with intensity distribution shown in Fig. 6.3.2 (a). To verify the non-separability, measurement in one DoF influence the outcome of the measurement in other DoF, we projected the pump

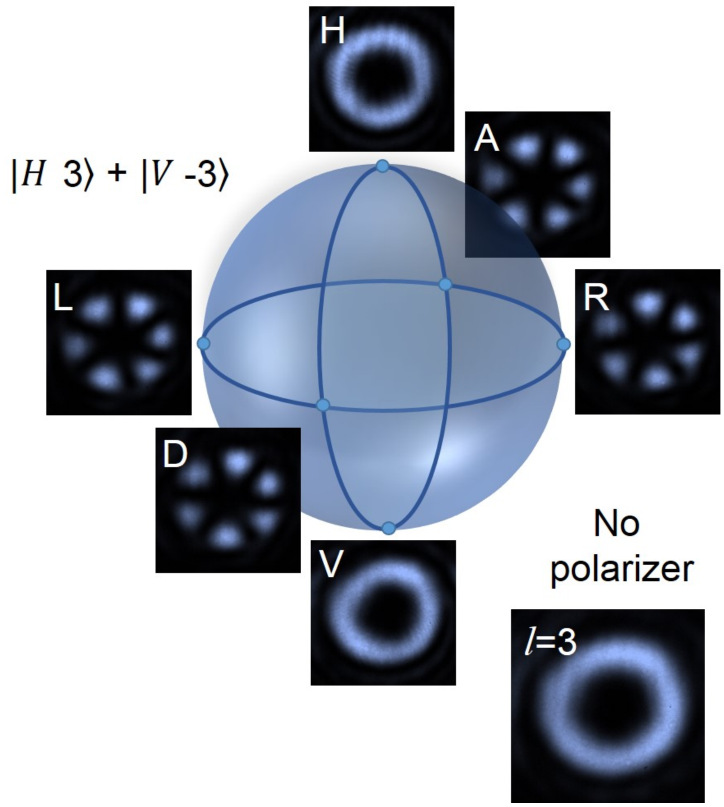

Figure 6.4.3: Intensity profiles of the non-separable states of the pump beam for two different OAM modes. Depending on the projection of the beam in different polarization states, $|H\rangle$, $|A\rangle$, $|R\rangle$, $|V\rangle$, $|D\rangle$, and $|L\rangle$ (as shown by the white letters on the images) on the Poincaré sphere, the mode pattern of the beam recorded by the CCD camera change to different points on LG-Bloch sphere for the state $\frac{1}{\sqrt{2}}(|H3\rangle + e^{-i\phi}|V-3\rangle)$.

state having OAM mode of l=1 and 3 at different polarization states, horizontal ($|H\rangle$), vertical ($|V\rangle$), anti-diagonal, ($|A\rangle$), diagonal ($|D\rangle$), left circular ($|L\rangle$) and right circular ($|R\rangle$) in Poincaré sphere and recorded the intensity of the beam with the results shown in Fig. 6.4.2 and Fig. 6.4.3 respectivley. As evident from figures, the projection of the pump state on $|H\rangle$ and $|V\rangle$ states result in vortex intensity profile with OAM order l and –l respectively. However, the projection on $|A\rangle$, $|D\rangle$, $|L\rangle$ and $|R\rangle$ states produce intensity distribution corresponding to the superposition of two opposite helical wavefronts of OAM order l resulting a ring lattice structure containing $2l$ number of petals at different orientation. All these projected intensity distributions can be represented by different points on LG-Bloch (Poincaré) sphere. The change in the images of Fig. 6.4.2 and Fig. 6.4.3 representing the projection of the pump state corresponding to OAM mode of $l = 1$ and 3 respectively corresponding to the change in polarization projection, verifies the generation of non-separable states. The inset image of Fig. 6.4.2 and 6.4.3 show intensity profile of the pump state without any projection.

6.4.3 Generation of hybrid entangled two photon state

With successful generation and verification of the non-separable states, we pumped the dual-BIBO crystal with the state, $\Psi_{Classical_2} = \frac{1}{\sqrt{2}}(|Hl\rangle + e^{-i\phi}|V-l\rangle)$, for direct transfer of classical non-separable states into hybrid entangled two photon states. According to the OAM conservation in nonlinear processes, the OAM of the pump photon should be equal to the sum of the OAMs of the generated signal and idler photons [97, 98], $l_s + l_i = l_p$. Here, l_p, l_s and l_i are the OAM of pump, signal and idler photons respectively. Since the OAM conservation law does not put any selection rule for the OAMs of the signal and idler photons, the OAMs of signal and idler can have arbitrary values with random variation owing to the conservation law. However, if we force signal or idler to carry fixed OAM value, then its partner photon will have a particular OAM with certainty. For example, if we project either signal or idler photons into Gaussian mode (l=0), then the OAM of

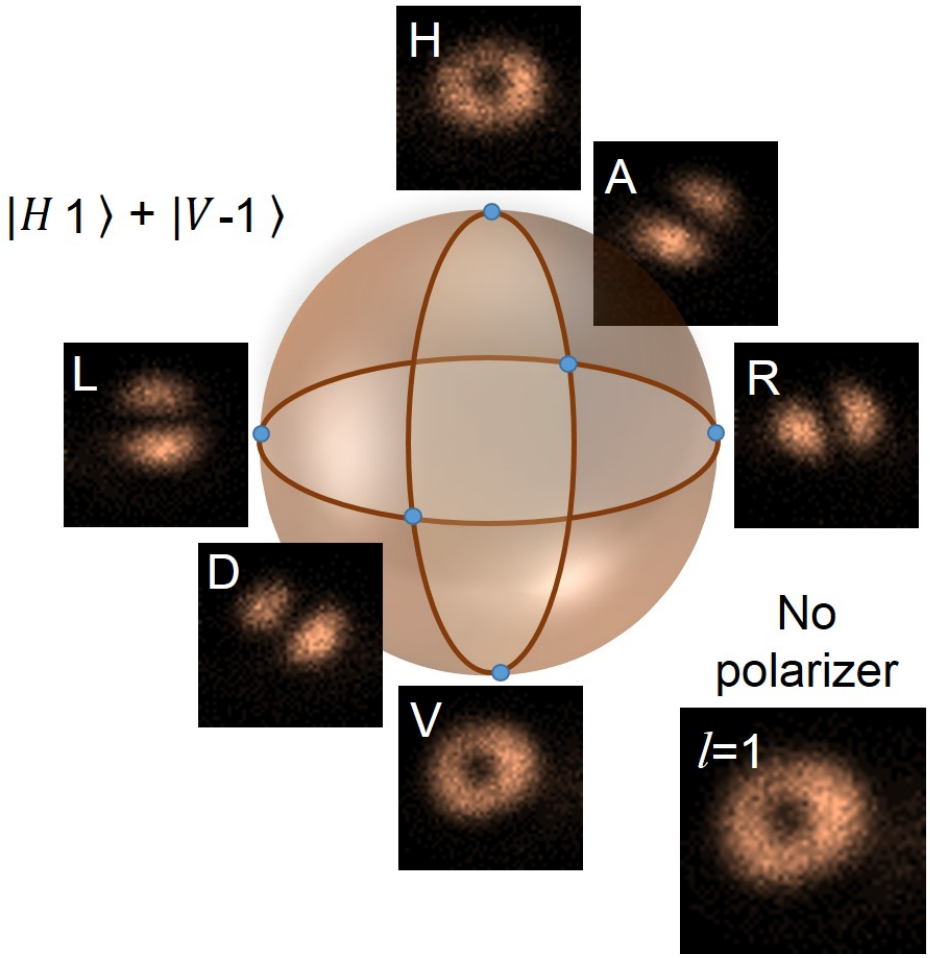

Figure 6.4.4: Gallery of images representing the probability distribution of the heralded signal photons. Depending on the polarization of the idler photon projected (white letters in the images) at different points in the polarization Poincaré sphere, the spatial distribution of the heralded signal change into different mode patterns in the LG-Bloch sphere. The sequence of coincidence images of the heralded signal due to particular polarization of its partner (idler) photon while pumping with non-separable states of first order ($l = 1$) LG modes around the meridian (vertical circle) and the equator (horizontal circle) in the LG-Bloch sphere confirms the generation of hybrid entangled two photon states encoded in polarization and OAM. In absence of any polarizer in the path of the idler photon, the spatial distribution of the heralded signal photon (inset) shows a statistical mixture of all states of the LG-Bloch sphere.

the idler or signal photon will be equal to that of pump photon indicating the possibility of direct transfer of the non-separable states in OAM and polarization DoF of the pump into one of the down converted photon. Therefore, in the present experiment, the state of the paired photons (considering idler photons in Gaussian mode) generated from the dual-BIBO crystal while pumped with non-separable states, $\Psi_{Classical_2} = \frac{1}{\sqrt{2}}(|Hl\rangle + e^{-i\phi}|V-l\rangle)$ can be written as per Eqn (5.2.10) is, $\Psi_2 = \frac{1}{\sqrt{2}}(|H,l\rangle + |V,-l\rangle)$, while the signal photon is projected by the analyzer in the D polarization. Here, the polarization degree of freedom of idler photon and OAM degree of freedom of signal photon are entangled. However, if the idler photon is projected in D polarization (for example) the paired photon state will transformed in to $\Psi_3 = |D0\rangle \otimes \frac{1}{\sqrt{2}}\left(|l\rangle + e^{-i\phi}|-l\rangle\right)$.

As a proof of principle, in the present experimental scheme, we pumped the crystal with non-separable states, $\Psi_{Classical_2}$ for two different values of OAM (l=1, 3) as shown in Fig. 6.4.2 and 6.4.3, and projected the photon (idler) of Arm-1 into Gaussian mode (l=0) using a lens and multi-mode fiber similar to the reports [17, 74] and measured the spatial distribution of the heralded photon (signal) in the form of coincidence counts per 10 sec in the transverse [x-y, see Fig 6.3.1 (a)] plane of Arm-2 with the results shown in Fig. 6.4.4. As evident from the gallery of images of Fig. 6.4.4 and Fig. 6.4.5 representing the spatial distribution of the heralded signal photon for the non-separable states corresponding to OAM mode of l=1 and l=3 respectively, the projection of the idler photon in Arm-1 to different states ($|H\rangle$, $|A\rangle$, $|R\rangle$, $|V\rangle$, $|D\rangle$, and $|L\rangle$) as marked by the white letters in the images) in the polarization Poincaré sphere with the help of $\lambda/4$ plate and analyser, A, directly projects the probability distribution of the heralded signal photons in Arm-2 in a ring lattice spatial structure with $2l$ number of petals to different points on the LG-Bloch sphere. Such observation intuitively gives the impression of generation of hybrid entangled two photon states through the direct transfer of non-separable states of the pump.

However, for confirmation and quantitative study of the entanglement we explore the features of the LG modes. It is well known that the superposition of any two equal OAM modes with opposite helicities, $|LG_{\pm l}\rangle = \frac{1}{\sqrt{2}}\left(|l\rangle + e^{-i\phi}|-l\rangle\right)$ results in radially symmetric ring lattice with $2l$ number of petals. However, the relative phase, ϕ between the two

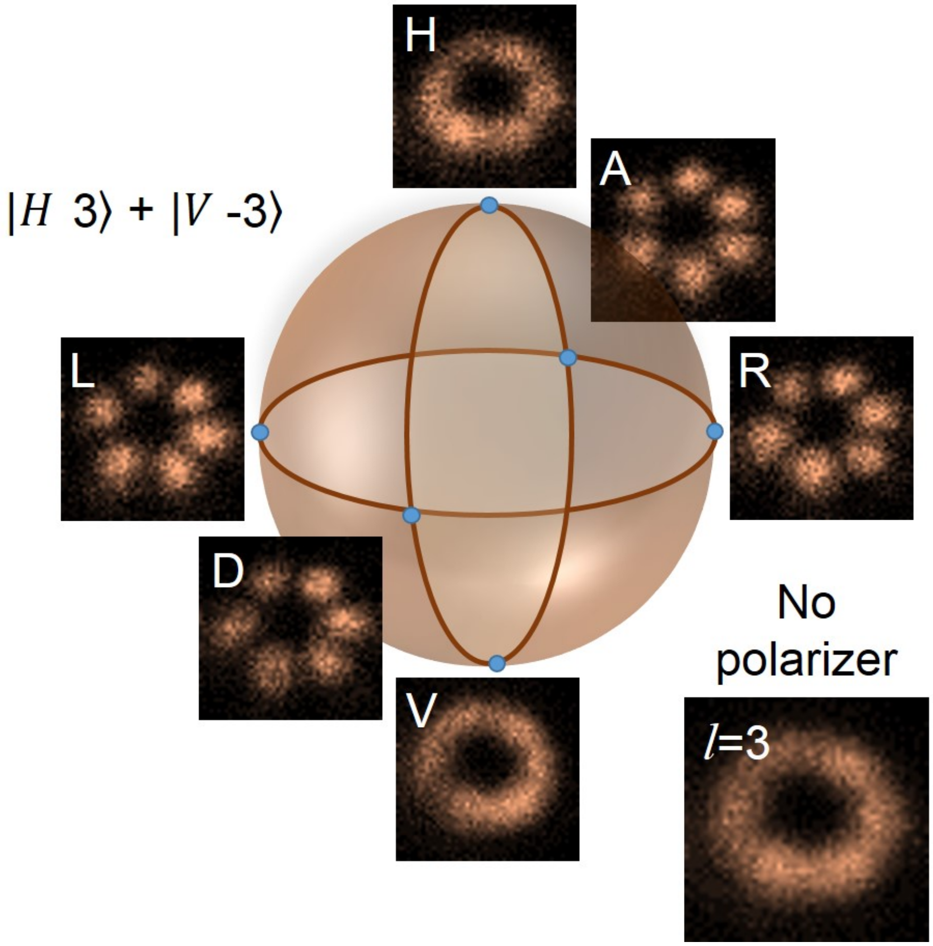

Figure 6.4.5: Gallery of images representing the probability distribution of the heralded signal photons. Depending on the polarization of the idler photon projected (white letters in the images) at different points in the polarization Poincaré sphere, the spatial distribution of the heralded signal change into different mode patterns in the LG-Bloch sphere. The sequence of coincidence images of the heralded signal due to particular polarization of its partner (idler) photon while pumping with non-separable states of third order ($l = 3$) LG modes around the meridian (vertical circle) and the equator (horizontal circle) in the LG-Bloch sphere confirms the generation of hybrid entangled two photon states encoded in polarization and OAM. In absence of any polarizer in the path of the idler photon, the spatial distribution of the heralded signal photon (inset) shows a statistical mixture of all states of the LG-Bloch sphere.

OAM modes results in spatial rotation of $\frac{\phi}{2\pi}\frac{360^\circ}{2l}$ [75] which can in principle be used to identify and discriminate between different superpositions of the OAM modes. To distinguish the spatial rotation and therefore different superpositions for the verification of entanglement in OAM and polarization DoF we have evaluated the coincidence of the heralded signal photons per angular region,θ, from the coincidence images (see insets of Fig. 6.4.6) for the idler polarization in mutually unbiased bases, $|A\rangle$, $|D\rangle$ and $|R\rangle$, $|L\rangle$ for the pump OAM mode, l=1 and l=3 with the results shown in Fig. 6.4.6 (a) and Fig. 6.4.6 (b) respectively. Let's assume that at an angle θ, we have the maximum coincidence for anti-diagonal (A) projection. The n^{th} maxima in the same projection appears at an angle, $\theta + n\frac{360^\circ}{2l}$, where n is an integer in the range, $1 \leq n \leq 2l$. The angular separation between two consecutive maxima is, $\frac{360^\circ}{2l}$. On the other hand, in mutually unbiased (say, L) and orthogonal (D) basis the maxima will shift to an angle $\theta + \frac{45^\circ}{l}$ and $\theta + \frac{90^\circ}{l}$ respectively. As evident from Fig. 6.4.6 (a), for OAM mode, $l = 1$, two consecutive maxima in A-projection (black dots) occur at $\theta = 0^\circ$ and $\theta + \frac{360^\circ}{2l} = 180^\circ$ and the maxima in the L- (blue dots) and D- (red dots) projections have angular shift of angle $\theta + \frac{45^\circ}{l} = 45^\circ$ and $\theta + \frac{90^\circ}{l} = 90^\circ$ respectively with respect to A-projection. Similarly in case l =3, as evident from Fig. 6.4.6 (b), we observe two consecutive maxima in same projection basis to have an angular separation of 60° and the maxima in the L- (blue dots) and D- (red dots) projections have angular shift of angle 15° and 30° respectively with respect to maxima in A-projection. Such spatial rotation of the OAM mode of the heralded signal photon for the projection of the idler at different points in the polarization Poincaré sphere confirms the entanglement in both OAM and polarization DoF.

To estimate the entanglement quality we have calculated the entanglement witness operator, $\widehat{W} = V_{(R/L)} + V_{(D/A)}$ using the quantum interference visibilities, $V_{(R/L)}$and $V_{(D/A)}$ in two mutually unbiased bases R/L and D/A respectively. For all separable states, the entanglement witness operator satisfies the inequality, $\widehat{W} \leq 1$ and exceeding the limit verifies

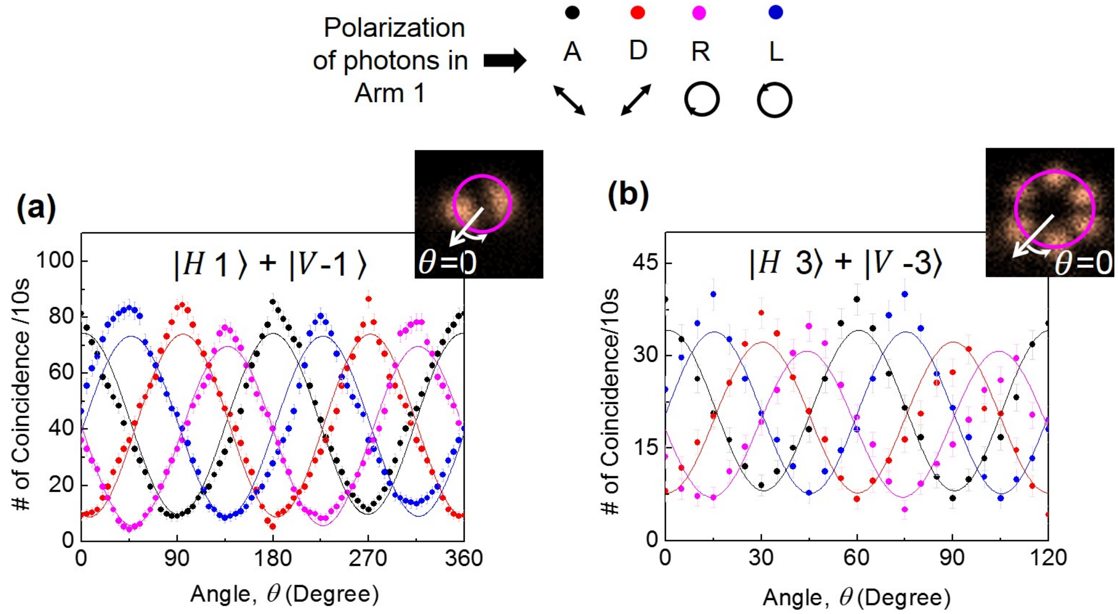

Figure 6.4.6: (a) Coincidence per angular region for A (black dots), D (red dots), R (pink dots) and L (blue dots) projections of the idler photon for OAM l=1, (b) for l=3. The lines are theoretical fit to experimental data. (Inset) Image of the probability distribution of the heralded signal photons. Errors are estimated from iteration.

entanglement [75, 99]. Using the values of $V_{(R/L)}$ and $V_{(D/A)}$ we estimate the entanglement witness operator for OAM mode $l = 1, 2$, and $l = 3$ to have a value $\widehat{W}$= 1.56±0.04, 1.40±0.04 and 1.25±0.03, clearly violating the inequality by more than 14, 10 and 8 standard deviation respectively. It is to be noted that we did not apply any background correction to the experimental results. Slight lower violation of inequality in case $l = 3$ with respect to that of $l = 1$ can be attributed to error in visibility data due low signal to noise ratio in the spatial distribution of the lower number of down converted photons. The stronger violation requires increase in the number of down converted photons. However, the present study confirms generated twin photons are entangled in both OAM and polarization DoF.

6.5 Conclusion

In conclusion, we have successfully demonstrated a novel scheme of generating hybrid entangled two photon states. Pumping a contiguous nonlinear crystal using non-separable states of pump beam of OAM mode of l=1 and 3 we have generated two photon hybrid entangled states. Characterization of the generated quantum state through tomography, and violation of Bell's inequality parameter shows high quality polarization entanglement whereas, the measurement of entangled witness parameter verifies the generation of two photons state entangled in both OAM and polarization DoFs. The concept is generic and can be used to produce hybrid entangled states with higher quanta of OAM and photons with arbitrarily high difference in OAM through the proper selection of the nonclassical state of the pump beam.

Chapter 7

Bi-photon orbital angular momentum eigen modes in SPDC process

7.1 Introduction

Quantum entanglement, the strong non-classical correlations in the joint measurement of two separate quantum systems, plays crucial role in variety of applications in quantum information processing, including quantum communication, quantum cryptography and teleportation [28, 78, 79]. So far, the quantum entanglement has been implemented mostly in photonic systems. The vast majority of the entangled photons are generated through spontaneous parametric down-conversion (SPDC) of high energy photon into low energy correlated photon pair [13]. With the first demonstration of entanglement with polarization [76], different degrees of freedom, such as spatial modes [4], time-energy [35] as well as continuous variables [100] have been used. Similarly, efforts have been made to produce photon pairs entangled between two different DoFs for example, polarization and spatial modes [12]. While entanglement in different DoFs have their own advantages and limitations, the entanglement in spatial modes e.g. orbital angular momentum (OAM) of photons has attracted great attention in recent times [4]. This is due to the fact that the OAM modes are discrete, integer valued, and form a theoretical infinite-dimensional Hilbert space essential for high dimensional entangled quantum states. The high dimensional entanglement not only increases the channel capacity [101], but also provides stronger violation of locality [102] and increases the security and robustness from eavesdropping.

The number of OAM modes generated in the SPDC process, commonly referred as the spiral bandwidth, dictates the OAM entanglement and the dimensionality of the system. The OAM modes of the SPDC process are commonly expressed in terms of bi-photon eigen modes of the paraxial OAM operators [96]. Mathematically the complete set of OAM eigen modes generated in SPDC process for the pump OAM mode of l_p are represented as, $\sum_{l_p=-\infty}^{\infty}\sum_{l_i=-\infty}^{\infty} C_{is} |l_i\rangle \left|l_p - l_i\right\rangle$. Here, li and $(l_p – l_i)$ are the idler and signal OAM modes, respectively, and C_{is} is eigen value corresponding to the state $|l_i\rangle \left|l_p - l_i\right\rangle$ generated in SPDC process. While efforts have been made to understand the effect of pump profile and phase matching on bi-photon eigen modes [96, 103], the majority of such studies have dealt with the OAM entanglement using with Gaussian pump, $l_p = 0$. In such cases, the bi-photon eigen modes represented as, $\sum_{l_i=-\infty}^{\infty} C_{is} |l_i\rangle |-l_i\rangle$ span a single subspace in the OAM Hilbert space. While manipulation of pump beam waist radius and the crystal parameters can increase the spiral bandwidth of the OAM mode, however, the bi-photon eigen modes are restricted to the same subspace. Similarly, one can manipulate the spatial mode of the pump beam and directly generate the spatially entangled states [104]. However, complete access to the bi-photon eigen modes, $\sum_{l_p=-\infty}^{\infty}\sum_{l_i=-\infty}^{\infty} C_{is} |l_i\rangle \left|l_p - l_i\right\rangle$ in the OAM Hilbert space require pump beam to carry superposition of OAM modes.

Optical vortices, having the phase distribution represented as $\exp(il\theta)$, where θ is the azimuthal angle and the integer l, known as vortex order or topological charge of the vortex, carry OAM of $l\hbar$ per photon. Typically, the optical vortices are produced through the spatial mode conversion of Gaussian laser beams using mode converters including spiral phase plates (SPPs), q-plates and the computer generated holography technique based spatial light modulators (SLMs). Most of these mode converters are designed to generate a single valued OAM mode, l [21]. On the other hand, fractional optical vortex beam contains large number of integer OAM modes with different weightage. Recently, it is observed that the off-axis vortex (asymmetric vortex) beams have broad OAM modal distribution [27, 26]. Using such asymmetric optical vortex beam, here, we investigate the OAM eigen modes of the bipartite system generated in SPDC process. Using SPP and simply shifting its optic axis with respect to the beam propagation axis, we have generated pump beam with a broad spectrum of OAM modes of different weightages. Pumping the nonlinear crystal with such asymmetric vortices we directly transferred the pump OAM spectrum to the down converted photons producing bi-photon eigen modes spanned over more number of subspace in the OAM Hilbert space. Calculation on Schmidt number [105] shows that the increase in the OAM modes with increase in asymmetry in the pump vortices. Additionally, shifting the SPP we can tune and access any particular subspace of the OAM Hilbert space. To the best of our knowledge, this is the first experimental report on controlling the OAM eigen modes of the bi-photon state spanned by the pump OAM modes.

7.2 Experimental scheme

The schematic of the experimental setup is shown in Fig. 7.2.1. A continuous-wave, single-frequency (line-width <12 MHz), diode laser of 100 mW output power at 405 nm in Gaussian spatial profile (TEM00 mode), is used as the pump source. The combination of a half-wave plate ($\lambda/2$) and polarising beam splitter (PBS1) cube controls the laser power to the experiment. Using the spiral phase plates, SPP1 and SPP2, having phase-winding numbers, m= 1 and 2, respectively, and the vortex doubler setup [21], comprised of PBS1, quarter-wave plate ($\lambda/4$) and a mirror (M), we have converted the Gaussian pump beam into vortex beam of orders (OAM modes), l_p=1 to 6. The vortex beams have symmetric intensity distribution and carry OAM mode, l_p, equal to the phase winding numbers, m, of

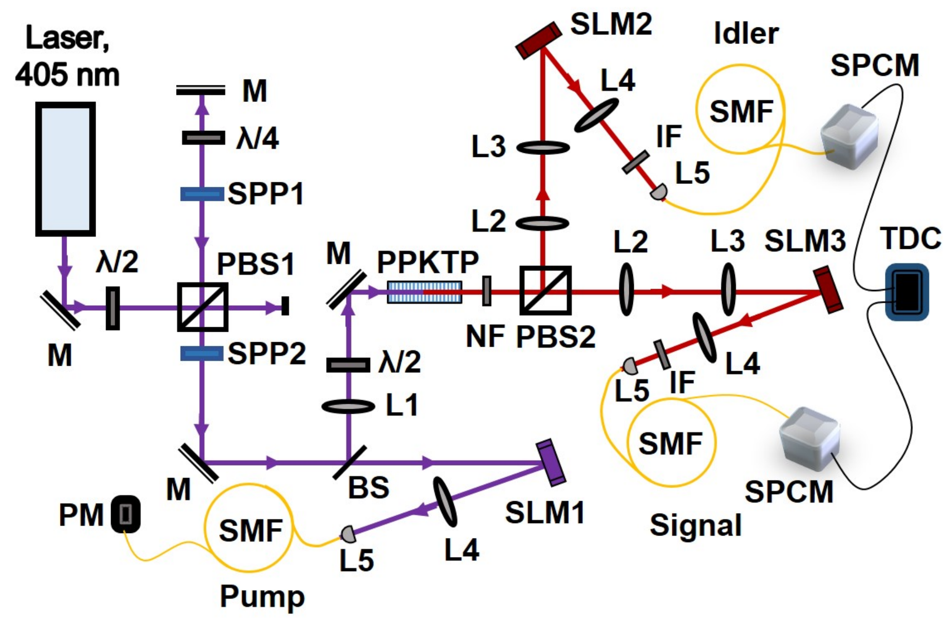

Figure 7.2.1: Schematic of the experimental setup. $\lambda/2$, $\lambda/4$, half-wave plate and quarter wave plate at 405 nm, respectively; PBS, polarizing beam splitter cube at 405 nm and 810 nm respectively; SPP1-2, spiral phase plate; M, mirrors; L1-5, lenses; PPKTP, non-linear crystal in a temperature oven; SLM, spatial light modulator; IF, interference filter; NF, notch filter; SMF, single mode fibre; SPCM, single photon counting module; TDC, coincidence counter; PM, power meter

the SPPs when the optic axis of the SPP coincide with the beam propagation axis. However, any misalignment in terms of tilt and or displacement between the beam propagation axis and the optics axis of the SPPs create asymmetry in the intensity distribution of the generated vortex beam. The resultant beam carries a broad OAM mode spectra and the distribution of the mode spectra vary with the asymmetry of the vortex beam. A fraction of the pump beam intensity transmitted through the beam splitter (BS) is used to study pump OAM modes.

Using the lens, L1, of focal length, $f1$=750 mm, the pump beam is focused at the centre of a 30 mm long, 2×1 mm^2 in aperture, periodically poled potassium titanyl phosphate (PPKTP) having single grating of period, Λ=10 μm, for type-II (e→o+e) phase-matched degenerate, collinear down conversion of pump beam in to 810 nm. Since the degenerate photons have orthogonal polarization states, we have considered the photons in horizontal and vertical polarization states as signal and idler, respectively. The notch filter (NF) removes the undepleted pump from the signal and idler. We have separated the signal and idler in transmitted and reflected ports, respectively, of the PBS2. Using the lenses, L2 and L3 of focal lengths, $f2$=100 mm and $f3$=500 mm in $2f2-2f3$ combination we imaged the signal and idler photons with 5X magnification on the surface of SLM2 and SLM3, respectively. The OAM content of the pump, signal and idler are measured using the projective technique [106], where, the incident photons are diffracted by the SLM (SLM1, SLM2 and SLM3) having blazed fork grating of different OAM orders. The first order diffracted photons are coupled to a single mode fibre by re-imaging the SLM plane with the lens combination, L4 and L5 ($f4$=750 mm and $f5$=4.6 mm), in $2f4-2f5$ configuration and subsequently measured using a detector. A power meter (PM) measures the power distribution of the pump OAM modes. The single photon counting modules (SPCMs) and the time to digital convertor (TDC) measure the coincidence of the signal and idler photons. We have used a coincidence window of 8.1 ns. The interference filter (IF) has a transmission bandwidth of 2.1 nm centred at 810nm.

7.3 Results and discussion

7.3.1 Generation and characterization of asymmetric pump vortex beam

We have studied the OAM spectra of the asymmetric vortex beam by measuring the far-field intensity profile and corresponding OAM modes of the pump vortex beam with the results shown in Fig. 7.3.1. To create the asymmetric position of the dark core of the vortex beams, we have moved the SPPs with respect to the beam axis with a normalized distance,

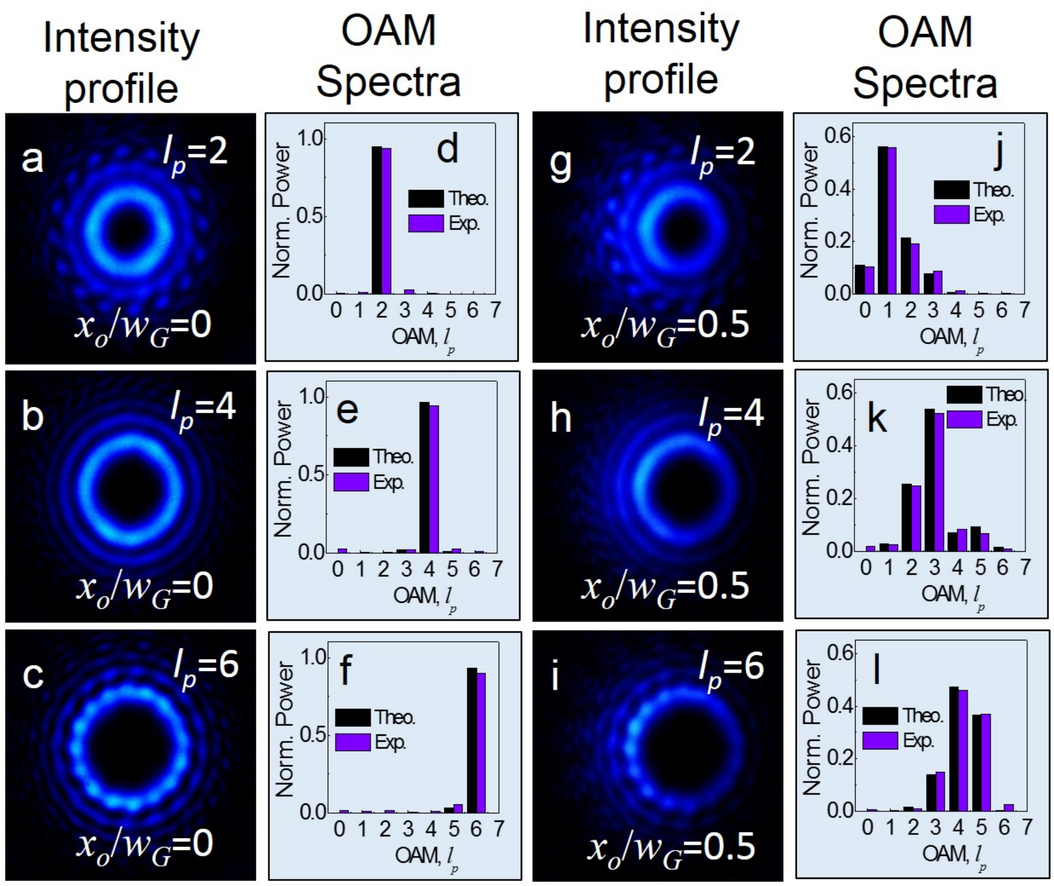

Figure 7.3.1: (a-c) Far-field intensity distribution of symmetric vortex beam (x_o/w_G=0) and (d-f) corresponding OAM spectra, (g-i) intensity distribution of the asymmetric (x_o/w_G=0.5) pump vortex beams and (j-l) corresponding OAM spectra, of orders, l_p= 2, 4, and 6. The black and violet bars represent the theoretical and experimental results respectively..

x_o/w_G [26]. Here, x_o is the shift of the optic axis of SPP away from the beam propagation axis and w_G=1.2 mm, is the full-width at half-maximum (FWHM) radius of the Gaussian beam at the SPP plane. Using SPP1 and SPP2 in the vortex doubler setup and adjusting the optic axes of the SPPs with respect to the beam propagation axis so that x_o/w_G=0, we have recorded the intensity profile of the vortex beams. As evident from first column, (a-c), of Fig. 7.3.1, the vortex beams have symmetric intensity distribution with increasing dark core size.

We have measured the OAM modes of the symmetric vortex beams, as shown in the second column, (d-f), of Fig. 7.3.1, to be l_p=2, 4, to 6, respectively. However, as evident from the third column, (g-i), of Fig. 7.3.1, the shift in the SPPs position by a normalized distance of, x_o/w_G=0.5, results asymmetric intensity distribution of the vortex beams with the dark core moved away from the beam propagation axis. Similar to our previous report [26], the increase in shift distance, x_o/w_G, pushes the dark core of the vortex beam away from the centre of the beam resulting larger asymmetry in the beam. Since the azimuthal phase variation in the beam is no longer uniform with respect to the beam axis, one can expect the beam to carry a distribution of OAM modes. Fourth column, (j-l), of Fig. 7.3.1, shows the measured OAM mode distribution of the asymmetric vortex beams generated for, x_o/w_G=0.5. It is evident from Fig. 7.3.1, that the shift of SPPs from x_o/w_G=0 to 0.5, transform the OAM modes, l_p=2, 4, and 6 to a distribution of OAM modes of (0, 1, 2, and 3), (2, 3, and 4) and (3, 4 and 5), respectively. Using the mathematical formula of Ref. [107] we have calculated the OAM mode distribution (black bars) of the asymmetric vortex beams for our experimental conditions and found a close agreement with our experimental results (violet bars). As predicted [107] and experimentally verified , here, we also observe the variation in OAM mode distribution of the asymmetric vortex with x_o/w_G. For very high asymmetry, $x_o/w_G \gg 1$, one can reach to the Gaussian mode. Using this technique, it is evident that one can control the OAM mode distribution of a vortex beam of OAM mode,

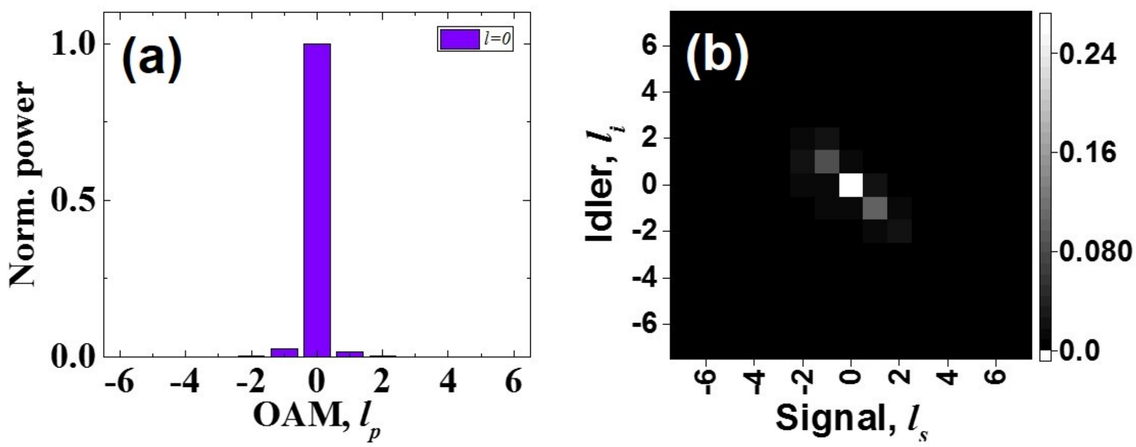

Figure 7.3.2: (a) OAM spectrum of pump Gaussian and (b) measured bi-photon eigen OAM modes in SPDC process.

l_p, into the mixture of OAM modes, l_p,l_p-1,l_p-2,...,0 of different weightages by simply shifting the optic axis of SPPs away from the beam propagation axis.

7.3.2 Study of bi-photon OAM eigen modes with Gaussian pump beam

To verify the reliability of the projective measurement setup, we first have measured the OAM bi-photon eigen modes by using Gaussian pump beam. Using a CCD camera we have estimated the beam waist radius of the Gaussian pump beam at crystal to be, w_p ~60 μm. Similarly, using back alignment technique [106], we have measured the waist radius of the signal and idler beams to be $w_s, w_i \sim 60$ μm ensuring the ratio, ~ 1, at the crystal plane to ensure optimum collection of the generated photons. Projecting the signal and idler photons in different OAM modes and measuring their coincidence counts we have measured the bi-photon OAM eigen modes for the Gaussian pump beam and consequently estimated the Schmidt number. Figure 7.3.2 (a) and (b) shows the pump OAM spectra and bi-photon OAM eigen modes respectively. Using the mathematical expression of the

Schmidt number,

$$K = \beta \left(\frac{w_p^2 + 4\alpha^2 b^2}{4 w_p \alpha b} \right)^2$$

, of Ref. [15], where $\alpha = 0.85$,$\beta = 1.65$, $b = \sqrt{L/4k_p}$, w_p, and k_p are the beam waist radius and the wave vector of the pump respectively, and L is the length of the crystal, we have calculated the Schmidt number to be, K_{theo} ~2.82, close to the measured value of, K_{exp}~2.86. Such close agreement between the experimentally measured Schmidt number to that of the theoretical Schmidt number confirms the reliable measurement capability of our OAM detection system.

7.3.3 Generation of bi-photon OAM eigen modes with asymmetric vortex beam

Using the same detection system, we pumped the crystal with vortex beam of order, l_p=6, with varying x_o/w_G value and measured the bi-photon OAM eigen modes of the down converted photons. The results are shown in Fig. 7.3.3. As evident from the first column, (a-c), of Fig. 7.3.3, the pump OAM spectra is varying from a single mode, l_p=6 at x_o/w_G =0 to a distribution of OAM modes, l_p=4, 3 and 2 at x_o/w_G =0.75, and l_p=3, 2 and 1 at x_o/w_G =1.25 with different weightages. From the second column, (d-f), of Fig. 7.3.3, it is evident that the bi-photon OAM eigen modes belong to the subspace spanned by OAM mode of, l=6, for the pump beam of single OAM mode, l_p=6, satisfying OAM conservation in down conversion process. However, with the increase in asymmetry of the pump vortex beam resulting from x_o/w_G=0, 0.75 and 1.25 we observe the increase in the span of bi-photon OAM eigen modes. Such broadening in the OAM eigen modes of the bi-photons can be understood as follows. As the OAM modal distribution of the pump beam broadens with the beam asymmetry, the generation of bi-photon OAM eigen mode by the constituting pump OAM modes of the asymmetric vortex beam result in the broadening of spiral spectrum.

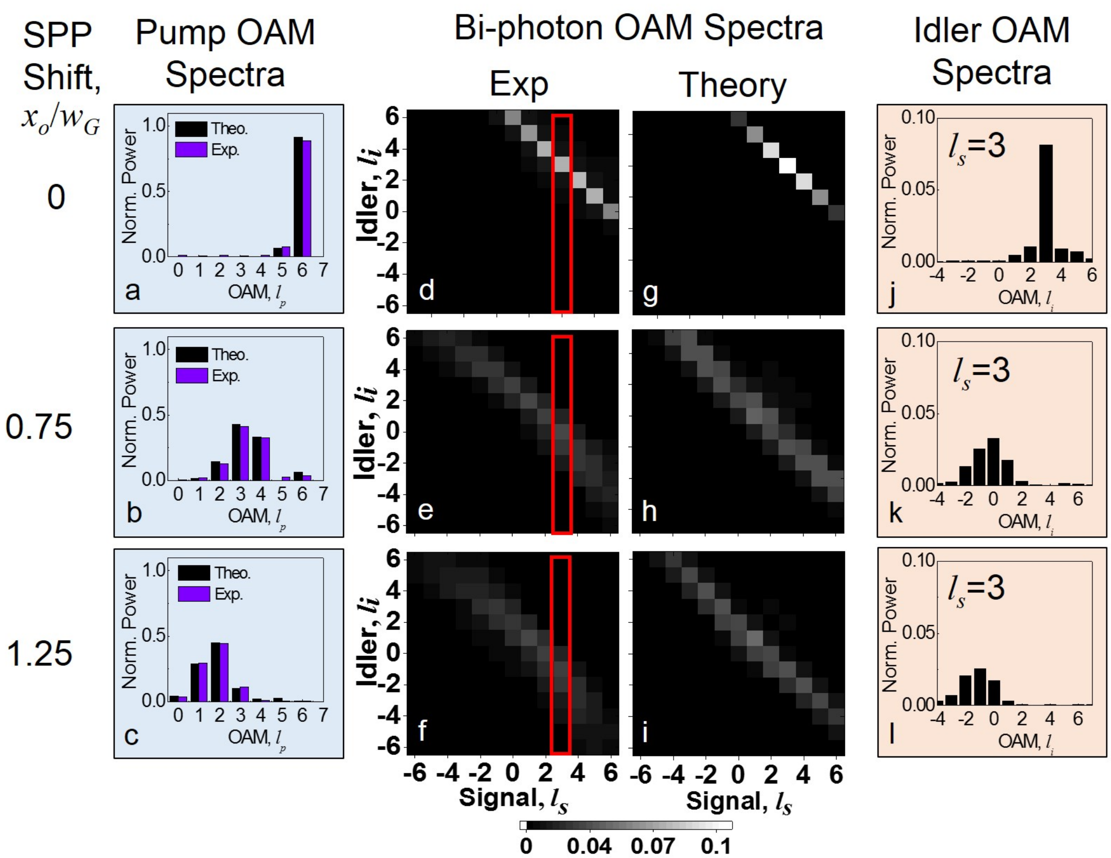

Figure 7.3.3: (a-c) Distribution of OAM modes of asymmetric pump beam of x_o/w_G= 0, 0.75 and 1.25, corresponding spiral spectrum for bi-photon OAM eigen modes (d-f), measured and (g-i) simulated. (j-l) A portion of the spiral spectrum of idler at a fixed OAM mode (l_s=3) of the signal.

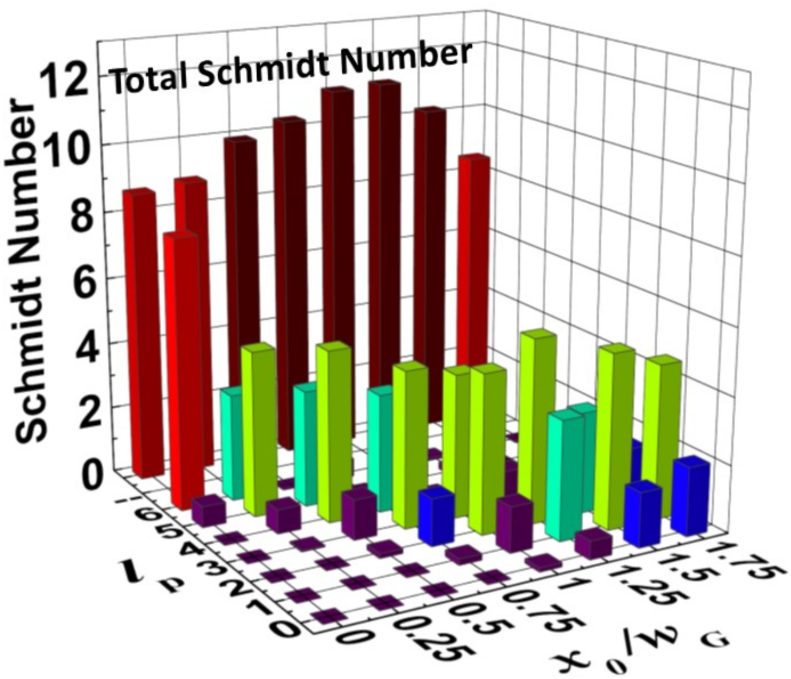

Figure 7.3.4: Variation in the measured value of Schmidt number, K, as a function of asymmetry in the pump vortex beam.

Using our experimental parameters, we have simulated [108] the bi-photon OAM eigen modes with results shown in third column, (g-i) of Fig. 7.3.3, in close agreement with our experimental results. To gain further insight on broadening of spiral bandwidth of the down converted photons, we have analysed the OAM mode distribution of the idler photons for a fixed signal OAM mode of l_s=3 [see the red boxes of Fig. 7.3.3 (d-f)]. The results are shown in fourth column, (j-l), of Fig. 7.3.3. We can clearly see the broadening of the OAM eigen modes of the bi-photons, a close resemblance to the OAM spectrum of the asymmetric pump vortices. It is also evident from the present study that one can tune the spiral bandwidth of the bi-photon eigen modes by simply adjusting the optic axis of the SPPs with respect to the beam propagation axis.

As the pump OAM spectrum vary with its asymmetry and the pump OAM mode, l_p, spans the OAM eigen-modes of the bi-photons, we have studied the effect of pump beam asymmetry on the Schmidt number, K. Using the pump vortex order, l_p=6, we have calculated the Schmidt number for OAM modes, l_p=1 to 6 with asymmetry parameter x_o/w_G. The results are shown in Fig. 7.3.4. As evident from the Fig. 7.3.4, the pump vortex beam with asymmetry, x_o/w_G =0 has OAM mode of, l_p=6, and a total calculated Schmidt number of, K=8.05 with major contribution from the pump OAM mode, l_p=6. However, with the increase of asymmetry, x_o/w_G, from 0 to 1.75, we observe a varying distribution of pump OAM modes, l_p, l_p-1, l_p-2,..,0 of different weights, and the corresponding Schmidt numbers. It is also interesting to note that the total Schmidt number, the sum of the Schmidt numbers of individual OAM modes, l_p, varies from 8.68 to 8.52 for the increase of x_o/w_G from 0 to 1.75 with a maximum of 11.01 at the pump beam asymmetry of, x_o/w_G=1. Such increase in the total Schmidt number, a measure of total number of bi-photon OAM eigen modes, can be attributed to the broadening of the OAM spectra of the pump beam near the asymmetry of, x_o/w_G=1.

7.3.4 Measurement of two dimensional bi-photon OAM entangled state

We have studied the effect of vortex asymmetry on the quality of two dimensional OAM entangled states by performing the state tomography for different values of asymmetry parameter, x_o/w_G. The results are shown in Fig. 7.3.5. Pumping the crystal with vortex beam of OAM mode, l_p=2, we have generated the Bell state, . The Fig. 7.3.5 (a)-(c) show the real parts of the density matrix of measured Bell state for the pump vortex asymmetry, x_o/w_G=0, 0.25 and 0.5, respectively. It is evident from Fig. 7.3.5 (a)-(c) that the density matrix of the Bell state change with the increase in asymmetry of the pump vortices from x_o/w_G=0, 0.25 and 0.5. To get further insight, we have measured the Bell state fidelity

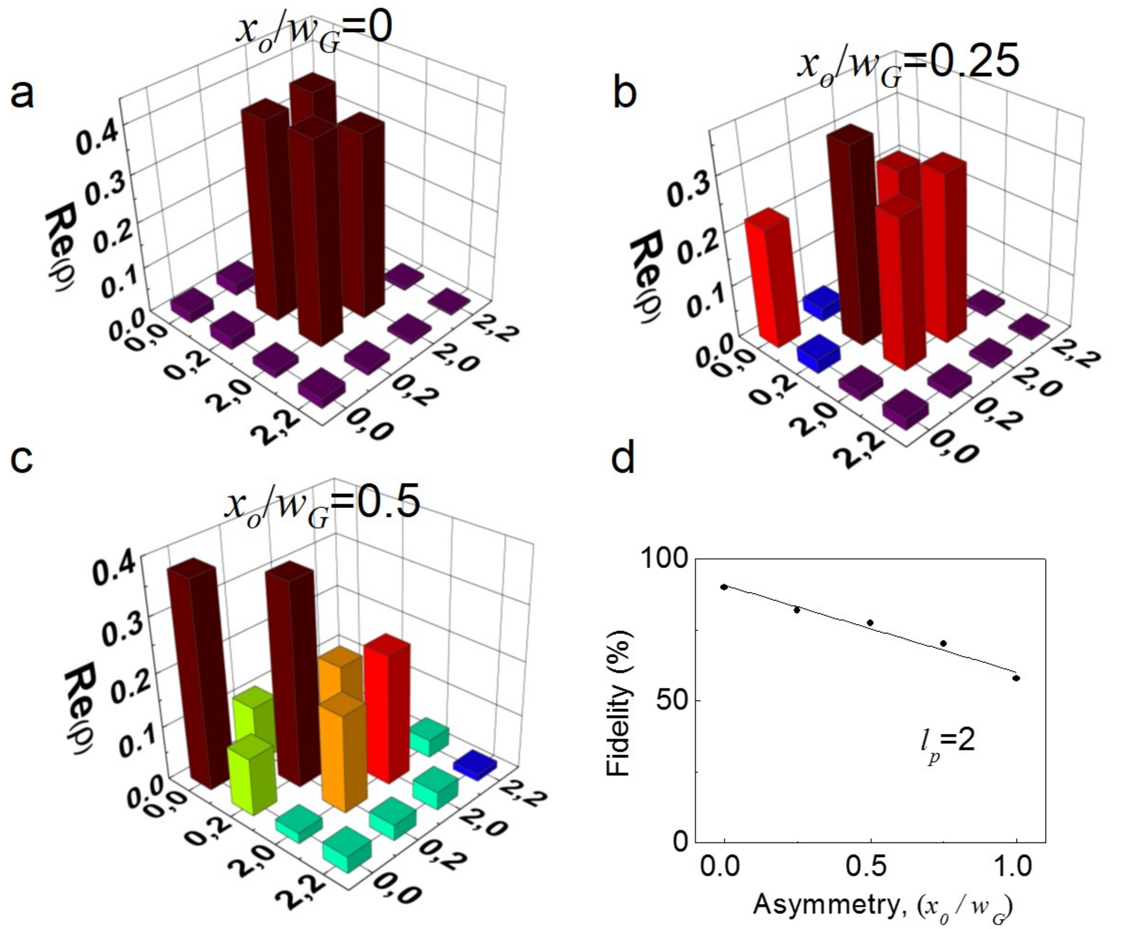

Figure 7.3.5: (a-c) Variation of the density matrix of two dimensional OAM entangled state with the asymmetry, x_o/w_G= 0, 0.25 and 0.5 of pump vortex OAM mode, l_p=2. (d), The change in the fidelity of the state with pump beam asymmetry.

for different asymmetries in the pump vortices with the results shown in Fig. 7.3.5 (d). It is evident from the Fig. 7.3.5 (d) that the fidelity of the Bell state decreases with the increase in asymmetry of the pump vortex beam. Such decrease in the fidelity of the Bell state can be attributed to the cross talk among different modes of the higher dimensional OAM entangled state. One can, in principle, obtain high fidelity by considering higher dimensional bases in the measurement.

7.4 Conclusion

In conclusion, we have tailored the OAM mode distribution of a vortex beam from the single mode to a mixture of OAM modes by controlling the asymmetry in its intensity distribution. Using such tailored pump OAM spectra we have studied the bi-photon OAM eigen modes in the down conversion process. The direct correlation of the pump OAM spectra to the bi-photon OAM eigen modes in SPDC process confirms the direct control of spiral bandwidth of the entangled photons. We have quantified the broadening of the bi-photon OAM eigen modes by calculating the Schmidt number, and observe the enhancement in the dimensionality of the bi-photon OAM eigen modes by tailoring the asymmetry of the pump vortices. This generic method may be utilized for increasing the information capacity of various quantum information protocols.

Chapter 8

Conclusion and scope for future work

8.1 Conclusion

In this doctoral thesis, we have presented the study of generation and characterization of different quantum entangled systems based on spontaneous parametric down conversion process. With the help of different structured beam we have investigated the effect of transverse profile of the pump beam on entanglement properties.

In Chapter 1, we have given the the motivation and objective of the thesis work, along with brief content of the each chapter. In chapter 2, we have covered the basics of quantum entanglement which were extensively used throughout my Ph.D work. It covers the spontaneous parametric down conversion process, one of the popular source of entangled photons. We also included the discussion of different parameters like phase-matching and pump transverse profile with brief introduction to different structured beam in this chapter.

In chapter 3, we have demonstrated a simple, compact and robust source of entangled photons at high brightness. Based on non-collinear, degenerate, type-0 phase-matching of a single PPKTP crystal at room temperature in a Sagnac interferometer, the detected paired photons rate of 0.41±0.02 MHz/mW/nm. This is the highest number of degenerate paired photons detected with the help of multimode fiber from a bulk crystal pumped with a continuous-wave laser. We have studied the dependence of pump focusing on the brightness of the generated photons collected using both multimode, and single mode fibers. For a fixed pump power and crystal parameters, the SPDC source has an optimum pump waist radius producing maximum number of paired photons. Even in the absence of any phase compensation, the entangled photon states detected using single mode fiber have a Bell's parameter, S=2.63$\pm$0.02, violating the Bell's inequality by nearly 32 standard deviations and fidelity of 0.975.

In chapter 4, we introduce "perfect" vortex, is a new class of optical vortex beam having ring radius independent of its topological charge (order). We demonstrated a novel experimental scheme to generate perfect vortex of any ring radius using a convex lens and an axicon. As a proof of principle, using a lens of focal length f=200mm, we have varied the radius of the vortex beam across 0.3-1.18 mm simply by adjusting the separation between the lens and axicon. This is also a simple scheme to measure the apex angle of an axicon with ease. Using such vortices we have studied non-collinear interaction of photons having orbital angular momentum (OAM) in spontaneous parametric down-conversion (SPDC) process and observed that the angular spectrum of the SPDC photons are independent of OAM of the pump photons rather depends on spatial profile of the pump beam. We observed that in the presence of spatial walk-off effect in nonlinear crystals, the SPDC photons have asymmetric angular spectrum with reducing asymmetry at increasing vortex radius. In chapter 5, we experimentally demonstrated, that the spatial profile of classical beam can be directly transferred to the spatial profile of the polarized entangled bi-photon modes. Correlation measurement and the Bells parameter indicate the presence of polarization entanglement even after pumping with the vortex beam.

In chapter 6, we have successfully demonstrated a novel scheme of generating hybrid entangled two photon states. Pumping a contiguous nonlinear crystal using non-separable states of pump beam of OAM mode of l=1 and 3 we have generated two photon hybrid entangled states. Characterization of the generated quantum state through tomography, and violation of Bell's inequality parameter shows high quality polarization entanglement whereas, the measurement of entangled witness parameter verifies the generation of two photons state entangled in both OAM and polarization DoFs. As a proof of principle, using local non-separable pump states of OAM mode l=3, we have produced quantum hybrid entangled states with entanglement witness parameter of $\sim$1.25$\pm$0.03 violating by 8 standard deviation. The generic scheme can be used to produce hybrid entangled states between two photons differing by any quantum number through proper choice of non-separable states of the pump beam.

In chapter 7, we introduced the concept of asymmetric vortex beam. We have shown that adjusting the optic axis of the spiral phase plate (SPP) of phase winding corresponding to OAM mode, l, with respect to the beam propagation axis, we have transformed a Gaussian beam into an asymmetric vortex beam with OAM modes, l, $l-1$, l-2 . . . 0 with different weightages. We have tailored the OAM mode distribution of a vortex beam from the single mode to a mixture of OAM modes by controlling the asymmetry in its intensity distribution. Using such tailored pump OAM spectra we have studied the bi-photon OAM eigen modes in the down conversion process. The direct correlation of the pump OAM spectra to the bi-photon OAM eigen modes in SPDC process confirms the direct control of spiral bandwidth of the entangled photons. We have quantified the broadening of the bi-photon OAM eigen modes by calculating the Schmidt number, and observed the enhancement in the number of the bi-photon OAM eigen modes by tailoring the asymmetry of the pump vortices.

8.2 Scope for future work

Generation of quantum entangled state have been predominantly based on Gaussian beam. Through this work, we have extended from the domain of generation of entangled state with Gaussian beam towards relativity unexplored domain, that is generation of entangled state with structured pump beam. We have generated bi-photon modes with Gaussian, perfect vortex, vortex and asymmetric vortex beam. However, there are lot of structured beam whose effect on bi-photon modes are not known yet. One of the best example of that kind is Airy beam. Acceleration and self healing are characteristic properties of Airy beams. Using such beams, we would like to explore the scope of generation of accelerating and self-healing bi-photon modes in future. We demonstrated the direct generation of bi-photon hybrid entangled state with the help of non-separable pump beam. However our source lacking the efficiency in terms of number photons. Two overcome such problem, combining the scheme in chapter 5 and in chapter 2, we would like to develop a high brightness hybrid entangled bi-photon state in future. In chapter 6, We have limited our study of bi-photon OAM eigen modes while only varying the asymmetry, but the study can be extended while varying the pump beam size and bi-photon OAM mode size. Combining the scheme in chapter 5 and chapter 6, and with the help of asymmetric vortex beam we would like extend the study of generation of simultaneous multiple hybrid entangled states.

Bibliography

[1] A. Einstein, B. Podolsky, and N. Rosen, *Can quantum-mechanical description of physical reality be considered complete?* Physical review **47**, 777 (1935).

[2] J. S. Bell, *On the einstein podolsky rosen paradox,* in "John S Bell On The Foundations Of Quantum Mechanics," (World Scientific, 2001), pp. 7–12.

[3] J. F. Clauser, M. A. Horne, A. Shimony, and R. A. Holt, *Proposed experiment to test local hidden-variable theories,* Physical review letters **23**, 880 (1969).

[4] A. Mair, A. Vaziri, G. Weihs, and A. Zeilinger, *Entanglement of the orbital angular momentum states of photons.* Nature **412**, 313–6 (2001).

[5] A. Vaziri, G. Weihs, and A. Zeilinger, *Experimental two-photon, three-dimensional entanglement for quantum communication,* Physical Review Letters **89**, 240401 (2002).

[6] J. Barreiro, *Jt barreiro, nk langford, na peters, and pg kwiat, phys. rev. lett. 95, 260501 (2005).* Phys. Rev. Lett. **95**, 260501 (2005).

[7] S. P. Walborn, *Hyperentanglement: Breaking the communication barrier,* Nature Physics **4**, 268 (2008).

[8] J. T. Barreiro, T.-C. Wei, and P. G. Kwiat, *Beating the channel capacity limit for linear photonic superdense coding,* Nature physics **4**, 282 (2008).

[9] J. T. Barreiro, T.-C. Wei, and P. G. Kwiat, *Remote preparation of single-photon hybrid entangled and vector-polarization states,* Physical review letters **105**, 030407 (2010).

[10] M. M. Wilde and D. B. Uskov, *Linear-optical hyperentanglement-assisted quantum error-correcting code,* Physical Review A **79**, 022305 (2009).

[11] W. Nogueira, M. Santibanez, S. Pádua, A. Delgado, C. Saavedra, L. Neves, and G. Lima, *Interference and complementarity for two-photon hybrid entangled states,* Physical Review A **82**, 042104 (2010).

[12] M. Jabir, N. A. Chaitanya, M. Mathew, and G. Samanta, *Direct transfer of classical non-separable states into hybrid entangled two photon states,* Scientific reports **7**, 7331 (2017).

[13] D. C. Burnham and D. L. Weinberg, *Observation of simultaneity in parametric production of optical photon pairs,* Physical Review Letters **25**, 84 (1970).

[14] C. Hong and L. Mandel, *Theory of parametric frequency down conversion of light,* Physical Review A **31**, 2409 (1985).

[15] F. M. Miatto, H. D. L. Pires, S. M. Barnett, and M. P. van Exter, *Spatial schmidt modes generated in parametric down-conversion,* The European Physical Journal D **66**, 263 (2012).

[16] R.-B. Jin, R. Shimizu, K. Wakui, M. Fujiwara, T. Yamashita, S. Miki, H. Terai, Z. Wang, and M. Sasaki, *Pulsed sagnac polarization-entangled photon source with a ppktp crystal at telecom wavelength,* Optics Express **22**, 11498–11507 (2014).

[17] V. Vicuna-Hernandez, H. Cruz-Ramirez, R. Ramirez-Alarc'on, and A. B. U Ren, *Classical to quantum transfer of optical vortices,* Optics Express **22**, 20027–20037 (2014).

[18] R. L. Sutherland, *Handbook of nonlinear optics* (CRC press, 2003).

[19] L. Allen, M. W. Beijersbergen, R. J. C. Spreeuw, and J. P. Woerdman, *Orbital angular momentum of light and the transformation of Laguerre-Gaussian laser modes,* Phys. Rev. A **45**, 8185–8189 (1992).

[20] T. F. Scott, B. A. Kowalski, A. C. Sullivan, C. N. Bowman, and R. R. McLeod, *Two-Color Single-Photon Photoinitiation and Photoinhibition for Subdiffraction Photolithography,* Science **324**, 913–917 (2009).

[21] N. Apurv Chaitanya, A. Aadhi, R. P. Singh, and G. K. Samanta, *Type-I frequency-doubling characteristics of high-power, ultrafast fiber laser in thick BIBO crystal.* Opt. Lett. **39**, 5419–22 (2014).

[22] S. Slussarenko, A. Murauski, T. Du, V. Chigrinov, L. Marrucci, and E. Santamato, *Tunable liquid crystal q-plates with arbitrary topological charge,* Optics express **19**, 4085–4090 (2011).

[23] R. Fickler, G. Campbell, B. Buchler, P. K. Lam, and A. Zeilinger, *Quantum entanglement of angular momentum states with quantum numbers up to 10,010,* Proceedings of the National Academy of Sciences **113**, 13642–13647 (2016).

[24] S. G. Reddy, C. Permangatt, S. Prabhakar, A. Anwar, J. Banerji, and R. P. Singh, *Divergence of optical vortex beams,* Appl. Opt. **54**, 6690 (2015).

[25] A. S. Ostrovsky, C. Rickenstorff-Parrao, and V. Arrizón, *Generation of the "perfect" optical vortex using a liquid-crystal spatial light modulator.* Opt. Lett. **38**, 534–6 (2013).

[26] S. U. Alam, A. S. Rao, A. Ghosh, P. Vaity, and G. Samanta, *Controlled generation, manipulation and frequency conversion of broadband orbital angular momentum spectrum of asymmetric optical vortex beams,* arXiv preprint arXiv:1801.02802 (2018).

[27] V. V. Kotlyar, A. A. Kovalev, and A. P. Porfirev, *Asymmetric gaussian optical vortex,* Optics letters **42**, 139–142 (2017).

[28] N. Gisin and R. Thew, *Quantum communication,* Nature Photonics **1**, 165 EP – (2007). Review Article.

[29] D. Bouwmeester, J.-W. Pan, K. Mattle, M. Eibl, H. Weinfurter, and A. Zeilinger, *Experimental quantum teleportation,* Nature **390**, 575 (1997).

[30] E. Knill, R. Laflamme, and G. J. Milburn, *A scheme for efficient quantum computation with linear optics,* nature **409**, 46 (2001).

[31] M. Jing, Z. Guang-Yu, and T. Li-Ying, *Theoretical study of quantum bit rate in free-space quantum cryptography,* Chinese Physics Letters **23**, 1379 (2006).

[32] D. Dequal, G. Vallone, D. Bacco, S. Gaiarin, V. Luceri, G. Bianco, and P. Villoresi, *Experimental single-photon exchange along a space link of 7000 km,* Physical Review A **93**, 010301 (2016).

[33] P. Michler, A. Kiraz, C. Becher, W. Schoenfeld, P. Petroff, L. Zhang, E. Hu, and A. Imamoglu, *A quantum dot single-photon turnstile device,* science **290**, 2282–2285 (2000).

[34] M. Medic, J. B. Altepeter, M. A. Hall, M. Patel, and P. Kumar, *Fiber-based telecommunication-band source of degenerate entangled photons,* Optics letters **35**, 802–804 (2010).

[35] J. Brendel, N. Gisin, W. Tittel, and H. Zbinden, *Pulsed energy-time entangled twin-photon source for quantum communication,* Physical Review Letters **82**, 2594 (1999).

[36] P. G. Kwiat, E. Waks, A. G. White, I. Appelbaum, and P. H. Eberhard, *Ultrabright source of polarization-entangled photons,* Physical Review A **60**, R773 (1999).

[37] M. Fiorentino, S. M. Spillane, R. G. Beausoleil, T. D. Roberts, P. Battle, and M. W. Munro, *Spontaneous parametric down-conversion in periodically poled ktp waveguides and bulk crystals,* Optics Express **15**, 7479–7488 (2007).

[38] M. Fiorentino and R. G. Beausoleil, *Compact sources of polarization-entangled photons,* Optics Express **16**, 20149–20156 (2008).

[39] Y.-C. Jeong, K.-H. Hong, and Y.-H. Kim, *Bright source of polarization-entangled photons using a ppktp pumped by a broadband multi-mode diode laser,* Optics Express **24**, 1165–1174 (2016).

[40] S. M. Lee, H. Kim, M. Cha, and H. S. Moon, *Polarization-entangled photon-pair source obtained via type-ii non-collinear spdc process with ppktp crystal,* Optics Express **24**, 2941–2953 (2016).

[41] M. Fiorentino, C. E. Kuklewicz, and F. N. Wong, *Source of polarization entanglement in a single periodically poled ktiopo 4 crystal with overlapping emission cones,* Optics Express **13**, 127–135 (2005).

[42] F. Steinlechner, M. Gilaberte, M. Jofre, T. Scheidl, J. P. Torres, V. Pruneri, and R. Ursin, *Efficient heralding of polarization-entangled photons from type-0 and type-ii spontaneous parametric downconversion in periodically poled ktiopo 4,* JOSA B **31**, 2068–2076 (2014).

[43] F. Steinlechner, S. Ramelow, M. Jofre, M. Gilaberte, T. Jennewein, J. P. Torres, M. W. Mitchell, and V. Pruneri, *Phase-stable source of polarization-entangled photons in a linear double-pass configuration,* Optics express **21**, 11943–11951 (2013).

[44] F. Steinlechner, P. Trojek, M. Jofre, H. Weier, D. Perez, T. Jennewein, R. Ursin, J. Rarity, M. W. Mitchell, J. P. Torres *et al.*, *A high-brightness source of polarization-entangled photons optimized for applications in free space,* Optics express **20**, 9640–9649 (2012).

[45] Y. Li, Z.-Y. Zhou, D.-S. Ding, and B.-S. Shi, *Cw-pumped telecom band polarization entangled photon pair generation in a sagnac interferometer,* Optics Express **23**, 28792–28800 (2015).

[46] K. Thyagarajan, J. Lugani, S. Ghosh, K. Sinha, A. Martin, D. B. Ostrowsky, O. Alibart, and S. Tanzilli, *Generation of polarization-entangled photons using type-ii doubly periodically poled lithium niobate waveguides,* Physical Review A **80**, 052321 (2009).

[47] H. J. Lee, H. Kim, M. Cha, and H. S. Moon, *Generation of bright visible photon pairs using a periodically poled stoichiometric lithium tantalate crystal,* Optics Express **23**, 14203–14210 (2015).

[48] A. Fedrizzi, T. Herbst, A. Poppe, T. Jennewein, and A. Zeilinger, *A wavelength-tunable fiber-coupled source of narrowband entangled photons,* Optics Express **15**, 15377–15386 (2007).

[49] B.-S. Shi and A. Tomita, *Generation of a pulsed polarization entangled photon pair using a sagnac interferometer,* Physical Review A **69**, 013803 (2004).

[50] T. Kim, M. Fiorentino, and F. N. Wong, *Phase-stable source of polarization-entangled photons using a polarization sagnac interferometer,* Physical Review A **73**, 012316 (2006).

[51] O. Kuzucu and F. N. Wong, *Pulsed sagnac source of narrow-band polarization-entangled photons,* Physical Review A **77**, 032314 (2008).

[52] A. Predojević, S. Grabher, and G. Weihs, *Pulsed sagnac source of polarization entangled photon pairs,* Optics Express **20**, 25022–25029 (2012).

[53] M. Jabir, N. A. Chaitanya, A. Aadhi, and G. Samanta, *Generation of perfect vortex of variable size and its effect in angular spectrum of the down-converted photons,* Scientific reports **6**, 21877 (2016).

[54] G. K. Samanta and M. Kumar, S Chaitanya, Ebrahim-Zadeh, *Stable, 9.6 W, continuous-wave, single-frequency, fiber-based green source at 532 nm,* Opt. Lett. **34**, 1561–1563 (2009).

[55] K. Kato and E. Takaoka, *Sellmeier and thermo-optic dispersion formulas for ktp,* Applied optics **41**, 5040–5044 (2002).

[56] R. Rangarajan, M. Goggin, and P. Kwiat, *Optimizing type-i polarization-entangled photons,* Optics express **17**, 18920–18933 (2009).

[57] D. F. V. James, P. G. Kwiat, W. J. Munro, and A. G. White, *Measurement of qubits,* Phys. Rev. A **64**, 052312 (2001).

[58] P. Kok, W. J. Munro, K. Nemoto, T. C. Ralph, J. P. Dowling, and G. J. Milburn, *Linear optical quantum computing with photonic qubits,* Reviews of Modern Physics **79**, 135 (2007).

[59] M. P. Edgar, D. S. Tasca, F. Izdebski, R. E. Warburton, J. Leach, M. Agnew, G. S. Buller, R. W. Boyd, and M. J. Padgett, *Imaging high-dimensional spatial entanglement with a camera,* Nature communications **3**, 984 (2012).

[60] R. Ramirez Alarcon, H. Cruz Ramirez, and A. B. URen, *Effects of crystal length on the angular spectrum of spontaneous parametric downconversion photon pairs,* Laser Physics **23**, 055204 (2013).

[61] S. Prabhakar, S. Gangi Reddy, A. Aadhi, A. Kumar, P. Chithrabhanu, G. Samanta, and R. Singh, *Spatial distribution of spontaneous parametric down-converted photons for higher order optical vortices,* Opt. Commun. **326**, 64–69 (2014).

[62] S. G. Reddy, S. Prabhakar, A. Kumar, J. Banerji, and R. P. Singh, *Higher order optical vortices and formation of speckles.* Opt. Lett. **39**, 4364–7 (2014).

[63] M. Chen, M. Mazilu, Y. Arita, E. M. Wright, and K. Dholakia, *Dynamics of microparticles trapped in a perfect vortex beam,* Optics letters **38**, 4919–4922 (2013).

[64] P. Vaity and L. Rusch, *Perfect vortex beam: Fourier transformation of a Bessel beam,* Opt. Lett. **40**, 597 (2015).

[65] P.-A. Belanger and M. Rioux, *Ring pattern of a lens–axicon doublet illuminated by a gaussian beam,* Applied optics **17**, 1080–1088 (1978).

[66] J. Arlt and K. Dholakia, *Generation of high-order bessel beams by use of an axicon,* Opt. Commun. **177**, 297–301 (2000).

[67] V. Jarutis, R. Paskauskas, and A. Stabinis, *Focusing of laguerre–gaussian beams by axicon,* Optics communications **184**, 105–112 (2000).

[68] D. G. Grier, *A revolution in optical manipulation.* Nature **424**, 810–6 (2003).

[69] C. I. Osorio, G. Molina-Terriza, B. G. Font, and J. P. Torres, *Azimuthal distinguishability of entangled photons generated in spontaneous parametric down-conversion,* Optics Express **15**, 14636–14643 (2007).

[70] J. Goodman, *Introduction to fourier optics,* (2008).

[71] N. Apurv Chaitanya, A. Aadhi, M. V. Jabir, and G. K. Samanta, *Frequency-doubling characteristics of high-power, ultrafast vortex beams,* Opt. Lett. **40**, 2614 (2015).

[72] O. Brzobohaty, T. Cizmar, and P. Zemanek, *High quality quasi-bessel beam generated by round-tip axicon,* Optics express **16**, 12688–12700 (2008).

[73] G. Molina-Terriza, J. P. Torres, and L. Torner, *Twisted photons,* Nature physics **3**, 305 (2007).

[74] H. Cruz-Ramirez, R. Ramirez-Alarcon, F. J. Morelos, P. A. Quinto-Su, J. C. Gutierrez-Vega, and A. B. U Ren, *Observation of non-diffracting behavior at the single-photon level,* Optics express **20**, 29761–29768 (2012).

[75] R. Fickler, M. Krenn, R. Lapkiewicz, S. Ramelow, and A. Zeilinger, *Real-time imaging of quantum entanglement,* Scientific reports **3**, 1914 (2013).

[76] P. G. Kwiat, K. Mattle, H. Weinfurter, A. Zeilinger, A. V. Sergienko, and Y. Shih, *New high-intensity source of polarization-entangled photon pairs,* Physical Review Letters **75**, 4337 (1995).

[77] H. Takesue, K. Inoue, O. Tadanaga, Y. Nishida, and M. Asobe, *Generation of pulsed polarization-entangled photon pairs in a 1.55-μm band with a periodically poled lithium niobate waveguide and an orthogonal polarization delay circuit,* Optics letters **30**, 293–295 (2005).

[78] R. L. D. DiVincenzo, E. Knill and W. Zurek, *Special issue on quantum coherence and decoherence,* Proc. R. Soc. London **Ser. A 1969** (1998).

[79] A. K. Ekert, *Quantum cryptography based on bell's theorem,* Phys. Rev. Lett. **67**, 661–663 (1991).

[80] C. H. Bennett and S. J. Wiesner, *Communication via one-and two-particle operators on einstein-podolsky-rosen states,* Physical review letters **69**, 2881 (1992).

[81] R. Ghosh and L. Mandel, *Observation of nonclassical effects in the interference of two photons,* Physical Review Letters **59**, 1903 (1987).

[82] S. P. Walborn, C. Monken, S. Pádua, and P. S. Ribeiro, *Spatial correlations in parametric down-conversion,* Physics Reports **495**, 87–139 (2010).

[83] Z. Ou, *Zy ou and l. mandel, phys. rev. lett. 61, 50 (1988).* Phys. Rev. Lett. **61**, 50 (1988).

[84] J. Franson, *Jd franson, phys. rev. lett. 62, 2205 (1989).* Phys. Rev. Lett. **62**, 2205 (1989).

[85] R. Fickler, R. Lapkiewicz, S. Ramelow, and A. Zeilinger, *Quantum entanglement of complex photon polarization patterns in vector beams,* Physical Review A **89**, 060301 (2014).

[86] L. Neves, G. Lima, A. Delgado, and C. Saavedra, *Hybrid photonic entanglement: Realization, characterization, and applications,* Physical Review A **80**, 042322 (2009).

[87] R. Fickler, R. Lapkiewicz, W. N. Plick, M. Krenn, C. Schaeff, S. Ramelow, and A. Zeilinger, *Quantum entanglement of high angular momenta,* Science **338**, 640–643 (2012).

[88] A. K. Jha, G. S. Agarwal, and R. W. Boyd, *Supersensitive measurement of angular displacements using entangled photons,* Physical Review A **83**, 053829 (2011).

[89] E. Nagali and F. Sciarrino, *Generation of hybrid polarization-orbital angular momentum entangled states,* Optics express **18**, 18243–18248 (2010).

[90] C. H. Monken, P. S. Ribeiro, and S. Pádua, *Transfer of angular spectrum and image formation in spontaneous parametric down-conversion,* Physical Review A **57**, 3123 (1998).

[91] Q. Zhan, *Cylindrical vector beams: from mathematical concepts to applications,* Advances in Optics and Photonics **1**, 1–57 (2009).

[92] C. Perumangatt, G. R. Salla, A. Anwar, A. Aadhi, S. Prabhakar, and R. Singh, *Scattering of non-separable states of light,* Optics Communications **355**, 301 – 305 (2015).

[93] H. D. L. Pires, H. Florijn, and M. Van Exter, *Measurement of the spiral spectrum of entangled two-photon states,* Physical review letters **104**, 020505 (2010).

[94] C. Borges, M. Hor-Meyll, J. Huguenin, and A. Khoury, *Bell-like inequality for the spin-orbit separability of a laser beam,* Physical Review A **82**, 033833 (2010).

[95] N. Apurv Chaitanya, M. V. Jabir, and G. K. Samanta, *Efficient nonlinear generation of high power, higher order, ultrafast "perfect" vortices in green,* Opt. Lett. **41**, 1348–1351 (2016).

[96] J. Torres, A. Alexandrescu, and L. Torner, *Quantum spiral bandwidth of entangled two-photon states,* Physical Review A **68**, 050301 (2003).

[97] Y. Jerónimo-Moreno and R. Jáuregui, *On-demand generation of propagation-invariant photons with orbital angular momentum,* Physical Review A **90**, 013833 (2014).

[98] C. I. Osorio, G. Molina-Terriza, and J. P. Torres, *Correlations in orbital angular momentum of spatially entangled paired photons generated in parametric down-conversion,* Physical Review A **77**, 015810 (2008).

[99] Z.-Y. Zhou, S.-L. Liu, Y. Li, D.-S. Ding, W. Zhang, S. Shi, M.-X. Dong, B.-S. Shi, and G.-C. Guo, *Orbital angular momentum-entanglement frequency transducer,* Physical review letters **117**, 103601 (2016).

[100] G. Masada, K. Miyata, A. Politi, T. Hashimoto, J. L. O'brien, and A. Furusawa, *Continuous-variable entanglement on a chip,* Nature Photonics **9**, 316 (2015).

[101] A. C. Dada, J. Leach, G. S. Buller, M. J. Padgett, and E. Andersson, *Experimental high-dimensional two-photon entanglement and violations of generalized bell inequalities,* Nature Physics **7**, 677 (2011).

[102] P. B. Dixon, G. A. Howland, J. Schneeloch, and J. C. Howell, *Quantum mutual information capacity for high-dimensional entangled states,* Physical review letters **108**, 143603 (2012).

[103] J. Romero, D. Giovannini, S. Franke-Arnold, S. Barnett, and M. Padgett, *Increasing the dimension in high-dimensional two-photon orbital angular momentum entanglement,* Physical Review A **86**, 012334 (2012).

[104] E. Kovlakov, I. Bobrov, S. Straupe, and S. Kulik, *Spatial bell-state generation without transverse mode subspace postselection,* Physical review letters **118**, 030503 (2017).

[105] C. Law and J. Eberly, *Analysis and interpretation of high transverse entanglement in optical parametric down conversion,* Physical review letters **92**, 127903 (2004).

[106] M. G. McLaren, F. S. Roux, and A. Forbes, *Realising high-dimensional quantum entanglement with orbital angular momentum,* South African Journal of Science **111**, 01–09 (2015).

[107] J. Gotte, S. Franke-Arnold, R. Zambrini, and S. M. Barnett, *Quantum formulation of fractional orbital angular momentum,* Journal of Modern Optics **54**, 1723–1738 (2007).

[108] A. M. Yao, *Angular momentum decomposition of entangled photons with an arbitrary pump,* New Journal of Physics **13**, 053048 (2011).